Problems of Planetology, Cosmochemistry and Meteoritica

Alexeev V.A., Pavlova T.A., Kalinina G.K. Some features of the radiation history of ureilites

Vernadsky Institute of Geochemistry and Analytical Chemistry RAS, Moscow (AVAL37@mail.ru)

Abstract. The analysis of the distributions of the cosmic-ray exposure ages and masses of ureilites in comparison with those for ordinary chondrites, as well as the analysis of the track study results of the Kenna ureilite are presented. The characteristic features found in the distributions are most likely associated with the presence of a larger proportion of ureilites with the small cosmic-ray exposure ages among the ureilites with small sizes. This fact may be due to the faster delivery of small-sized meteoroids on the orbits crossing the Earth's orbit, which in turn is associated with the more efficient transfer of the small bodies from the region of the asteroid belt in the resonances regions mainly in result of the action of "daily" component of the Yarkovsky effect.

Keywords: ureilites, cosmic-ray exposure ages, particle tracks

Introduction. Among the meteorites, the total number of which exceeded 70,000, the ureilites account are less than 0.8% - only 553 meteorites (https://www.lpi.usra.edu/meteor/metbull.php). The most of these meteorites (~55%) were found in the deserts of northwestern Africa. Ureilites differ from the most other meteorites in their unique mineralogical composition, high carbon content, and the presence of diamond of extraterrestrial origin. These meteorites are the second most common among achondrites (after eucrites). Based on the previous studies, the destruction and subsequent reaccumulation of the parent body of ureilites in the early Solar system, ~5 million years after the formation of CAI - calcium-aluminum inclusions is assumed (Goodrich et al., 2004). The further history of the parent body of ureilites can be partially established from the data on their cosmic-ray exposure ages. Leya and Stephenson (2019) presented the results of the new determinations of cosmic-ray exposure ages, as well as the compilation of the ages obtained by other researchers (Leya, Masarik, 2009) and adjusted with previously calculated of the formation rate of the cosmogenic ^{21}Ne according to the preatmospheric radius of the meteorite and the shielding degree of the studied sample. The submitted work presents the analysis results of the distribution of the cosmic-ray exposure ages and masses of ureilites in comparison with those for ordinary chondrites, as well as the analysis results of Wilkening and Marti (1976) of the track studies of the Kanne ureilite.

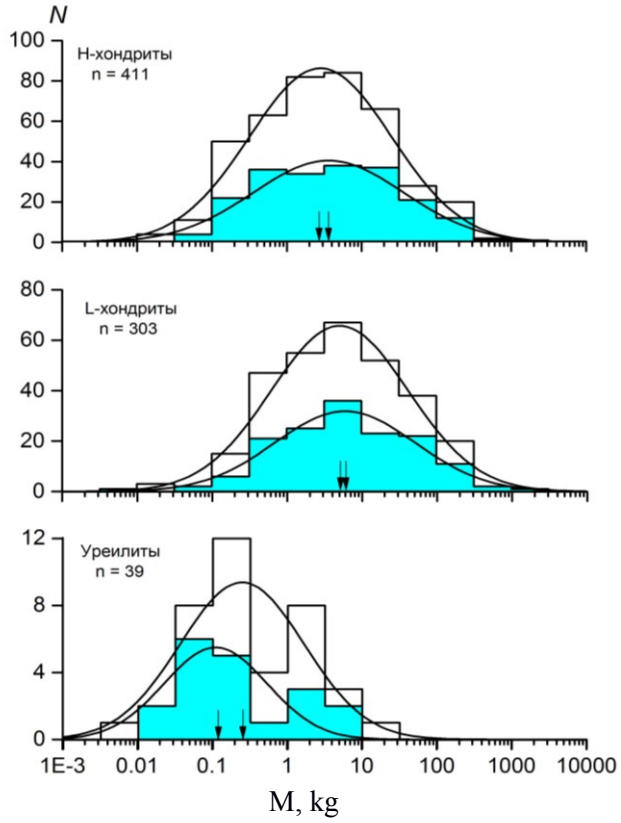

Fig. 1. Distributions of the found masses of H- and L-chondrites and ureilites. The arrows indicate the positions of the maxima of the Gaussian curves. The shaded part refers to meteorites with cosmic-ray exposure age of $T_{21}<T_{21,med}$.

The mass distribution of ordinary chondrites and ureilites. One of the specialties of the ureilites is the noticeable difference in the distribution of the found masses from distribution of the masses of the most common meteorites - ordinary chondrites (chemical groups H, L and LL). In **Fig. 1** there is shown the mass distributions of H- and L-chondrites and ureilites with the known cosmic-ray exposure ages (T_{21}). Information on the ages of H- and L-chondrites is taken from the results of previous studies (Alexeev, 2005) and refs there; the cosmic-ray exposure ages of 39 ureilites are taken from Leya

Table 1. The position of the maxima of the Gaussian curves (Fig. 1) in the mass distributions (M, kg) of H- and L-chondrites and ureilites.

Parameter of distribution	H-chondrites	L-chondrites	Ureilites
M_{av} (all meteorites)	2.82 ± 0.03	5.13 ± 0.06	0.25 ± 0.08
M_{av} ($T_{21}\leq T_{21,med}$)	3.62 ± 0.05	6.03 ± 0.08	0.11 ± 0.04
Δ*), kg	0.90 ± 0.10	0.90 ± 0.09	-0.14 ± 0.09

*) $\Delta = M_{av}$ ($T_{21}\leq T_{21,med}$) - M_{av} (все)

Table 2. The number of meteorites (N) in quadrants I÷IV in the distributions of masses (M, kg) depending on the cosmic-ray exposure ages (T_{21}, Ma) of H- and L-chondrites and ureilites (Fig. 2). Asymmetry in distributions.

Quadrant	H-chondrites	L-chondrites	Ureilites
I ($M>M_{med}$, $T_{21}>T_{21,med}$)	95	69	12
II ($M>M_{med}$, $T_{21}\leq T_{21,med}$)	110	82	7
III ($M\leq M_{med}$, $T_{21}\leq T_{21,med}$)	95	69	13
IV ($M\leq M_{med}$, $T_{21}>T_{21,med}$)	111	83	7
Asymmetry coefficient, α*)	-0.08 ± 0.02	-0.09 ± 0.02	0.28 ± 0.08

*) $\alpha = [(N_I + N_{III}) - (N_{II} + N_{IV})]/(N_I + N_{II} + N_{III} + N_{IV})$

and Stephenson (2019).

The mass distributions of both H- and L-chondrites can be approximated by a Gaussian curve, the parameters of which are given in **Table 1**. It is characteristic that for all H-chondrites with the known cosmic-ray exposure ages, the position of the curve maximum (2.82 kg) is lower than the maximum value (3.62 kg) by the value 8 = 0.90 ± 0.10 kg for chondrites, whose age is less than the median value of $T_{21,med}$.

The maximum of the L-chondrites mass distribution is at the higher value (5.13 kg) than for H-chondrites. However, in this case, as for H-chondrites, the position of maximum for meteorites with $T_{21}\leq T_{21,med}$ falls on the region of the higher values of mass (8 = 0.90 kg).

For ureilites, a different picture is observed. The positions of the maxima fall at the significantly lower mass values than for H- or L-chondrites. Moreover, in contrast to H- and L-chondrites, the maximum of the Gaussian curve for ureilites with $T_{21}\leq T_{21,med}$ is on the lower mass values (0.11 kg) than for all meteorites: 8 = -0.14 kg.

The found features in the mass distributions may be due to the difference in both the sizes and structure of the parent bodies of these meteorite groups.

Asymmetry in the distribution of meteorite ages. The age distributions of the ordinary chondrites have been studied in many works (Alexeev, 2005 and links there). Often, an analysis of the distributions is carried out to establish a collision history of meteorites (Graf, Marti, 1995). A characteristic feature of ureilites is manifested when comparing the distribution of their cosmic-ray exposure ages with those for the meteorites of other types (**Fig. 2**).

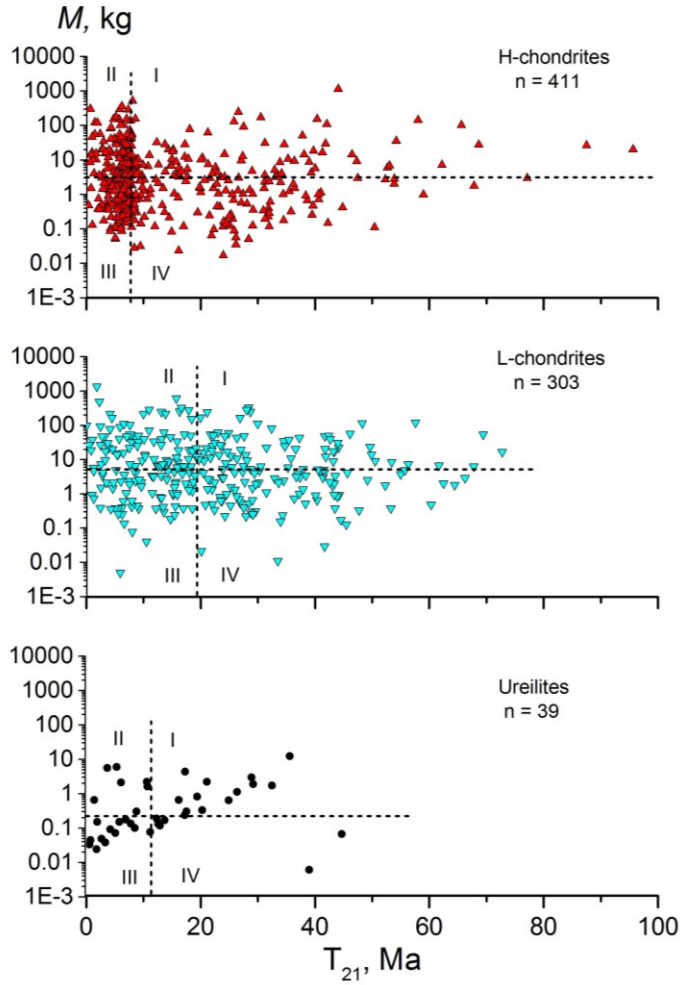

Fig. 2. Distribution of radiation ages of meteorites in comparison with the found mass. The dashed lines correspond to the median values of the corresponding quantities. I÷IV are quadrants.

The analysis of the age distributions of more than 700 H- and L-chondrites showed a small asymmetry. The coefficient of asymmetry α = [(NI + NIII) - (NII + NIV)]/(NI + NII + NIII +NIV) characterizes the relative difference in the numbers of meteorites in quadrants I + III and II + IV. Quadrants are formed with using the median age values ($T_{21,med}$) and masses (M_{med}) of meteorites in the distribution. The stronger the value α differs from zero, the greater the "skewness" and, accordingly, the higher asymmetry in the distribution. From the results of the analysis of the data shown in Fig. 2, it is seen (**Table 2**) that the asymmetry coefficients for both H- and L-chondrites have close negative values, slightly differing from zero: $\alpha \sim -0.1$.

Details of the calculations and the results of the age determination are given in (Alekseev, 2005) and in the refs there. The porosity information is taken from (Macke, 2010). For ureilites the asymmetry coefficient is positive and significantly higher than zero (0.28 ± 0.08). This feature is due to the clearly expressed tendency of increase in the cosmic-ray exposure age with increase in mass.

Tracks in ureilitites. Additional information about ureilites can be obtained from the results of track studies. However, at present, the number of such studies is rather small. As an example, we consider the data obtained by Wilkening and Marti (1976) for the Kenna ureilite with using the later data on the cosmic-ray exposure age of this meteorite and on the dependence of the track production rate in meteorites of different sizes.

When studying the track distribution in olivine crystals, there are usually attracted the calculated track production rates in *pyroxene of chondrites* (ρ/T, where ρ is the track density, cm^{-2} and T is the cosmic-ray exposure age of the meteorite, million years) in dependence on the occurrence depth of the sample (d, cm) in meteorites of various preatmospheric sizes (Bhattachrja et al., 1973) with subsequent correction for olivine. To unify the procedures for the distribution analysis, there were carried out the calculations, based on the results of Bhattachrja et al. (1973) on the depth distribution of the track production rate of iron group nuclei, VH-nuclei ($24 \leq Z \leq 28$) in *olivine of chondrites* of different preatmospheric sizes (Alexeev et al., 2019). In these calculations, it was taken into account that the track production rate in pyroxene is higher than in olivine. According to various researchers, the excess coefficient was found to be from 1.8 to 2.9. In this work, to calculate the equivalent rate of track production in pyroxene according to the data obtained for olivine, we used the average value of these values, which amounted to 2.3 ± 0.5.

The closeness of the values of the bulk density of ureilites and ordinary chondrites of the different chemical groups, according to a representative summary of the data (Macke, 2010), made it possible to use for ureilites the track production rates in depend on the depth, obtained for chondrites.

Table 3 shows the track data obtained by Wilkening and Marti (1976) for the Kenna ureilite, recalculated taking into account the adjusted by Leya and Stephenson (2019) cosmic-ray exposure age for this meteorite T_{21} = 35.6 Ma (instead of the value using by Wilkening and Marti (1976) 23.6 Ma) and with involving the depth dependence of the track production rate in meteorites of the different sizes according to (Bhattachrja et al., 1973). Based on these data, an estimate was made of the depth of the studied samples (d ~2 and ~10 cm) in a preatmospheric hypothetically spherical meteoroid of radius R ~15 cm.

Table 3. Modified track data for the Kenna ureilite in according to (Wilkening, Marti, 1976).

Sample	Number of crystals	Number of tracks	Density of tracks, ρ, 10^6 cm^{-2}	Track production rate, D, 10^5 cm^{-2} Ma^{-1}	Depth, d, cm
1	48	5413	4.3	1.2	2 ± 1
2	20	2180	1.7	0.5	10 ± 1

Conclusions. The characteristic features in the distribution of the found masses and the cosmic-ray exposure ages of ureilites are established in comparison with those for H- and L-chondrites, the most representative chemical groups of ordinary chondrites. The distribution maximum of the found masses of ureilites is placed on the significantly lower value (0.25 kg) in comparing with H- and L-chondrites: 2.8 and 5.1 kg, respectively. For ureilites, the asymmetry was found in the cosmic-ray exposure age distribution. This asymmetry is practically absent in the age distributions of H- and L-chondrites. The corrected track data of the Kenna ureilite indicate an insignificant depth location of the studied samples in the body of the preatmospheric meteoroid of the small size.

The noted effects are most likely associated with the presence of the larger proportion of ureilites with small cosmic-ray exposure ages among the ureilites of the small sizes. This fact may be due to the faster delivery of small-sized meteoroids on the orbits crossing the Earth's orbit, which in turn is associated with the more efficient transition of the small bodies from the region of the asteroid belt in the resonances regions mainly in result of the action of "daily" component of the Yarkovsky effect.

The work was partially supported by the Program No. 12 of the Presidium of the RAS.

References

Alexeev V.A. The history of ordinary chondrites from the data on stable isotopes of noble gases (a review) // *Sol. Syst. Res.* 2005. V. 39. No. 2. P. 124-149.

Alexeev V.A., Bagulya A.V., Volkov A.E., Gippius A.A., Goncharova L.A., Gorbunov S.A., Grachev V.M., Dashkina A.B., Kalinina G.V., Konovalova N.S., Okateva N.M., Pavlova T.A., Polukhina N.G., Starkov N.I., ThanNaing Soe, Chernyvsky M.M., Shchedrina T.V. Study of the Pallasite Radiation History by Track Analysis // *Bulletin of the Lebedev Physics Institute* 2019. V. 46. No. 8. P. 251–255. DOI: 10.3103/S1068335619080037.

Bhattacharya S.K., Goswami J.N., Lal D. Semiempirical rates of formation of cosmic ray tracks in spherical objects exposed in space: pre- and post-atmospheric depth profiles // *J. Geophys. Res.*1973. V. 78. No. 34. P. 8356-8363.

Goodrich C. A., Scott E. R. D., Fioretti A. M. Ureilitic breccias: Clues to the petrologic structure and impact disruption of the ureilite asteroid // *Chemie der Erde* 2004. V. 64. P. 283–327.

Graf Th., Marti K. Collisional history of H chondrites // *J. Geophys. Res*. 1995. V. 100. E10. P. 21247-21263.

Leya I., Masarik J. Cosmogenic nuclides in stony meteorites revisited // *Meteoritics & Planetary Science* 2009. V. 44. P. 1061–1086.

Leya I., Stephenson P.C. Cosmic ray exposure ages for ureilites—New data and a literature study // *Meteoritics & Planetary Science* 2019. P. 1-21 (https://doi.org/10.1111/maps.13288).

Macke R.J. Survey of Meteorite Physical Properties: Density, Porosity and Magnetic Susceptibility // Ph.D. Thesis, University of Central Florida. 2010. 332 p.

Wilkening L.L., Marti K. Rare gases and fossil particle tracks in the Kenna ureilite // *Geochim. Cosmochim. Acta* 1976. V. 40. P. 1465-1473.

Badekha[1] K. A., Grokhovsky[2] V.I. Phase transformation in the mono cristalls of meteoritic and laboratory origin. UDC 669.017.3

[1]Vernadsky Institute of Geochemistry, Moscow (ksenia_uimina@mail.ru),
[2]Ural Federal University, Ekaterinburg

Abstract. The work is devoted to the research of phase transformation in the iron meteorites Fe-18%Ni and terrestrial monocrystal steel containing Schlieren Bands or selective sheen in the polished and etched sections. The research was carried out using ZEISS ΣIGMA VP SEM with EBSD unit and the corresponding soft.

Key words: monocrystals, IVB group meteorites, phase-transformations, EBSD-analysis, Schlieren Bands.

The steel is one of the most spread constructing material. The knowledge we get while studding th phase transformation process and its characteristics in the alloys on the base of Fe is the base of the modern material science. Diffusionless martensite transformations are characterized with significant orientation relations between the cristal sell of the original and the final phases. The transphormation takes place at low temperatures. Also we observe bainite transformation when at the certain stage the growth of the new phase becomes diffusion-controlled, but the crystals of the new phase keep the orientation observed for the shift-transformations..

There are some examples of the martensite transformation in the monocrystals of the steels (Khlebnikova et al., 1997). It was mentioned, that the zones of the selective sheen appear on the polished and etched surfaces (Fig. 1a). The properties of the zones are similar to the Schlieren Bands (Buchwald, 1981) observed in the high Ni-iron meteorites (Ataxites and close to them ungrouped meteorites-Chinga).

Natural monocrystals that are accessible for analysis are Iron meteorites. This study is devoted to the crystallographic analysis of the phases, observed in the pare of the selective sheen zones in several meteorites (Hoba, Chinga, Cape of Good Hope, Iquique) and in the sample of the monocrystalline Fe-40%Cr steel. The study was carried out using ZEISS ΣIGMA VP SEM with EBSD unit on the base of Ural Federal University.

Samples and methods. The monocrystal of the Fe-40%Cr steel was grown using Bridgmen method on the base of Ural institute of the metal physics (Khlebnikova et al., 1997). In had a shape of column. The sample was cut from the column (Fig. 1a) and had the width of several mm. The meteorites were observed earlier (Badekha, 2012) and here we refer for the several of them: Hoba (16,56 вес.% Ni, 0,07 вес.% P), Cape of Good Hope* (16,3 вес.% Ni, 0,12 вес.% P), Iquique (16 вес.% Ni, 0,09 вес.% P) IVB Irons and Chinga (16,58 вес.% Ni, 0,05 вес.% P) ungrouped.

The samples were cut and polished using standard procedure of the section preparation – almond pastas and finishing SiO_2 colloide with 0,04 um particles. Hoba and Fe-40%Cr steel (as other monocrystalline samples (Khlebnikova et al., 1997) have 4 types of the sheen, but other meteorites demonstrate only two – dark and light (Fig. 1 a-f). The research of the metal was carried out using as SEM, so the optical microscope. Structural differences were observed. The steel, Hoba and Cape of Good hope have larger structuralunits, the shlieren bands can be found without etching just because of the visible orientation of metal phases. In Hoba it is less observed, but the structure is more rude, than in Iquqique and of course than in Chinga (Fig.1).

Chinga demonstrate a bright band-contrast during EBSD- Bcc-orientation mapping, but without the orientation analysis its submicrostructure remains mud and dense and can be distinguished only with the highest magnification (Fig.1m) – because of the chemical composition and the peculiar thermal history of the meteorite.

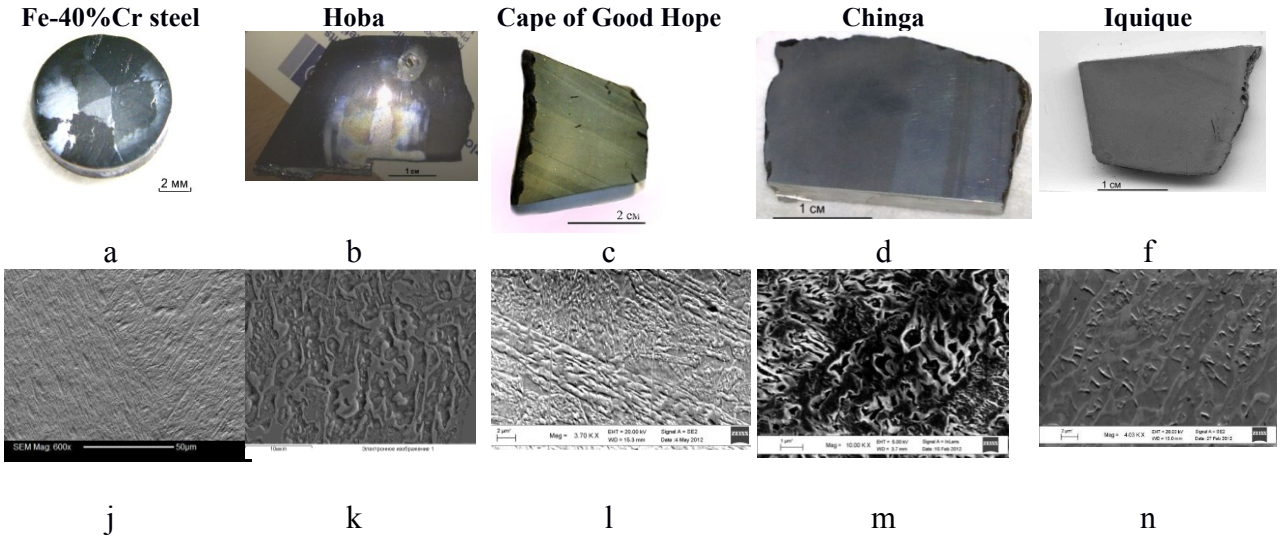

Fig. 1 . The samples and its structure: a – monocrystalline Fe-40%Cr steel, b- Hoba ataxite, c – Cape of Good Hope ataxite, d – Chinga, f – Iquique ataxite, j-n – corresponding SEM-pictures of the metal structure.

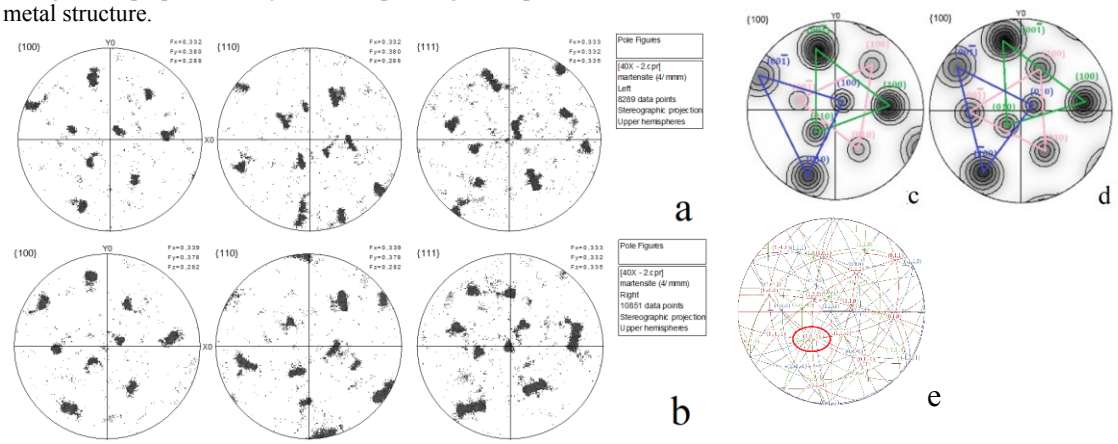

Fig. 2. Pole Figures for the martensite from the left (a) and right (b) of the Zones border. Pole Figures with intensity treatment divided to 3 orientations in one of the projections from the right (c) and left (d) areas of the Zones border; overlapping of two Bcc-orientations orientations in Hoba with Miller index identification and revealing of the rotation axis (e)

EBSD-analysis aloud dividing metal structure to Bcc- and Fcc- phases. In the steel the analysis divided martensite and the Bcc-phase, no Fcc remained. But all meteorites demonstrated the phase-maps with Bcc-subgrains with Fcc-rims (on side) – known plessite structure (Buchwald, 1975). The treatment of the Pole Figures for the Bcc- and Fcc-phases was carried out as using INCA Crystal 300 corresponding soft, so by hands with Carine Crystallography 3.1 and using the Wulff net. Also the overlapping of the Pole figures was carried out in Corel Draw and the orientation angles between the certain planes and directions was revealed (orientation relations of *Kurdyumov-Sachs* and Nishiyama-Wasserman).

All poles on the Experimental Pole Figures were revealed and named using the superpositions of the orientations fond with Carine Crystallography 3.1. Usually 3 orientations were enough to describe the Experimental Figure. Because of the structural elements small size and the surface preparation imperfections the Experimental Pole Figures were sometimes dense (especially for Chinga), but nether the less the orientation contrast was visible on the Bcc-phase maps. A well-described Pole Figures were received from Hoba and Fe-40%Cr steel samples. In other cases it was necessary to reveal the center of the Pole using intensity treatment. This of course lessens the number of orientations revealed and the accuracy.

The mistake was calculated for each Pole of each orientation in Microsoft Excel, corresponding the shift from the theoretical model advised by Carine Crystallography 3.1. The calculation of the

Orientation Relations was carried out using the special method of orientation link matrixes for the cubic cell (Ural Institute of the metal physics, Gundirev et al., 2003).

Results and discussion. EBSD-analysis revealed 3 phases in the Fe-40%Cr steel monocrystal - martensite(42,3%), cementite Fe_3C (10,7%) and Bcc-Fe (14,1%). Cementite Fe_3C precipitations point out to the unfinished hardening process with occurrence of low bainite, accompanied by precipitation of disperse cementite phase. A set of Pole figures in the right and left region of the Sheer zones border was occurred for each phase. The value of the texture maximum angle disperse, which characterizes the disorientation of the crystal cells of the α_2-phase in the each Schlieren Band or Sheer Zone is up to 9^o (Fig.2)

The superposition of 3 crystallographic orientations was revealed for the martensite in each Zone (Fig.2). One of them (MR1, ML1) is the main (according to the intensity of the corresponding Poles). An common axis of rotation can be revealed for each orientation of the martensite (it is visible while overlapping the Pole Figures – the Pole, corresponding to the axis of rotation coincides for each orientation – a common Pole [111] и [010]). Close-packed [111] direction for two of six orientations revealed and [010] for two of martensite crystals types might correspond to <110> close-packed direction of the initial austenite Fcc-phase.

It was established, that all martensite crystals orientations revealed correspond to one of the known orientation relations – *Kurdyumov-Sachs* (K-S) orientation relation– with accuracy of 5-7^o (Table 1). Other monocrystal steels studied (Khlebnikova et al., 1997) also demonstrated a slight distortion from K-S relation - 2,3^o and N-W - 2,9^o (X-ray diffraction was used). So it seems to be closer to K-S orientation relation. For iron meteorites it was also considered (Goldstein., Michael, 2006), that Bcc-Fcc orientation relation is between K-S and N-W (according to the EBSD-data).

Observed characteristics of meteoritic metal crystal orientations correspond to those observed by Laue method (Buchwald, 1981). The common features for all observed metal monocrystals are the set of 3 Bcc-phase orientations, which have an axis of rotation and orientation link with the primary austenitic Fcc-phase. In meteoriteswe always observed residual Fcc-phase surrounding subgrains of Bcc-phase and on side of rare kamasite grains having single orientation (Badekha, 2012). The Pole Figures received for Hoba meteorite (Fig.3) are of highest quality among meteorites investigated and are close to theoretical for K-S+N-W (Goldstain, Michael, 2006) when overlapped.

Table 1 – Orientation relations for the Fe-40%Cr steel main martensite orientations from the left (L) and Right (R) zones of selective sheen.

Orientation pare	Close-packed planes	Directions	Planes lie in the directions	Rotation around the cubic lattice axis
R_1, L_1	$[111]_L \parallel [111]_R$ with $3,3^0$ accuracy	$(-110)_L \parallel (-110)_R$ with $1,3^0$accuracy	$[111]_L \in (-110)$ $[111]_R \in (-110)$	$[010]_L \parallel [010]_R$ with $1,3^0$ accuracy, $[100]_L \parallel [100]_R$ with $4,4^0$ accuracy, $[001]_L \parallel [001]_R$ with $5,9^0$ accuracy
R_2, L_2	$[-111]_R \parallel [111]_L$ with $0,1^0$ accuracy	$(101)_R \parallel (0-11)_L$ with $5,7^0$accuracy $(0-11)_R \parallel (-101)_L$ with $11,6^0$accuracy	$[-111]_R \in ((101)_R$ $(0-11)_R$ $[111]_L \in ((0-11)_L$ $(-101)_L$	$[100]_L \parallel [0-10]_R$ with $0,1^0$ accuracy, $[010]_L \parallel [100]_R$ with $7,6^0$ accuracy, $[001]_L \parallel [001]_R$ with $8,6^0$ accuracy
	$[1-11]_R \parallel [-1-11]_L$ with $0,1^0$ accuracy	$(-101)_R \parallel (011)_L$ with $5,2^0$accuracy $(011)_R \parallel (-101)_L$ with $0,1^0$accuracy	$[1-11]_R \in ((-101)_R$ $(011)_R$ $[-1-11]_L \in ((011)_L$ $(-101)_L$	
R_3, L_3	$[010]_R \parallel [010]_L$ with $0,1^0$ accuracy	$(-101)_R \parallel (-101)_L$ with $5,7^0$accuracy $(101)_R \parallel (101)_L$ with $5,7^0$accuracy $(001)_R \parallel (001)_L$ with $5,7^0$accuracy $(100)_R \parallel (100)_L$ with $11,6^0$accuracy	$[010]_R \in ((-101)_R$, $(101)_R$, $(001)_R$, $(100)_R$. $[111]_L \in ((-101)_L$, $(101)_L$, $(001)_L$, $(100)_L$.	$[11-1]_R \parallel [11-1]_L$ with $12,7^0$ accuracy

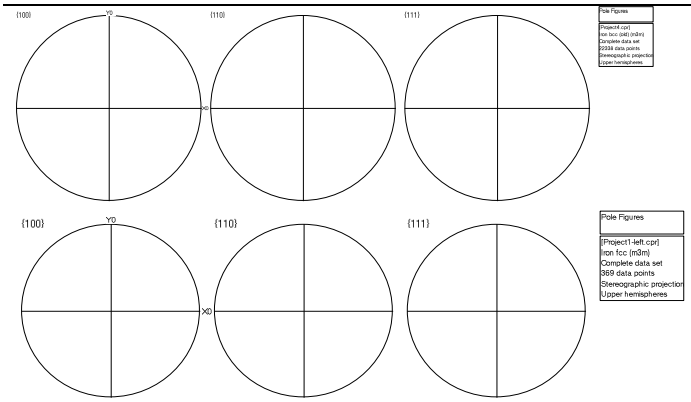

Fig. 3. Pole Figures for Bcc-phase (a) and Fcc-phase (b) in Hoba (corresponds to the data for Tawallah Valley (Goldstein., Michael, 2006).

For Chinga and Hoba meteorites at least one of two Bcc-phase orientations, which produce Schlieren Bands contrast, corresponds to octahedrite direction of the <111> of the initial Fcc-phase. For Iquique and Cape of Good Hope it is the minor third orientation.

The main Bcc-phase orientations satisfy the K-S orientation relationship with 4-6° accuracy (Badekha, 2012). The authors (Gundirev et al., 2003) investigating Chinga with X-ray diffraction found 12 Bcc- orientations, and one of them was connected by the inverse N-W (or Pitch) orientation relation, and with the accuracy of $5{,}26^0$ the K-S relation with the initial Fcc-phase. That points out to the martensitic type of the phase transformation in the initial Fcc-monocrystal.

It was checked that the pairs of the orientations are not the twins (Khlebnikova et al., 1997; *Buchwald,* 1981), that was prouved in the current study. The accuracy of twinning is more than 20^0. For all the meteorites there is a slight shift – not more than 8^0 - of the 3 Bcc-orientations set in each Schlieren band during the rotation around [110]Bcc. Comparing these data with martensitic steel features (Khlebnikova et al., 1997), it is important to note that the angels up to 8^0, observing by EBSD method, are small-angle borders between martensite crystals inside the package (set), (111) Fcc-plane corresponding to [110] Bcc direction, is the plane of the first shift during the martensitic transformation, and it defines the type of the package. At these terms only four types of packages may exist inside one Fcc-monocrystal – similar the lath-martensite in steel (Khlebnikova et al., 1997).

Conclusion. EBSD method reveals the set of 3 orientations of the Bcc-subgrains in each Sheer Zone, rotated around one axis due to the orientation relationship performing, that corresponds to the structure of the lath martensite. We propose that the phase transformation in the Fe-based alloys monocrystals are accompanied by the formation of the sheer zones, which are the consequence of different orientation of the Bcc-martensite packages in the unfinished martensite transformation process: $\gamma \rightarrow \alpha_2 + \gamma_{residual} \rightarrow \alpha + \gamma + \gamma_{residual}$.

The authors are grateful for World History Museum, Dedovsk, for the providing of Cape of Good Hope sample. The research was carried out in terms of Ministry of Science and Higher Education of Russian Federation Project № FEUZ-2020-0059.

References

Badekha K. A., Grokhovsky V. I., Yakovlev G. A.. Study of Schlieren bands in the ataxites using EBSD method// Meteoritics and Planetary Science. - 2012. - V. 46. № S1. - P. A49.

Buchwald V. F. *On the Oriented Sheen* in Ataxites / *Buchwald*, V. F. // Meteoritics. - 1981. - Vol. 16. - P.298-299.

Buchwald, V.F. Handbook of Iron Meteorites. Berkeley: University of California Press. - 1975. – P. 1418

Goldstein, J.I., Michael, J.R. The formation of plessite in meteoritic metal // Meteoritics and Planetary Science. – 2006. - vol. 41, № 4. - P. 553-570

Khlebnikova Yu.V., Schastlivtsev V.M., Rodionov D.P.// Physics of Metals and Metallography. - 1997. – 83.- P.640-646

Gundyrev V. M., Teplov V. A., Kabanova I. G., Kar'kina L. E., Khlebnikova Yu. V., Tabatchikova T. I., Shchegoleva N. N. Textural State and Crystallographic Features of the BCC and FCC Phases of the Chinga Meteorite (Fe–17% Ni) // Physics of Metals and Metallography. — 2003. — V. 95. — P. 174—181.

Barenbaum A.A.[1], Shpekin M.I.[2] Cumulative hypothesis of formation on the moon of the south pole-aitken basin by galactic comets UDC: 550.2: 523.4-1/-8

[1]*Oil and Gas Research Institute RAS, Moscow* (azary@mail.ru),

[2]*Kazan Federal University, Kazan* (michaels1@yandex.ru)

Abstract. The hypothesis is proposed that the unique South Pole – Aitken basin on the Moon could arise as a result of the last four cometary bombardments of the Moon by galactic comets as a result of the cumulative mechanism of crater formation.

Keywords: South Pole –Aitken basin on Moon; galactic comets; cumulative mechanism of crater formation.

Introduction The South Pole–Aitken Basin (SPA) is one of the largest impact structures not only on the Moon, but throughout the Solar System. It was discovered half a century ago (Rodionov et al., 1971) by the Soviet space stations Zond-6 (1968) and Zond-8 (1970). But even today its origin remains obscure.

The SPA basin is elliptical in shape and is located in the southern hemisphere on the far side of the Moon (Fig. 1). It got its name from the names of two objects on its opposite sides: the Moon south pole and the Aitken crater. The basin has young craters and smaller sea basins, and under its bottom there is an excess of dense rocks that do not give the Bouguer gravity anomaly, as in ordinary mascones (James at., 2019).

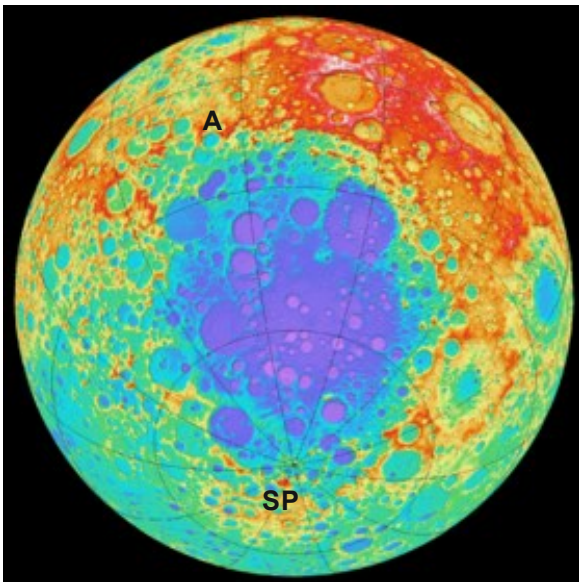

Fig. 1. Map of the heights of the moon. The South Pole–Aitken Basin on the far side of the Moon. Designated: SP – South Pole, A – Aitken crater

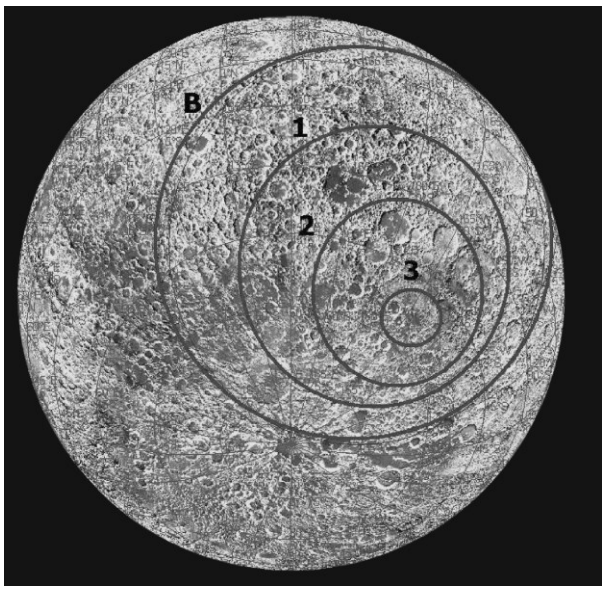

Fig. 2. Rings in multi-ring structure of SPA basin, plotted on Moon image with a central meridian of 160° west longitude (Shevchenko et al., 2007)

Several misaligned rings (Fig. 2) are distinguished in the structure of the basin (Shevchenko et al., 2007) at different topographic heights. Rings differ in diameters and composition of rock. Ring "B" denotes a shaft with a diameter of 3500 km that surrounds the SPA basin and which can be traced along the ridge system in the northwestern, northern, northeastern, and eastern parts of the basin (Shevchenko et al., 2007). At a number of points, the shaft reaches a height of H = 8 km. The substance of its rocks, as well as the elevated area located behind it, has anorthosite composition typical of the rocks of the upper part of the Moon's crust.

The ellipse "1" with a major semi-axis of 970 km corresponds to a profile with H = 0 km, which corresponds to the spherical surface of the Moon with a radius of 1738 km. This ellipse determines the actual size of the SPA basin. Its center has coordinates 53° south latitude and 169° west longitude.

The ellipse "2" corresponds to a profile with the mark of H = –4 km. Its semi-major axis is ≈640 km, and the center is even more shifted south relative to the "B" ring. The rocks of the basin to a depth of ≈4 km contain more Fe and Th, which indicates the presence of material of the middle and lower crust of the Moon.

Ring "3" with a radius of ≈200 km separates the deepest part of the basin, starting from H = –6 km. The center of this ring is displaced from the center of the ring in a southeast direction by already ≈730 km. Moreover, the composition of the rocks up to depths of H = –8 km differs little from the rocks of the overlying layer.

Hypotheses of SPA basin origin There is no generally accepted explanation of the origin of the SPA basin. It is believed that the basin could have formed 4.2–4.3 billion years ago as a result of the fall of a very large asteroid onto the Moon (Hiesinger et al., 2012). In this case, one could expect the presence in the basin of a large amount of mantle material from depths of ~ 200 km. Such material, however, is absent both in the pool itself and on the surface around the pool. Therefore, it is believed that the fall occurred at a small angle (~30°) to the lunar surface (Wieczorek et al., 2012). An argument in favor of this assumption is also the presence of an elevated area above all in the northeast, as well as in the northwest of the basin (Fig. 1).

At the same time, judging by the displacement of the rings, the authors of the work (Shevchenko et al. 2007) found that the impactor could move almost perpendicular to the plane of the ecliptic. The angle of its fall to the Moon was ~75°. This displacement is

interpreted as a trace of the trajectory of the impactor immediately before contact with the lunar surface. The authors also concluded that the impactor was most likely not an asteroid, but a comet type body.

The question of the nature of the fallen body that formed the SPA basin, however, has not been resolved. According to (Byrne, 2005), the impactor could relate to a different population of cosmic bodies than bodies, as a result of which all other basins on the Moon were formed.

A new approach to solving the problem In the works (Barenbaum, Shpekin 2018, 2019), we showed that large craters and sea basins on the Moon, as well as Mars and Mercury, were not created by the falls of interplanetary asteroids, as it is believed today (Melosh et al., 2013), but at a result of bombardments by high-speed comets of galactic origin. The bombardments are in the nature of intense cometary showers lasting ≈1-5 million years, which occur during the periods of the sun's stay in the jet streams and spiral arms of the Galaxy and are repeated after ≈20-37 million years. Wherein, after 150 million years, galactic comets alternately bombard the southern and northern hemispheres of the planets (Barenbaum, 2010).

As a result, most craters 10–180 km in diameter and basins larger than 180 km in size on the Moon, Mars and Mercury arose during the last one and to a lesser extent during the two or three previous cometary bombardments, when comets mostly fell in the southern hemisphere of the planets.

The last bombardment took place 5-1 million years ago, when the Solar system was in the stream of galactic comets near the Sun – in the branch of Orion-Cygnus. According to our estimates (Barenbaum, 2019; Barenbaum, Shpekin, 2020), the flux density of these comets was $\Phi \approx 5\times10^{-10}$ (year km^2)$^{-1}$, and their density of incidence on Moon, Earth and other planets was $\approx 2\times10^{-3}$ km^{-2}.

Given the density of comets falling on the south pole of Moon and Mercury, which have no atmosphere, and Mars, which has a very rarefied gas shell, the craters from the fall of many comets overlapped each other, which led to an increase in the depth and size of the resulting impact structure. We called this mechanism of the formation of the largest craters and sea basins "cumulative" (Barenbaum, Shpekin, 2018).

We believe (Barenbaum, Shpekin, 2020) that such a "cumulative mechanism" can also explain the origin of the SPA basin on the Moon.

Confirmation of the cumulative hypothesis We will perform the following elementary calculation. We will calculate the number of galactic comets that fell in the SPA basin in accordance with their flux density in the Orion-Cygnus branch $\Phi \approx 5\times10^{-10}$ (year km^2)$^{-1}$, and find their kinetic energy. Let us take the basin radius R = 2000 km, the average energy of comets $E_k \approx 5\times10^{21}$ J and the duration of their bombardment $\Delta t = 4$ million years. Then, during this time, number $N = \pi R^2 \Phi \Delta t \approx 6\times10^3$ comets with full energy $E_\Sigma = N E_k = 3\times10^{25}$ J can fall into the basin.

This energy could well go to the formation of the SPA basin. To answer the question whether this energy is enough for this or not, we compare the value of E_Σ with the energy of the ejection of rocks from the pool during the formation of its bowl. Let us consider the most extreme case, when all substance ejected from a basin bowl acquires a second cosmic velocity equal to $v_2 = 2.4$ km/s on the Moon and leaves the Moon. The energy required for this will be $E = Mv_2^2/2$, where M is the mass of the ejected substance. Assuming the basin depth H = 6 km, its area $S = 3\times10^6$ km^2, and assuming that the rocks consisted of anorthosite with a density $\rho = 3.3$ g/cm^3, we obtain the rock volume $V = SN = 1.9\times10^7$ km^3, their mass $M = \rho V = 6.2\times10^{19}$ kg and the energy required to eject rocks from the SPA basin, $E = 1.8\times10^{26}$ J.

According to (Melosh, 1989), when impact craters are formed, only a small amount of material from the near-surface region of the crater is ejected at a speed exceeding the first cosmic velocity on the planet. The bulk of the rocks have a significantly lower ejection rate, which prevents the rock fragments from moving far from the crater.

These discarded rock fragments may explain the existence of the rampart surrounding the SPA basin, as well as the origin of the higher terrain in the northeast of the basin. Therefore, if we assume that the bulk of the matter was ejected from the SPA basin at a speed an order of magnitude lower than the second cosmic one for the Moon, then the energy required for the formation of the basin will decrease by 2 orders of magnitude and become equal to ≈ 5% of the total energy of galactic comets $E_\Sigma = 3\times10^{25}$ J.

Even taking into account the fact that each of the 6,000 galactic comets that fell down into the SPA basin, was able to vaporize, melt, and heat rock mass several times higher than mass of the comet (Melosh, 1989), the energy intensity of these processes will not exceed the several first percent of energy E spent on the formation of the SPA basin bowl as a whole.

This calculation shows that the SPA pool can form galactic comets well. Earlier (Barenbaum, Shpekin, 2011, 2019a), we found that many large craters and marine basins of the southern hemisphere on the opposite side of the Moon, in particular, Aitken and Tsiolkovsky craters, as well as the Orientale mares could have occurred during the last comet bombardment 5-1 million years ago.

Figure 1 is clearly seen that these structures are located within the vast highlands surrounding the SPA basin from the north-east, north, and north-west, which, we believe, partly consists of rocks ejected

during the formation of the basin. Therefore, the age of the UPE basin is older than 5 million years, and it itself could well begin to form during the three previous comet bombardments of the southern hemisphere of the Moon, which took place in the ≈ 23, ≈ 40 and ≈ 65 million years ago (Barenbaum, 2010).

In connection with this, a weighty argument in favor of our hypothesis is the displacement of the basin rings in the southeastern direction (Shevchenko et al., 2007). When the Sun moves in a galactic orbit, the angle between the plane of the ecliptic and the direction toward the Galaxy center, where the galactic comets come from, changes. Wherein, the angle between the equator of the Moon and the direction of incidence of comets on it also changes in a certain way. According to calculations (Barenbaum, 2002), for the last bombardment this angle was close to 58°, while for the previous three bombardments it was 54°, 45° and 35°, respectively.

This calculation is quite consistent with the nature of the displacement of the ring centers in the SPA basin (Fig. 2) according to data (Shevchenko et al. 2007). Therefore, it can be assumed that the SPA basin was formed as a result of the last four bombardments of the Moon by galactic comets. The reason for its occurrence was a powerful comet bombardment, which took place on the border of the Mesozoic and Cenozoic 65 million years ago. The maximum density of comets falls fell on the region of latitudes close to the center of the "B" ring, where at that time the axis of rotation of the moon passed. During the three subsequent bombardments, the axis of rotation of the Moon and, as a consequence, it south pole moved step by step to their current position, occupying positions that coincided with centers of the rings "1", "2" and "3".

Conclusion A hypothesis is proposed according to which the South Pole-Aitken basin on the Moon arose under the influence of falls of galactic comets. This hypothesis differs from other known hypotheses in that:

1. The SPA basin on the Moon was created not by the impact of one large cosmic body that fell, but as a result of the multiple bombardments of the Moon by high-speed galactic comets during periods of the Solar system being in the jet streams of the Galaxy.

2. The physical mechanism of the formation of the SPA basin under impact of bombardments by galactic comets is similar to the "cumulative mechanism" (Barenbaum, Shpekin, 2020) of the creation by these comets on the Moon, as well as on Mars and Mercury, of sea basins larger than 180 km. The main difference is that the SPA basin was not formed as a result of one, but of last four comet bombardments.

3. The elliptical shape and specific ring-shaped structure of the basin is not caused only by the oblique incidence of galactic comets, but also by an increase in the angle of their incidence relative to the modern plane of the equator of the Moon during each subsequent bombardment.

4. The formation time of the SPA basin should be considered Cenozoic, which is the age of the basin is 65 million years.

References

Barenbaum A.A. Galaxy, Solar System, Earth. Subordinated Processes and Evolution, 2002, (PH: GEOS, Moscow) 353 p.

Barenbaum A.A. Galaxycentric Paradigm in Geology and Astronomy, 2010, (PH: Librokom, Moscow) 546 p.

Barenbaum A.A. Craters and seas on Mars and the Moon as a source of information about the flow of galactic comets in the Orion-Cygnus branch and the frequency of their precipitation on the planets of the Solar System // Materials of the XX International Conference: Physicochemical and Petrophysical Studies in Earth Sciences. 2019. (IGEM RAS, Moscow) P. 22-26.

Barenbaum A.A., Shpekin M.I. About age of the lunar surface // Vestnik Otdelenia Nauk o Zemle RAN, 2011, №3, NZ6011, doi:10.2205/2011NZ000141.

Barenbaum A.A., Shpekin M.I. Cumulative formation of mares and mascons on Moon by galactic comets // Night Moscow Solar System Symposium, Moscow: IKI RAS, 2018, 9MS3-PS-81.

Barenbaum A.A., Shpekin M.I. Origin and formation mechanism of craters, seas and mascons on the Moon // Journal of Physics: Conf. Ser. 1147, 2019, 012057. doi:10.1088/1742-6596/1147/1/012057.

Barenbaum A.A., Shpekin M.I. Estimation of the flux density of galactic comets in the Orion-Cygnus branch based on number of shield volcanoes on Venus, craters on Mars and marine basins on the Moon // Journal of Physics: Conf. Ser. 2020 (in press).

Byrne C.J. Size distribution of lunar basins // Lunar and Planet Sci. Conf. XXXVI. 2005. 1260.

Hiesinger H., van der Bogert C.H., Pasckert J.H., Schmedemann N., Robinson M.S., Jolliff B., Petro N. South pole–Aitken basin: Crater size-frequency distribution measurements // European Planetary Science Congress. 2012. (id. EPSC2012-832: journal) p.56

James P.B., Smith, D.E., Byrne P.K., Kendall J.D., Melosh H. J., Zuber M.T. Deep Structure of the Lunar South Pole–Aitken Basin // Geophysical Research Letters. 2019. Online version first published: 27 May 2019 (10): 5100–5106. doi:10.1029/2019GL082252.

Melosh H.J. Impact Cratering. A Geological Process, 1989, New York: Oxford University Press Inc.

Melosh H.J., Freed A.M., Johnson B.C., Blair D.M., Andrews-Hanna J.C., Neumann G.A., Phillips R.J., Smith D.E., Solomon S.C., Wieczorek M.A., Zuber M.T. The origin of lunar mascon basins // Science. 2013, Vol. 340, Issue 6140, pp. 1552–1555. doi: 10.1126/Science. 1235768.

Rodionov B.N., Isavnina I.V., Avdeev Yu.F., Blagov V.D., Dorofeev A.S., Dunaev B.S., Ziman Ya.L., Kiselev V.V., Krasikov V.A., Lebedev O.N., Mikhailovskii A.B., Tishchenko A.P., Nepoklonov B.V., Samoilov V.K., Truskov F.M., Chesnokov Yu.M. and Fivenskii Yu.I. // Cosmic. Res. 1971, Vol.9, p. 410–417.

Shpekin M.I., Barenbaum A.A. On mechanism and time-formation of Lunar mascons // Experiment in Geosciences. 2017, V.23, № 1, P. 60-63.

Shevchenko V.V., Chikmachev V.I., Pugacheva S.G. Structure of lunar basin South Pole–Aitken // Astronom. Vestnik. 2007. Vol. 41, №6, p. 447–462. https://doi.org/10.1134/S0038094607060019

Wieczorek M.A, Weiss B.P, Stewart S.T. An impactor origin for lunar magnetic anomalies // Science. 2012. V.335 (6073). P. 1212–1215. doi:10.1126/science.1214773.

Barenbaum A.A.[1], Titorenko A.[2] Optimized galactic model of geological cyclicity and its testing on geology and astronomy data UDC 550.93, 551.7,523.525, 524.66

[1]*Oil and Gas Research Institute RAS, Moscow* (azary@mail.ru),

[2] Russian State University of Oil and Gas, Moscow (ya.titorenko7@yandex.ru)

Abstract. The parameters of the galactic model of geological cyclicity were optimized, which ensured the best fit of the calculation results to the geology and astronomy data. The model is confirmed by data of the International Stratigraphic Chart and the General Stratigraphic Scale, and was also verified by comparing with data of astronomy a number parameters of the spiral construction Galaxy, as well as distance between the Sun and the Galaxy center, that were calculated according to the model.

Keywords: *Galactic model of geological cyclicity; International and General stratigraphic scales; Galaxy spiral structure.*

Introduction Continuing the conclusions (Barenbaum, 2018), we optimized the parameters of the galactic model of geological cyclicity (Barenbaum, 2010). This model allows calculating age of the borders of the stratigraphic scale for Phanerozoic and Precambrian based on the analysis of the Sun movement in the Galaxy. The purpose of the work was to:

- Develop a more accurate algorithm than in the model (Barenbaum, 2010) for calculating parameters of the Sun galactic orbit and the time when the Sun crosses jet streams and spiral arms of the Galaxy.

- Optimize the parameters of the solar orbit and galactic arms, ensuring the best agreement of calculations with data of the International Stratigraphic Chart (ISC) and the General Stratigraphic Scale of Russia (GSS) for the Phanerozoic and Precambrian.

- Clarify the values of a number of design parameters of the Galaxy, which are difficult or impossible to measure using astronomical methods.

Galactic model According to the galactic model (Fig. 1), the spiral structure of our Galaxy is formed by two branch systems, one with a logarithmic and the second with an Archimedean type of spirals. The first system consists of four galactic arms, and the second consists of two gas-dust jets.

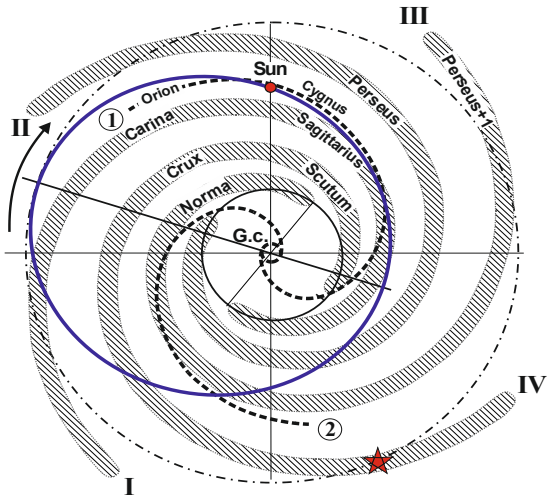

Fig. 1. The current position of the Sun in orbit (ellipse) relative to four galactic arms (Roman numerals) and two jet streams (Arabic numerals in circles) in projection onto the plane of the Galaxy. The orbit is shown for the last revolution of Sun around the Galaxy center (G.c.). The small circle in the center, where the jet streams flow out, is the nuclear disk. The larger circle where the galactic arms begin determines the size of the Galaxy isothermal core. The outer dotted ring corresponds to the corotation radius R* of our Galaxy. The arrow indicates the direction of the Sun moving on orbit, which coincides with rotation of the Galaxy and rotation of the line apsid (straight line) of the Sun orbit. The asterisk shows the place in the arm Crux-Scutum (IV) where the Solar system was formed earlier.

The galactic arms are described by the formula $R(\varphi) = Ro\{\varkappa[\varphi+(2k–1)/4]\}$, where: k = 1–4 is the arm number; $\varkappa = ctg(\mu)$ is parameter that characterizes the swirl angle of the arms, uniformly rotated around the Galaxy center with a period T_G.

The formula of jet streams has the form $R(\varphi) = V_s(t+\varphi/\omega_d) = V_s t + \rho\varphi$, where V_s is rate of flow out of matter from the nuclear disk, t is the time, $\omega_d = 2\pi/T_d$ is the angular velocity of the disk, T_d is the rotation period; $\rho = V_s/\omega_d$ is the parameter of swirling of jet streams. The disk is inclined to the Galaxy plane at an angle of 22° (Fizika kosmosa, 1986) and precesses with the period of rotation of the disk.

The value R* = ϰ/ρ defines the corotation radius of the Galaxy, at which the radiuses of curvature of the logarithmic arms and jet streams, swirled into Archimedean spirals are the same.

The Sun moves in the galactic plane in an elliptical orbit with a large semi-axis (α) and eccentricity (e), characterized by anomalistic (T_R) and sidereal (T_φ) rotation periods around the Galaxy center. The line apsid of solar orbit also rotates to the side of the Sun movement with some period (T). At this the Sun is periodical approaching the Galaxy center at a distance of $R_{min} = \alpha(1 - e)$, and it is moving away from it at a distance of $R_{max} = \alpha(1 + e)$. Simultaneously, the Sun makes vertical fluctuations relative to the galactic plane with a period T_d.

Due to the movement of the Sun and different speeds of rotation of the nuclear disk and galactic arms, their position changes over time. As a result, the Sun quasiperiodically crosses the spiral arms and jet streams of the Galaxy, and then the Solar system is bombarded by galactic comets for a period of ~2÷5 million years, and of different intensity.

In the Earth history the times of such bombardments are epochs of global natural catastrophes: biotic, climatic and tectonomagmatic. Their time is fixed by geologists in the geochronological scales of the Phanerozoic and Precambrian, as their borders of different ranks. The galactic model allows us to calculate the age of these borders, starting with the rank of systems.

This model is developed and improved for over 30 years, having undergone several modifications. Currently, with its help, the principle of constructing a stratigraphic scale has been explained (Barenbaum et al., 2002) and the time of main Precambrian events has been clarified (Barenbaum, 2018).

Today in Russia, two geochronological scales are used GSS and ISC, which differ in age of borders of the same name stratons. Despite all efforts, it is not possible to eliminate the contradiction between the scales (Alekseev, 2015, Zhamoyda, 2015). Optimization of the galactic model solves this problem.

Galactic model optimization approach An analysis of GSS and ISC shows (Barenbaum, 2018) that all 15 borders of the Phanerozoic systems coincide in time with bombardments of the Earth by comet streams when the Sun was either in one of four galactic arms (12 events) or when it crossed the Galactic plane (3 events). This circumstance allows us to introduce a measure of "deviation" of the model. For the first events, this measure we will take the Sun distance (ΔR_i) to middle of the nearest to it galactic arm. And for the last three events the Sun distance of between its position at a given moment of time and the Sun position at nearest moment time, multiple of period of 25 mln years.

Based on all 15 "deviations" ΔR_i, their average value was found

$$\Delta\bar{R} = \sqrt{\frac{1}{15}\sum_{1}^{15}\Delta R_i^2}\,, \qquad (1)$$

This "standard deviation" was as a criterion for adequacy of the model. The model with smallest $\Delta\bar{R}$ value was considered the best, and this value itself was as indicator of the average width of galactic arms.

To limit the number of optimized parameters, all the model parameters included in the formulas for calculating the Sun galactic orbit and of the times when the Sun crosses jet streams and galactic arms were divided into two groups. The parameters of the first group were considered reliably established in previous versions of the model, and the parameters of the second group needed to be clarified.

The **"established"** model parameters were considered to be:

1. The model of Galaxy according to J. Vallee (2017), consisting of four logarithmic arms with the twist parameter of spirals ϰ = ctg μ, where μ is the twist angle.

2. Two jet streams twisted into Archimedean spirals with the parameter ρ = 2.48 kpc/rad, flowing out of a precessing nuclear disk with a rotation period T_d = 50 mln years.

3. Movement of the Sun on elliptical orbit, the apse line of which turns around the Galaxy center in direction of the Sun movement. The anomalistic and sidereal rotation periods of the Sun T_R = 250 min years and T_φ = 222.223 mln years. The Sun orbit lies in the Galaxy plane. And the Galaxy itself as a whole rotates evenly around the center with a period of T_G = 200 mln years.

4. Fixing the Sun position in orbit at two moments in time. The first moment was 2 ± 1 mln years ago, when the Sun was in the Orion-Cygnus jet stream; and the second moment was 567 ± 1 mln years ago, when the Sun crossed centerline of the arm Crux-Scutum (IV) at a distance of the corotation radius R* from the Galaxy center (see Fig.1) .

The "**refined**" model parameters were:

5. The distance $R_\odot$ of the Sun and the Galaxy center.

6. The modern position of the Sun relative to the Carina-Sagittarius (I) and Perseus (II) arms.

7. Large semi-axis (α) and eccentricity (e) of the Sun orbit, connected by the condition:

α(1+ e) = ρ/ϰ, which means that the Sun reaches R * at the point R_{max}.

8. The initial angles of rotation the line of apsid solar orbit, as well as of four exit points of galactic arms from central ring and two jet streams from nuclear disk, ensuring conditions 4 and 7 are satisfied.

Optimization result A program was developed to calculate the time when the Sun crosses the stream

jets and galactic arms in the above conditions. The search for optimal model parameters that minimize the value $\Delta\bar{R}$ is automated. The calculations were carried out with variation of parameters: 1) distance $R_\odot$ varied from 7.8 to 9.0 kpc with a step of 0.05 kpc, 2) angle μ from 70° to 90° with a step of 0.05°, and 3) eccentricity of solar orbit from $0.34 \le e \le 0.42$ in increments of 0.05. Large semi-axis α solar orbit and the initial angle of rotation its line of apsid automatically determined from conditions 4 and 7.

The speed and acceleration of the Sun movement were calculated. The calculations were tested using data from geology and astronomy. A total of more than 100 thousand calculations were performed.

Optimization consisted in minimizing value $\Delta\bar{R}$ for each of variable parameters while iterating through the values of all other parameters of the model. Processing of the calculation results showed that there is an optimal set of parameter values that provide a minimum of discrepancy at the $\Delta\bar{R} \cong 0.4$ kpc level. The optimal values are: $R_\odot$ = 8.35±0.05 kpc, μ = 77.8 ±0.05°, e = 0.37±0.005 and α = 8.373 kpc.

Testing the model based on geology data In Fig. 2, the calculated moments of the Sun intersection of the jet streams and galactic arms are compared with the borders Phanerozoic of the rank of systems in GSS-1993 (red vertical lines) and periods in ISC-2020 (blue lines). The absolute age of the same borders of both scales is shown at the bottom of the figure. The general division of the Phanerozoic into eras is also given there.

Periodic curve is the Sun orbit, shaded stripes are the galactic arms, and Roman numerals are numbers of the galactic arms. Icons with numbers on solar orbit indicate the times when the Sun crosses jet streams (circles) and simultaneously the galactic arms (squares). If at this time the propagation of jet streams coincides with the Galaxy plane, then such events are shown by black icons. The width arms are assumed to be $2\Delta\bar{R}$ = 0.8 kpc, where multiplication by 2 corresponds to a 95% confidence interval.

Horizontal dash-and-dot line shows corotation radius R* =11.47 kpc. During the epochs 566.5 and 66.5 mln years ago, when the Sun was located in the arms Perseus 1 (III) and Crux-Scutum (IV) at a distance R*, major geological events occurred on Earth, which served as the basis for their identification as beginning of the eras Paleozoic and Cenozoic. An event similar in consequences for the biosphere took place 251 mln years ago in the arm Perseus (II) that was the beginning of the Mesozoic era.

Despite the different ages of some borders of the same name in the GSS and ISC, the calculations are quite consistent with the data of both scales. The epochs of comet bombardment, if they do not always coincide with the borders of the GSS and ISC rank systems, are very close in time to these borders.

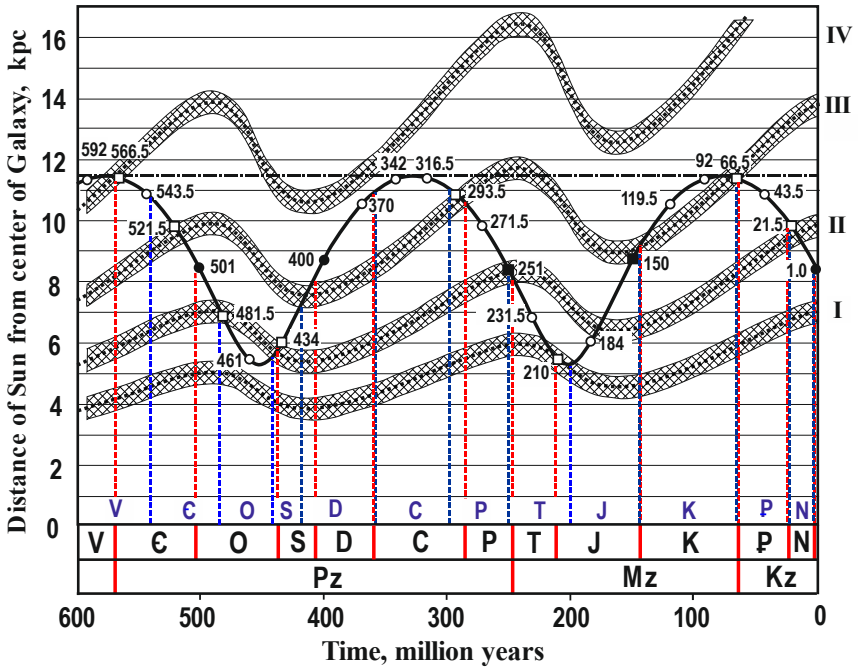

Fig. 2. Comparison of calculations the age of borders systems of the Phanerozoic with GSS-1993 and ISC-2020

Testing the model based on astronomy data The model was also tested using astronomy data. Below are the results of several astronomical tests.

Distance between Sun and Galaxy center: The dependence of standard deviation $\Delta\bar{R}$ on accepted value $R_\odot$ for optimal values μ = 77.8 ° and e = 0.37 is shown in Fig. 2. Calculation gives optimal value $R_\odot$ = 8.35 ± 0.05 kpc. The same figure shows value $R_\odot$ measured by astronomers: 1 – Gillessen et al (2009), 2 – Honma et al (2012), 3 – Gillessen et al (2013), 4 – Reid et al (2014), 5 – Bobylev and Baykova (2014), 6 – Grijs & Bono (2016), 7 – Grijs & Bono (2017), 8 – Vallee (2017), 9 – Camariolo et al (2018).

We see that $R_\odot = 8.35 \pm 0.05$ kpc agrees well with the one found by astronomers within the limits of their measurement errors. Our calculation gives preference to a group of points in area of 8.3 kpc.

Twist angle of galactic arms: The dependence of standard deviation $\Delta\bar{R}$ on twist angle μ for $R_\odot$ = 8.35 kpc and e = 0.37 is shown in Fig. 3. The graph indicates that the optimal angle is $\mu_{opt} = 77.8 \pm 0.05°$. The μ_{opt} was compared with measurements by

astronomers. In astronomy, the degree of swirling of the galactic arms is characterized by the angle *i*, which is associated with the angle μ by the ratio $i = \mu - 90^o$. Astronomers ' measurements give $i = -12.9\pm2.9^o$ (Bobylev, Baykova, 2014), -9.5 ± 0.1^o (Dambis et al., 2015), -10.6 ± 0.3^o (Rastorguev et al., 2017) and -13.6 ± 0.4^o (Valle, 2017). These measurement results, in terms of angle μ, lie to the left and right of the value μ_{opt}, and none of them falls into the field Fig. 3.

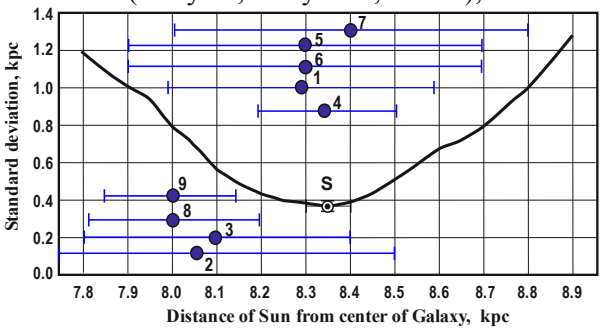

Fig. 3. Dependence of standard deviation $\Delta\bar{R}$ on Sun (S) distance to the Galaxy center at $\mu = 77.8°$ and $e = 0.37$

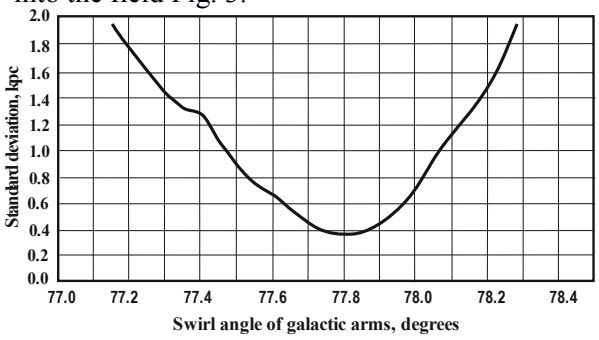

Fig. 4. Dependence of standard deviation $\Delta\bar{R}$ on twist angle μ of galactic arms at $R_\Theta = 8.35$ kpc and $e = 0.37$

Speed and acceleration of Sun: Change in speed and acceleration motion of the Sun in orbit cannot be determined from astronomical observations. However, the galactic model allows calculating them.

Fig. 5 shows the periodical change in the speed motion of the Sun relative to the Galaxy center in time. The speed of the Sun varies from V_{min}=186.5 km/s at maximum distance from the center R_{max} = 11.47 kpc, to V_{max}=332.0 km/s at minimum distance R_{min}=5.46 kpc. The average speed of the Sun is 273.1 km/s. At a given time (t = 0), its speed is V_Θ = 240.8 km/s. In the projection on the galactic plane, vector V_Θ makes the angle β = 19.45° with radius vector of the Sun.

Fig. 6 shows a similar graph for changing acceleration of the Sun. The graph shows that acceleration of the Sun movement changes with the same period T_R = 250 mln years. At the points of solar orbit R_{min} and R_{max}, the acceleration turns to 0, changing the sign. Currently, the Sun is moving to the perigalactic point of its orbit with an acceleration of +1.8 km/s in 1 mln years.

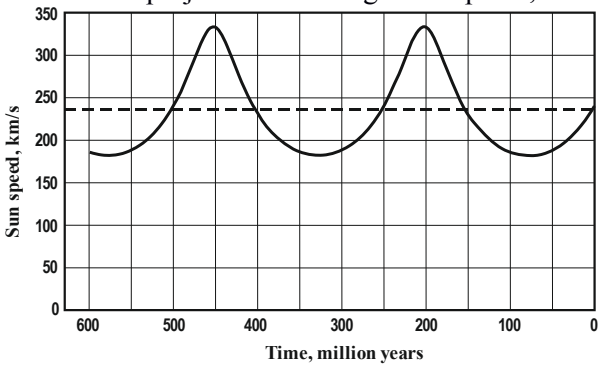

Fig. 5. Changes in orbital velocity of the Sun over time. Dotted line indicates average velocity

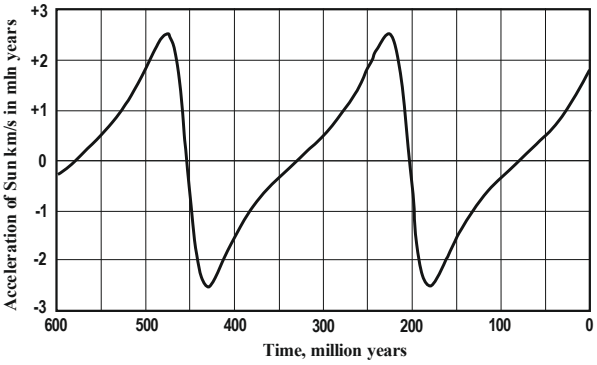

Fig. 6. The change in acceleration of the Sun over time

Gravitational potential of Galaxy: The found orbit of the Sun allows us to establish the distribution function of the gravitational potential U(R) in the plane of the Galaxy outside its isothermal core. The potential U(R) in our model can be represented as a series

$$U(R) = c_0\left[1+\left(\frac{R}{R_\Theta}\right)^{-1}+\frac{(1-\xi^2)p}{2R_\Theta}\left(\frac{R}{R_\Theta}\right)^{-2}+\ldots\right] \quad (cm/s)^2, \qquad (2)$$

where: $c_0 = M_0G/R_\Theta$ is a constant coefficient, $p = \alpha(1-e^2)$ is an elliptic parameter, $\xi = T_\varphi/T_R$, M_0 is the mass of the Galaxy inside the average radius of the Sun orbit ($\alpha = R_\Theta$), G is the gravitational constant.

In formula (2), first R-dependent term in square brackets defines the movement of the Sun in an elliptical orbit with parameters α and e, and the quadratic term characterizes the rotation of the apse

line of the solar orbit. In our model, the multiplier in front of this member is equal to 0.091.

The value of c_0 can be calculated using average quadratic velocity of stars in the isothermal sphere of the Galaxy as $c_0 = \frac{2}{3}\overline{V}^2$, where $\overline{V}$ =260 km/s, and in that case $c_0 = 4.5\times10^{14}$ (cm/s)^2 (Barenbaum, 2002). A can be found by the parameters of the Sun's orbit as $c_0 = L^2/pR_\Theta$, where L is the moment of the amount of movement of the Sun relative to the center of the Galaxy. Taking R_Θ = 8.35 kpc, e = 0.37 and α = 8.373 kpc, we get $p = 2.58\times10^{22}$ cm. Currently, $L = V_\Theta R_\Theta \mathrm{Cos}(\beta) = 5.094\times10^{29}$ cm/s. Substituting the values R_Θ, p, and L, we find $c_0 = 4.50\times10^{14}$ (cm/s)^2.

The value c_0 coincides with the one calculated in the first way. The mass of the Galaxy inside the radius of the Sun's orbit, calculated as $M_0 = c_0R_\Theta/G = 0.875\times10^{11}\ M_\Theta$, is in good agreement with the results of other authors $M_0 = (1.0–1.4)\times10^{11}M_\Theta$ at distance R_Θ = 10 kpc.

Conclusion A more advanced version of the galactic model of geological cyclicity was developed. The model allows you to build a universal geochronological time scale for the Phanerozoic and Precambrian, as well as to clarify the distance of the Sun to the center of the Galaxy and its spiral structure.

The main results are as follows:

- A new approach to the construction of chronostratigraphic scales of the Phanerozoic and Precambrian was developed, taking into account the bombardments of the Solar system by galactic comets.
- A spiral model of the Galaxy has been constructed that best matches the results of astronomical observations and geological data.
- The distribution of the gravitational potential in the Galaxy plane outside the isothermal core is established.

References

Alekseev A.S. (2015) International stratigraphic chart: state of the art // Russian Geology and Geophysics, V.56, №4, P. 524-531.

Barenbaum A.A. (2010) Galactocentric paradigm in geology and astronomy (Moscow, PH: LIBROCOM), 546 p.

Barenbaum A.A. (2018) Complexing the data of astronomy, geology and meteoritics at development of the adequate spiral model of Galaxy // Experiment in Geosciences, V.24, №1, P.12-15.

Barenbaum A.A., Gladenkov Yu.B., Yasamanov N.A. (2002) Geochronological scales and astronomic time (state of art) // Stratigraphy and Geol. Correlation, V.10, №2, 103-113.

Bobylev V.V., Baykova A.T. (2014) Analysis of galactic rotation from masers based on a nonlinear Oort model // Astronomy Letters, V.40, №12, P. 773-782.

Dambis A.K., Berdnikov L.N., Efremov Yu.N. et al. (2015) Classical cepheids and spiral structure of the Milky Way //Astronomy Letters, V.41, №9, P. 489-500.

Fizika kosmosa (1986) Little Encyclopedia / Ed. R.A. Syunyaev (Moscow, PH: Sov. Entsiklopediya), 783 p.

Zhamoida A.I. (2015) General stratigraphic scale of Russia: state of the art and problems // Russian Geology and Geophysics, V.56, № 4, P. 511-523.

Camarillo T., Varun M., Tyler M., and Bharat R. (2018) Publ. Astron. Soc. Pacific. 130, 4101.

Gillessen S., Eisenhauer F. Fritz T.K. et al (2009) Astrophys. J. V.707, №2, p. L114-L117.

Gillessen, S., Eisenhauer, F., Fritz, T. K. et al. (2013) Proc. IAU Symp., 289, 29.

de Grijs R., Bono G. (2016) Astrophys. J. Sup. Ser.,V.227, 5.

de Grijs R., Bono G. (2017) Astrophys. J. Sup. Ser.,V.232, 22.

Honma, M., Nagayama, T., Ando, K. et al. (2012) Publ. Astron. Soc. Japan, 64, 136.

Rastorguev A.S., Utkin N.D., Zabolotskikh M.V. et al. (2017) Galaxy masers: kinematics, spiral structure and dynamic disk condition // Astrophys. Bull., № 72, P.134-155.

Reid M. J., Menten K.M., Brunthaler A. et al. (2014) Astrophys. J. №2, 783, 130.

Vallee J.P. (2017) Astronomical Review, V.13, Issue 3-4, P.113-146.

Fisenko A.V., Semjonova L.F. Alternative composition of xenon components in nanodiamonds of meteorites. UDC 550.42

Vernadsky Institute of Geochemistry and Analytical Chemistry RAS, Moscow (anat@chgnet.ru)

Abstract. The contents of alternative xenon components — Xe-P3fr, Xe-P6, and Xe-pr — in the nanodiamond of meteorites of various chemical classes and petrological types are calculated. The Xe-pr component used instead of Xe-HL consists mainly of Xe isotopes formed in p- and r-processes of nucleosynthesis during a type II supernova explosion. The calculation results showed the following:
1. The main components of xenon in the nanodiamond are almost normal by the isotopic composition of Xe-P3fr and Xe-P6.
2. The relative content of Xe-pr in the nanodiamonds of thermally metamorphosed meteorites does not exceed 15% of the total xenon content in the diamond of each meteorite, which is significantly lower than that for Xe-HL (at least 65%).
3. Xenon components are in the order Xe-P3 <Xe-pr << Xe-P6 in terms of increasing the degree of preservation during thermal metamorphism. This indicates the xenon components are content in individual populations of diamond grains with different thermo-oxidative stability . The contents of the Xe components obtained under the assumption of the presence of Xe-pr or Xe-HL in the meteoritic nanodiamond are compared.

Keywords: meteorite , nanodiamonds, xenon components.

Introduction Xenon in meteorite nanodiamonds is usually taken as a mixture of such basic components as Xe-P3, Xe-P6 and Xe-HL (Huss,

Lewis, 1994a). At the same time, an alternative composition of this mixture consisting of Xe-P3fr, Xe-P6 and Xe-pr components is also possible (Fisenko, Semjonova, 2020). In both compositions, the Xe-P3, Xe-P3fr, and Xe-P6 components are similar to the composition of solar xenon. The isotopic compositions of the Xe-HL and Xe-Pr components are sharply anomalous due to the simultaneous enrichment by light and heavy isotopes. These components are different from each other in that Xe-HL is a mixture of normal and abnormal subcomponents, while the Xe-pr component consists mainly of Xe isotopes formed in p- and r-processes of nucleosynthesis during a type II supernova explosion. Therefore, the Xe-pr component is significantly more enriched in light and heavy isotopes than Xe-HL. We have shown that the use of the Xe-pr component instead of Xe-HL leads to a sharp decrease of the relative content of Xe-pr compared to Xe-HL in diamond of Orgueil (CI), Tieschitz (H3.6) and Indarch (EH3-4) meteorites (Fisenko, Semjonova, 2020). In this work, we present calculations of the contents of alternative components Xe-P3fr, Xe-P6, and Xe-pr in the total nanodiamonds of threaten meteorites of various chemical classes and petrological types, as well as their comparison with data obtained using the Xe-HL component.

Determination of the content of xenon components in meteoritic nanodiamonds.

A method of calculating the content of xenon components is given in (Fisenko, Semjonova, 2020). Here we note the following.

The content of alternative xenon components were calculated based on the measured contents of xenon and its isotopic composition in nanodiamonds of different meteorites in (Huss, Lewis, 1994a).

At the calculations, it was taken into account that the noble gases in the isolated diamond fractions also contain Xe-S, the phase-carrier of which are SiC nanograins. The calculations were carried out using the following equations:

$$X + Z + Y + V = [^{132}Xe]_m$$
$$(^{130}Xe/^{132}Xe)_{P3} \times X + (^{130}Xe/^{132}Xe)_{P6} \times Z + (^{130}Xe/^{132}Xe)_S \times V = (^{130}Xe/^{132}Xe)_m \times [^{132}Xe]_m$$
$$(^{134}Xe/^{132}Xe)_{P3} \times X + (^{134}Xe/^{132}Xe)_{P6} \times Z + (^{134}Xe/^{132}Xe)_{pr} \times Y + (^{134}Xe/^{132}Xe)_S \times V = =(^{134}Xe/^{132}Xe)_m \times [^{132}Xe]_m$$
$$(^{136}Xe/^{132}Xe)_{P3} \times X + (^{136}Xe/^{132}Xe)_{P6} \times Z + (^{136}Xe/^{132}Xe)_{pr} \times Y + (^{136}Xe/^{132}Xe)_S \times V = =(^{136}Xe/^{132}Xe)_m \times [^{132}Xe]_m,$$

where the variables X, Z, Y, V are the contents of ^{132}Xe-P3fr, ^{132}Xe-P6, ^{132}Xe-pr and ^{132}Xe-S, respectively. The subscripts P3, P6, S, and pr refer to the isotopic compositions of xenon components (Table 1), while m refers to the contents of ^{132}Xe and isotopic ratios of xenon, which we used based on meteorites measured in (Huss, Lewis, 1994a) during pyrolysis of nanodiamonds.

In calculating the contents of Xe components in the nanodiamond of all meteorites, we used mass fractionated Xe-P3 (0.99% / at. (Huss et al. 2008), designated as Xe-P3fr). It is possible that the low-temperature Xe-P3 in diamond of weakly thermally metamorphosed meteorites is not fractionated, but we did not take this into account in the calculations.

All calculations were carried out in result of normalizing the equations to the measured ratios ^{130,134,136}Xe / ^{132}Xe without the errors of their measurements. Therefore, the obtained contents of Xe components in meteorite nanodiamonds represent one of the options for their possible values. Nevertheless, a common method for determining these contents revealed the features of xenon components at using the Xe-pr component instead of Xe-HL in the calculations.

Results and discussion The calculated contents of the alternative components Xe-P3fr, Xe-P6 and Xe-pr in the nanodiamonds of various meteorites are shown in table 2.

Table 1. The isotopic compositions of the xenon components (^{132}Xe=100)

Components	$\frac{^{124}Xe}{^{132}Xe}$	$\frac{^{126}Xe}{^{132}Xe}$	$\frac{^{128}Xe}{^{132}Xe}$	$\frac{^{129}Xe}{^{132}Xe}$	$\frac{^{130}Xe}{^{132}Xe}$	$\frac{^{131}Xe}{^{132}Xe}$	$\frac{^{134}Xe}{^{132}Xe}$	$\frac{^{136}Xe}{^{132}Xe}$
Xe-P6[1]	0.438 ± 25	0.444 ± 28	8.90 ± 20	111.4 ± 8	16.60 ± 11	82.14 ± 47	32.91 ± 50	31.00
Xe-S[2]	0	0.033 ± 19	21.59 ± 14	11.8 ± 1.1	48.26 ± 42	18.6 ± 1.2	2.22 ± 53	0.34
Xe-P3fr	0.415	0.380	7.74	101.1	15.59	81.51	38.45	32.23
Xe-pr	43.35	19.29	139.5	553.4	0	374.80	2570	3833

[1] – Huss, Lewis, 1994a; [2] –Lewis et al., 1994.

Table 2. The content of xenon components and isotope ratios 124-129,131Xe for diamond

Sample	^{132}Xe-P3fr (^{132}Xe-P6)	^{132}Xe-pr ^{132}Xe-S)	$\frac{^{124}Xe}{^{132}Xe}$	$\frac{^{126}Xe}{^{132}Xe}$	$\frac{^{128}Xe}{^{132}Xe}$	$\frac{^{129}Xe}{^{132}Xe}$	$\frac{^{131}Xe}{^{132}Xe}$
Orgueil	47.92	0.132	*0.560(3)*	*0.452(2)*	*8.34(3)*	*105.7(3)*	*82.84(25)*
C(I)	1.407	0.33	0.526	0.428	8.201	101.7	81.79

Sample	^{132}Xe-P3fr (^{132}Xe-P6)	^{132}Xe-pr ^{132}Xe-S)	$\frac{^{124}Xe}{^{132}Xe}$	$\frac{^{126}Xe}{^{132}Xe}$	$\frac{^{128}Xe}{^{132}Xe}$	$\frac{^{129}Xe}{^{132}Xe}$	$\frac{^{131}Xe}{^{132}Xe}$
Semarkona	31.54	0.156	*0.631(3)*	*0.479(2)*	*8.57(3)*	*109.2(3)*	*83.30(25)*
LL(3.0)	1.287	0.16	0.616	0.470	8.472	103.2	82.60
Bishunpur	23.36	0.172	*0.721(4)*	*0.520(3)*	*9.01(3)*	*110.6(3)*	*83.59(25)*
LL(3.1)	1.742	0.15	0.705	0.511	8.794	104.4	83.17
Ragland	22.14	0.216	*0.773(4)*	*0.546(3)*	*9.01(3)*	*109.7(3)*	*83.95(25)*
LL(3.5)	2.920	0.002	0.784	0.547	9.00	106.1	84.08
M.Madaras	19.30	0.179	*0.760(4)*	*0.544(2)*	*9.44(3)*	*107.7(3)*	*83.87(25)*
L(3.5)	2.773	0.024	0.763	0.541	8.961	105.9	83.88
ALHA77214	20.92	0.206	*0.775(4)*	*0.540(4)*	*8.95(3)*	*107.3(3)*	*82.87(25)*
L(3.5)	3.328	0.007	0.779	0.548	9.01	106.3	84.03
Tieschitz	21.23	0.208	*0.771(6)*	*0.542(5)*	*9.02(3)*	*110.0(3)*	*84.01(25)*
H(3.6)	3.519	0.049	0.775	0.546	9.048	106.1	83.89
Qingzhen	20.57	0.202	*0.772(5)*	*0.553(4)*	*8.99(3)*	*106.4(3)*	*83.72(25)*
EH(3)	3.153	0.091	0.777	0.547	9.05	105.9	83.81
Indarch	23.78	0.263	*0.770(3)*	*0.545(4)*	*9.10(3)*	*106.7(3)*	*83.68(25)*
EH(4)	6.770	0.102	0.783	0.554	9.16	106.9	83.93
Leoville	23.08	0.191	*0.752(4)*	*0.533(3)*	*8.88(3)*	*112.4(3)*	*83.83(25)*
CV(3.0)	1.836	0.085	0.742	0.528	8.87	105.1	83.59
Vigarano	18.46	0.168	*0.770(4)*	*0.540(3)*	*8.99(3)*	*111.9(3)*	*84.01(25)*
CV(3.3)	1.864	0.020	0.769	0.542	8.94	105.7	83.92
Allende	21.36	0.221	*0.790(5)*	*0.551(5)*	*9.11(3)*	*107.3(3)*	*84.34(25)*
CV(3.2)	3.557	0.018	0.796	0.556	9.05	106.6	84.21
Kainsaz	20.62	0.192	*0.771(4)*	*0.540(3)*	*9.46(3)*	*107.0(3)*	*83.98(25)*
CO (3.2)	2.510	0.046	0.769	0.542	8.97	105.7	83.85

The reality of the calculated contents of the Xe components can follow from the degree of coincidence of the calculated isotope ratios $^{124\text{-}129,131}$Xe / ^{132}Xe with the measured ones. These ratios were calculated based on the contents of xenon components and their isotopic compositions (Tables 1, 2). On the base of data in table 2, we note the following. Deviations of the calculated ratios from the measured ones do not exceed mainly 1-2%, which may indicate the reliability of the calculated xenon components. In addition, this coincidence is a strong argument in favor of a single population of diamond grains containing light and heavy xenon isotopes formed in p- and r-processes of nucleosynthesis during a type II supernova explosion. The observed significant difference for Orgueil diamond is probably due to a significant fr content of the low-temperature Xe-P3, which we accepted mass fractionated. It is also likely that deviations of the calculated ^{129}Xe / ^{132}Xe ratios for diamond of some meteorites are due to the unaccounted for fraction of excess ^{129}Xe formed as a result of ^{129}I decay. The observed underestimation of the calculated ^{128}Xe / ^{132}Xe ratio only for to the Kainsaz and Mezo Madaras meteorites remains an open question. The calculated contents of xenon components using HL and pr components, as expected, differ significantly from each other. This can be seen from the data in Fig. 1, which shows the relative contents of xenon components obtained by us in this work and from the data in (Huss, Lewis, 1994b). In this figure, meteorites are located on the abscissa in the sequence of increasing temperature of their metamorphism. The dashed lines in Fig. 1 (and also in fig. 2) correspond to the temperature of metamorphism (330 °C) for the Leoville meteorite (Huss, Lewis, 1994b). One of the main results of the performed calculations is the revealed sharp decrease in the content of the Xe-pr component relative to Xe-HL in diamond of thermally metamorphosed meteorites.

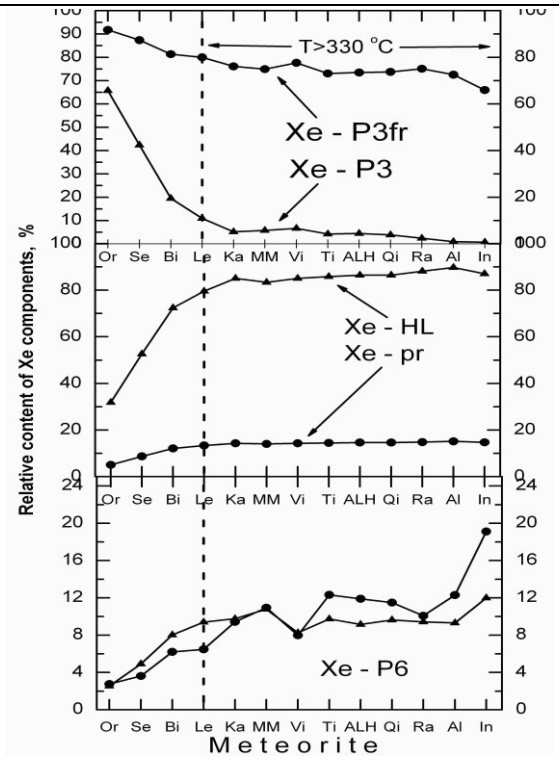

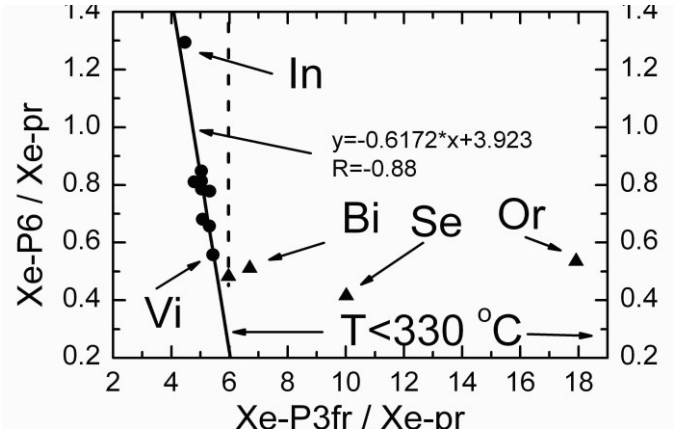

Fig.1. Relative contents of Xe components with Xe-HL (triangles) or Xe-pr (circles)

Fig.2 Relation of Xe components in nanodiamonds of different meteorites.

If the Xe-pr content in the diamond of the most metamorphosed Allende and Indarch does not exceed 15% of all xenon, then the Xe-HL content is at least 65%. The low content of the Xe-pr component corresponds to the conclusion in the work (Lewis et al, 2018) about the extremely low content in the Allende meteorite of a population of nanodiamond grains formed after a Type II supernova explosion and most likely is a phase carrier of the anomalous xenon. Thus, populations of grains with Xe-P3fr and Xe-P6 constitute the main part of diamond grains containing noble gases if the Xe-pr component is present. The components Xe-P3fr and Xe-P6, as noted above, are almost isotopically normal.

The sharp changes in the relative contents of xenon components in diamonds of the first meteorite group are probably due to the presence of noble gas components with low thermal stability in the initial / primary nanodiamond. For xenon, by this component is the low-temperature component Xe-P3 (Huss, Lewis 1994a). According to the data in Fig. 1, this component is almost completely removed from the nanodiamond during thermal metamorphism up to 330 °C.

Alterations of the xenon component ratios in meteorite diamonds are shown in Fig. 2. According to this figure, the following features of these alteration can be noted. The Xe-P3fr / Xe-pr and Xe-P6 / Xe-pr ratios first decrease and then slightly increase with an increase of the temperature of metamorphism to 330 ° C. Consequently, up to this temperature of metamorphism mainly low-temperature xenon Xe-P3 and Xe-P6 components from diamonds were removed.

Perhaps these loses occurred without significant destruction of the diamond grains. The Xe-P3fr / Xe-pr ratio continues to decrease with an increase in the temperature of metamorphism above 330 ° C, but to a lesser extent, while the Xe-P6 / Xe-pr ratio sharply increases. These differences can be interpreted assuming that different components of noble gases are contained in different populations of diamond grains with different thermal-oxidative stability. Probably, the preservation of xenon components is in series Xe-P3fr <Xe-pr << Xe-P6 during thermal metamorphism. Therefore, the destruction of the grains of populations to varying degrees led to the observed alteration in the xenon components.

Conclusion The results of the calculated contents of alternative xenon components (Xe-P3fr, Xe-pr, and Xe-P6) in diamonds of meteorites of thirteen various chemical classes and petrological types at using Xe-pr instead of Xe-HL showed the following. 1. The main xenon components in meteorite nanodiamonds are Xe-P3fr and Xe-P6, the xenon of which is almost normal in isotopic composition. It is assumed that the mass of populations of grains of nanodiamonds with noble gases of the components P3fr and P6 will also be the bulk of grains of nanodiamonds with noble gases, if the concentrations of xenon atoms in the grains of nanodiamonds are the same for all its components. 2. The relative content of the Xe-pr component in the nanodiamond of thermally metamorphosed meteorites does not

exceed 15% of the total xenon content in the diamond of this meteorite. This value is significantly less than that for Xe-HL — at least 65% according to the data in (Huss and Lewis, 1994b). 3. Xenon components are in the series Xe-P3 <Xe-pr << Xe-P6 in terms of increasing the degree of preservation under thermal metamorphism. This indicates the xenon components are content in individual populations of diamond grains with different thermo-oxidative stability .

Thus, the use of Xe-pr led to alteration in the contents of xenon components and their distributions in diamond of various meteorites.

References

Fisenko A. V., Semjonova L. F.(2020). Meteoritic Nanodiamonds: Alternative Composition of Xenon Components // *Solar System Research*, **54**, 3, 253–262. ISSN 0038-0946.

Huss G.R. and Lewis R.S. (1994a) Noble gases in presolar diamonds I: Three distinct component and their implication for diamond origins // *Meteoritics*, **29**, 791–810.

Huss G.R and Lewis R.S. (1994b) Noble gases in presolar diamonds II: component abundances reflect thermal processing, // *Meteoritics,* **29**, 811–829.

Huss G.R., Ott U., and Koscheev A.P. (2008) Noble gases in presolar diamonds III: implantation experiments with synthetic nanodiamonds, *Meteoritics &Planetary Science,* **43**, 1811–1826.

Lewis R.S., Amari S.A., and Anders E. (1994) Interstellar grains in meteorites. II. SiC and its noble gases // *Geochim. Cosmochim. Acta*, **58**, 471–494.

Lewis J.B, Floss C., Isheim D., Daulton T.L., Seidman D.N., and Ogliore R. (2019) Origins of meteoritic nanodiamonds investigated by coordinated atom-prob tomography and transmission electron microscopy studies //*Meteoritics & Planetary Science*, https://doi.org/10.1111/maps.13373

Ivanov A.A., Sevastyanov V.S., Shnykin B.A., Dolgonosov A.A., Krivenko A.P., Priymak S.V., Galimov E.M. Evaluation of the various energy sources effectiveness at the stage of prebiological structures formation during abiogenesis. UDC 550.47

Vernadsky Institute of Geochemistry and Analytical Chemistry RAS, Moscow (aiva@geokhi.ru)

Abstract. Any transformation of organic matter has its own energy format, which makes possible synthesis, destruction or formation of a structure, requires individual sources of energy for each process.
In theoretical and experimental modeling of abiogenesis processes, classically considered energy sources, such as atmospheric electric discharges, radioactive and cosmic radiation, meteorite and comet impacts, volcanic eruptions and other thermal sources, are more suitable for the primary synthesis of low molecular weight organic compounds. However, for the stage of the subsequent formation of prebiological structures, these energy sources are ineffective. The reason for this conclusion is the irregularity and non-specific impact of these energy sources, their insufficiently short duration, energy redundancy, or energy insufficiency. Besides, the formation of prebiological structures and protobionts from them requires a special landscape of the place and soft energy supply for this process over a geologically long period; also, these structures must be protected from the destructive influence of the said energy sources.
All these requirements are met by an unaccounted and not previously considered source of energy and the place of probable formation of prebiological structures, from which, under the given conditions, protobionts could form. Such a place could be abrasive shores, in the caverns of which a pneumatic shock occurred during the surf due to the regular pumping of the multiphase bubbly medium full of energy generated from compounds of the organic broth.

Keywords: pneumatic *impact, protobionts, abiogenesis, peptides, microspheres, multiphase bubble medium, caverns of abrasive shores.*

The analysis of results of experimental and theoretical researches regarding the problem of abiogenic autogenesis in modern and previous studies has shown that none of the classically considered power sources of the nature is enough for this multistage process, as none of them is suitable for a regular power supply of the last stage of structural protobiont formation. Possibly, a power source of another origin is required for this purpose. Such a power source has to meet all requirements which will allow to create cellular structures from the components synthesized in the previous stages of abiogenesis with the assistance of those classically considered power sources, such as atmospheric electric discharges, volcanic eruptions and other thermal sources, comet and meteorite impacts, radioactive and cosmic radiation, including solar ultraviolet. Besides, such a power source also has to be universally suitable to initiate the synthesis of different classes of organic polymers of which all living matter consists, such as lipids, carbohydrates, peptides, nucleic acids, from simple "building blocks" of life (amino acids, nucleotides, sugars, fatty acids).

As each process requires its own format of driving force energy, the search for a universal power source, suitable both for formation of prebiological structures from organic polymer, and for the process of subsequent self-organization of the first predecessors of life, protobionts, out of them, became one of the main lines of our researches.

At the time when the young Earth was nothing but a big chemical reactor made of elementary gases, such as CO_2, CO, CH_4, H_2, H_2S NH_3 and other chemicals, the molecular synthesis, including that of organic compounds, which are the prerequisite predecessors of life, was occurring. However, such situation was suitable mainly for the stage of

synthesis of low molecular weight organic compounds, and a lot was still to happen before the emergence of life. It was the time of primary synthesis of the compounds such as formaldehyde (NSON), acetaldehyde (H_4C_2O), hydrogen cyanide (HCN), cyanoacetylene (HC_3N), urea (H_4CN_2O), acetic ($H_4C_2O_2$), formic (H_2CO_2), oxalic ($H_2C_2O_4$) acids and other low molecular weight organic compounds commonly characterized by pungent odor (Oparin, 1957). It is difficult to imagine the life emerging in such situation! Still, later, under certain conditions, on the basis of these compounds, more complex organic substances, including the first biological building blocks constituting life, e.g. amino acids, nucleotides, fatty acids, and saccharites could be formed. Only then, the majority of these compounds could participate directly in future biological processes (Galimov, 2001). Apparently, it was a high time for the first rudiments of life to appear! However, as we know today, similar organic compounds exist not only on Earth, but also in space, which does not make Earthly conditions of that time exclusive for their synthesis (Kwok, 2018; López-Sepulcre, 2019; Rubin, 2019; Sharma, 2019). This means that the singularity of the planet conditions is explained by something different, which has specifically affected the further course of the events which subsequently have completely changed its shape, having made Earth a currently unique object of the Universe. When and how did these special conditions on Earth conducive to the emergence of a required power source, which marked the qualitative transition from the quantitative variety of organic substances to the first biologically significant structures made of them, appear?!

Could life arise and develop on early Earth abiogenically, in the conditions of oxygenless atmosphere, with the strong cosmic radiation?! It possibly could, but neither in small and open water bodies, nor in hot springs of hydrotherms, nor in volcano calderas, as it is commonly perceived today, but in the bays of caverns of the abrasive coast of the primary ocean shielded from the powerful cosmic radiation by rocky material. On such a shadow stage, energy could be regularly delivered by waves. The energy from the ground swell in partially closed cavities of the bays, containing an insignificant amount of the so-called primordial broth, excited a pneumatic impact, which generated a short-term leap of their pressure and temperatures. Thus, the pneumatic impact arising with regular frequency in the bays of abrasive coast influenced by ground swell would organize a kind of separately isolated thermobarocycler in each of them. That is, ground swell in myriads of vugs, working regularly as a piston, systematically squeezed and warmed air in each single bay, while aerating and carbonating the organic broth inside with bubbles hot from pneumatic impact. Depending on the wave impact force, as well as on the size and arrangement of bays, the instant temperature of the air compressed therein could rapidly increase by hundreds of degrees, and pressure could rise up to 10 atmospheres and higher (Ivanov, 2018). Therefore, on the spherical border of the bubbles hot from shock compression, peptides contained in the organic broth coagulated from it, forming the microspheres absolutely necessary to start protobiont formation. At the next wave impact, the microspheres, attacked by hot bubbles, broke into pieces and combined, changing their sizes and forms. Further, on the polypeptide cover of microspheres existing in the active multiphase bubble environment of cavern bays, both from inside and outside, there could form the structures and compounds necessary to start metabolism. It was promoted not only by the pneumatic impact, but also by the solar photodissociate formed in mineralized water and ionized atmosphere injected continuously into the bay zone. As we see it, the long structural and chemical transformation of polypeptide microspheres resulted in emergence of cell-like structures. Regular pulsation of pressure and temperatures in cell cavities initiated primary metabolism in these cell-like structures, in fact, gradually turning them into primitive protobionts. It is obvious that the beginning of formation of polypeptide membranes of microspheres was the key moment of transition from the simple synthesis of organic compounds to the structural formation of the first probiotic cells. This is a very important point, as life begins with a cell, and a cell begins with the membrane organizing the internal space of a cell for all its future contents. Still, the main thing is that the thermobarocyclic mode of pulsation of the multiphase bubble environment arising in a plethora of cavities of abrasive coasts and actively supported throughout a geologically long period is a natural process capable of initiating the regular formation of high molecular weight organic compounds, generate polypeptide microspheres and other prebiological structures, forcing their metabolism! No natural process known today is capable to provide such format of energy and conditions for the structural stage of abiogenesis on the early Earth!

The power source generated by ground swell, as we suggest, never leaves the multiphase bubble environment alone, pumps it up with the energy of pneumatic impact, maintaining its continuous movement in the caverns.

For the stage of abiogenous structurization of protobionts, the efficiency of the suggested power source, in comparison with the classical power sources considered earlier, is much higher. It is evidenced by the results of experimental modeling of the processes of formation of organic polymers and polypeptide microspheres at pneumatic impact,

which are reflected in our papers numerically and visually (Ivanov, 2019), and set out in this year's paper (Ivanov, 2020) more specifically. To sum up, it is required to list the comparative advantages of the idea of this approach in relation to the sources of the "rigid" energy, such as electric discharges of lightning, energy of the volcanic, hydrothermal, or cosmic nature, the effect of which leads not to the formation of hollow polypeptide microspheres at the structure-forming stage of abiogenesis, but to the formation of drops of diverse liquids (coacervates) or microspherical conglomerates formed on hot volcanic particles.

1. Unlike shallow water bodies or the primary ocean, in the cavities of its abrasive coast the concentration of high molecular weight organic substances can be higher multiple times, and this is the most essential advantage! (By the way, even today the amount of the biomass in the open ocean is much more scarce as compared to its foreshore.)

2. The high efficiency of microsphere formation, since the abrasive coastline of the primary ocean mottled by cavities, due to the regular work of the ground swell, could generate an enormous quantity of them every minute.

3. Initially hollow microspheres of different volume with electroneutral membrane made of coagulated peptides had the wide range of pore sizes capable of passing the building components required to form the structures of the internal cell compartment.

4. The power source is cyclic, short-term, focused and soft, since the energy of pneumatic impact acquired from the ground swell is transferred to the air bubbles aerating the primary broth of caverns.

5. The high frequency of pneumatic blow cycles, and therefore the speed of formation of organic polymers and the structural components of protobionts formed therefrom.

6. The immunity of prebiological structures and protobionts to the harmful action of ultraviolet and other adverse physical factors.

7. The ability of a power source to work round the clock, continuously, day and night.

8. The mode of heating and cooling cycles at increased and decreased pressure.

9. With each wave, organic and inorganic compounds, as well as their radicals, formed on the edge of caverns under the influence of the UV radiation of the Sun, are instantly injected into the reactor zone of cells where, at the pneumatic impact, they are transformed further.

10. The activity of a multiphase water and bubble environment of the reactor zone of a cavern cell can be maintained throughout a geologically long period.

References

Galimov E.M. Phenomenon of Life. URSS. 2001, p. 256

Ivanov A.A. The shadow side of abiogenesis, p. 70, Ikar, Moscow 2020

Oparin A.I. The origin of life on the Earth. ASUSSR, Moscow, 1957, p. 457

Ivanov A.A., Sevastyanov V.S., Voropaev S.A., Dolgonosov A.A. Microscale processes of thermal coagulation of polypeptides during pneumatic impact. Goldschmidt2018, August 12-17, Boston, USA

Ivanov A.A., Sevastyanov V.S., Shnykin B.A., Dolgonosov A.A., Krivenko A.P., Priymak S.V., Roslyakova A.S., Galimov E.M. Self-organization of prebiological environment in the conditions of early Earth. Experiment in Geosciences 2019 Volume 25 N 1

Sun Kwok. Formation and delivery of complex organic molecules to the Solar System and early Earth Vancouver, Canada, 2018, Handbook of Astrobiology, Vera Kolb (ed.), CRC Press, p.165.

Ana López-Sepulcre, Nadia Balucani, Cecilia Ceccarelli, Claudio Codella, Francois Dulieu, Patrice Theulé, Interstellar formamide (NH2CHO), a key prebiotic precursor, ACS Earth and Space Chemistry, 2019, 3 (10), 2122-2137

Mohit K. Sharma, Transfer of radiation in the formic acid: A precursor for amino acids, J. Astrophys. Astr. (2019) 40:10

Martin Rubin*, David V. Bekaert, Michael W. Broadley, Maria N. Drozdovskaya, and Susanne F. Wampfler, Volatile species in comet 67P/Churyumov-Gerasimenko – investigating the link from the ISM to the terrestrial planets, ACS Earth Space Chem. 2019, 3, 9, 1792–1811.

Kuyunko N.S., Alexeev V.A. Thermoluminescent reseach and determination of metamorphism degree of carbonaceous CO and CV group chondrites.

Vernadsky Institute of Geochemistry and Analytical Chemistry RAS, Moscow (AVAL37@mail.ru)

Abstract. The results of thermoluminescent studies of 11 samples of carbonaceous CO and CV group chondrites from the meteorites collection of the Geochemistry Institute of the Russian Academy of Sciences are presented. The measurements of natural and x-ray radiation induced in laboratory condition thermoluminescence were made relative to Dhajala H3.8 chondrite. The temperature maximums of thermoluminescent glow for the researched meteorites were determined. The intensity of the natural and x-ray radiation induced in laboratory condition thermoluminescence were calculated by the area under the luminescence curve. The emission curves of the x-ray radiation induced thermoluminescence of carbonaceous chondrites have a complex shape with a peak in the temperature range 100-130 °C. In some samples, less pronounced peaks are recorded at temperatures above 150 °C.

It was found that the thermoluminescence intensity calculated from the area under the glow curve and the height of the low-temperature peak (1p00-130 °C) correlate with the metamorphism degree of carbonaceous

chondrites. The calculated subtypes are in good agreement with the data of other researchers.

Keywords: thermoluminescence, meteorites, carbonaceous chondrites, meteorite metamorphism.

The thermoluminescent method is one of the simplest and most reliable methods for recording structural changes in a substance. It is widely used for meteorite research - orbit estimation, shock-thermal history, identification of finds, etc.

In order to expand the database of thermoluminescence (TL) of meteorites, in this work, we measured the natural (TLnat) and x-ray radiation induced in laboratory condition thermoluminescence (TLind) of 11 samples of carbonaceous CO and CV group chondrites. For research, gross samples of meteorites weighing 0.7-1.0 g were crushed and crushed in a jasper mortar under a layer of ethyl alcohol. The magnetic fraction was separated with a hand magnet after drying for 24 hours in air. Three samples weighing 2 mg were prepared from the nonmagnetic fraction of each test sample by quartization method. Each sample was placed in a 6 mm diameter beryllium foil dish and evenly distributed on the bottom with an acetone drop under the binocular. The solvent was removed by air-drying for 24 hours. Thermoluminescence was recorded on a modified laboratory unit. The interface made on the basis of the L-154 board made it possible to register the photomultiplier current and the sample heating temperature on a computer. The resolution of the registration was 1 ° C.

The results of thermoluminescent studies of carbonaceous chondrites are presented in figures 1-3 and in the table.

The emission curves of the X-ray radiation induced thermoluminescence of carbonaceous chondrites have a complex shape with a peak in the temperature range 100-130 °C. In some samples, less pronounced peaks are recorded at temperatures above 150 °C. The calculations of the thermoluminescence parameters were carried out according to the obtained TL spectra of the glow (table). An average of three measurements was used. The natural and x-ray radiation induced in laboratory condition thermoluminescence intensity values were calculated by the area under the luminescence curve in the temperature range of 50-350 ° C in relative units by normalizing to the corresponding values for Dhajala H3.8 chondrites.

Based on model experiments (Ivliev et al., 1995, 1996, 2002) on the study of thermoluminescence in oligoclase, calcite and quartz subjected to shock loading by spherical converging waves, a high sensitivity of TL characteristics to radiation from an external radioactive source is shown. It was also concluded that variations of radiation induced TL are due to changes in the crystal structure of feldspar as a result of shock-thermal metamorphism.

In a study (Sears et al., 1980), metamorphic sequence was found for TL data for nonequilibrium ordinary chondrites. We (Kuyunko et al., 2015) measured X-ray radiation induced thermoluminescence under laboratory conditions for more than 50 ordinary nonequilibrium chondrites and established the correlation dependence of TLind with a petrological subtype in the range 3.0-3.9 and used it to classify meteorite finds. Thermoluminescent studies (Sears, 1991, Guimon, 1995) showed a metamorphic sequence for carbonaceous chondrites similar to nonequilibrium ordinary chondrites, despite the difference in the ratio of elements and oxygen isotopic composition. It was shown that according to the intensity of luminescence in the low-temperature peak of TL (up to 130 °C) in carbonaceous CO and CV group chondrites, one can distinguish 10 subtypes 3.0-3.9 similar to ordinary nonequilibrium chondrites, reflecting the degree and nature of the metamorphism of their parent bodies. The relationship between the height of the low-temperature peak and the intensity of x-ray radiation induced in the laboratory thermoluminescence with the petrological subtype of the studied carbonaceous chondrites is shown on Fig. 3.

Table. 1. The results of thermoluminescent studies of carbonaceous CV and CO group chondrites

Meteorite	Symbol	Type	Subtype	Tmax,°C	TLind	Peak height	Dhajala's Peak height	Height relative to Dhajala
Felix	Fe	CO	3,4	106	0,0856	0,380	3,596	0,106
Isna	Is	CO	3,7	108	0,2056	1,288	3,596	0,358
Kainsaz	Ka	CO	3,2	105	0,1372	0,673	3,202	0,210
Lance	La	CO	3,4	106	0,1538	0,723	3,596	0,201
Ornans	Or	CO	3,4	107	0,0556	0,271	3,990	0,068
Warrenton	Wa	CO	3,6	106	0,1815	1,234	3,596	0,343
Allende	Al	CV	3,2	105	0,0561	0,427	3,202	0,133
Axtell	Ax	CV	3,0	113	0,0053	0,031	3,990	0,008
Efremovka	Ef	CV	3,2	108	0,0983	0,280	3,202	0,088
Grosnaja	Gr	CV	3,2	107	0,0149	0,062	3,202	0,019
Leoville	Le	CV	3,3	192	0,0866	0,257	3,202	0,080

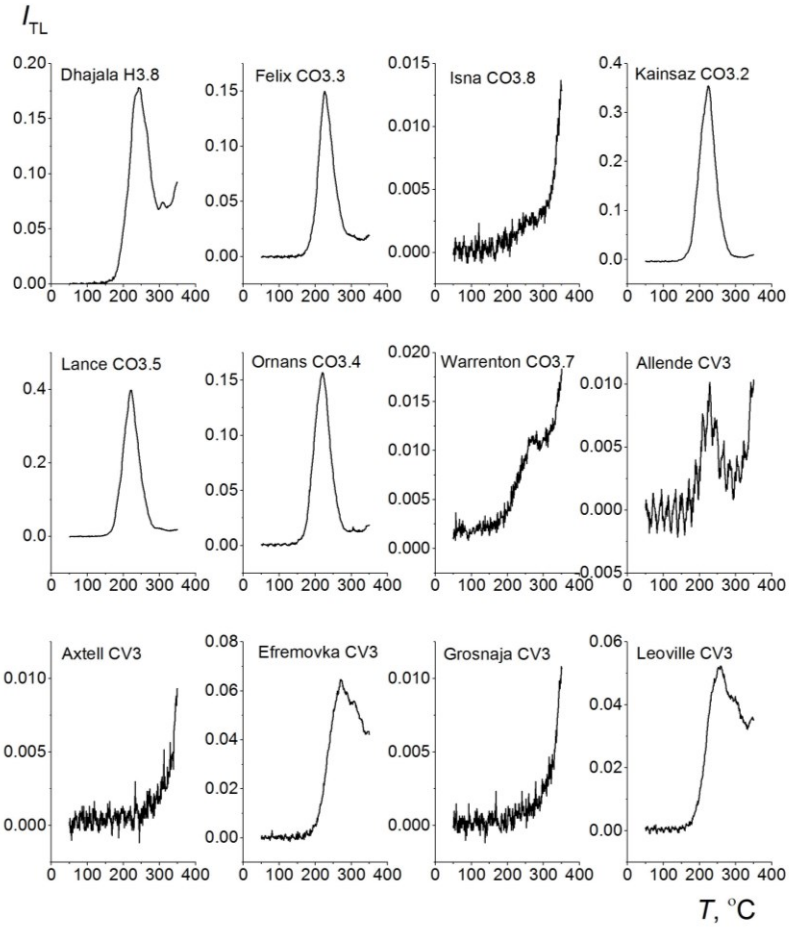

Fig. 1. Spectra of natural thermoluminescence of carbonaceous CV and CO group chondrites

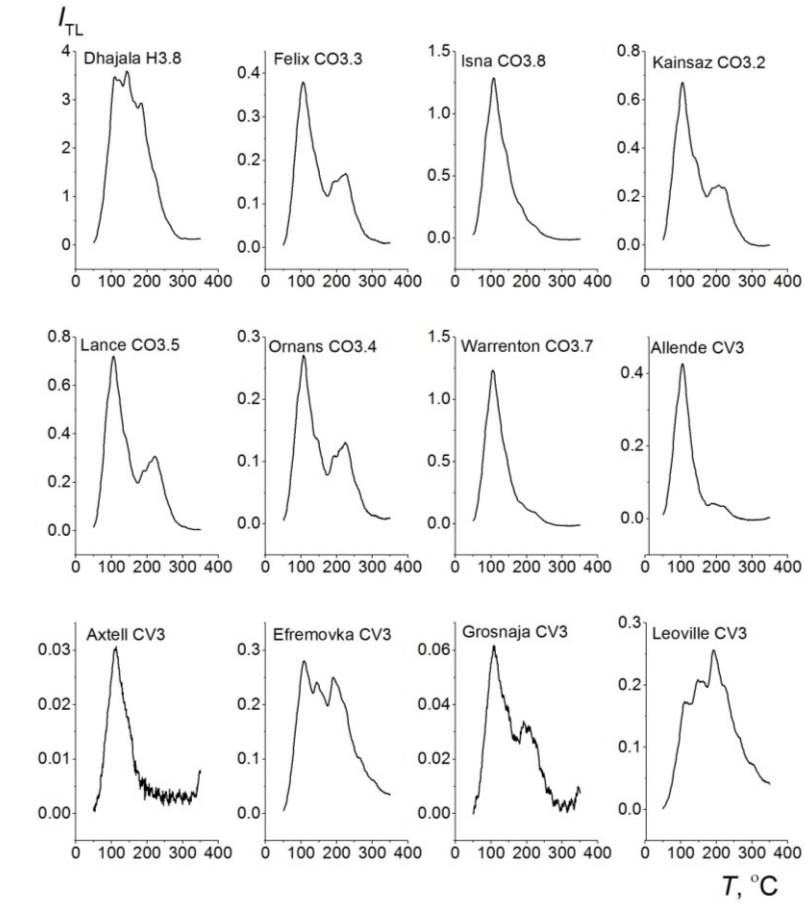

Fig. 2. X-ray-induced thermoluminescence spectra of carbonaceous CV and CO group chondrites

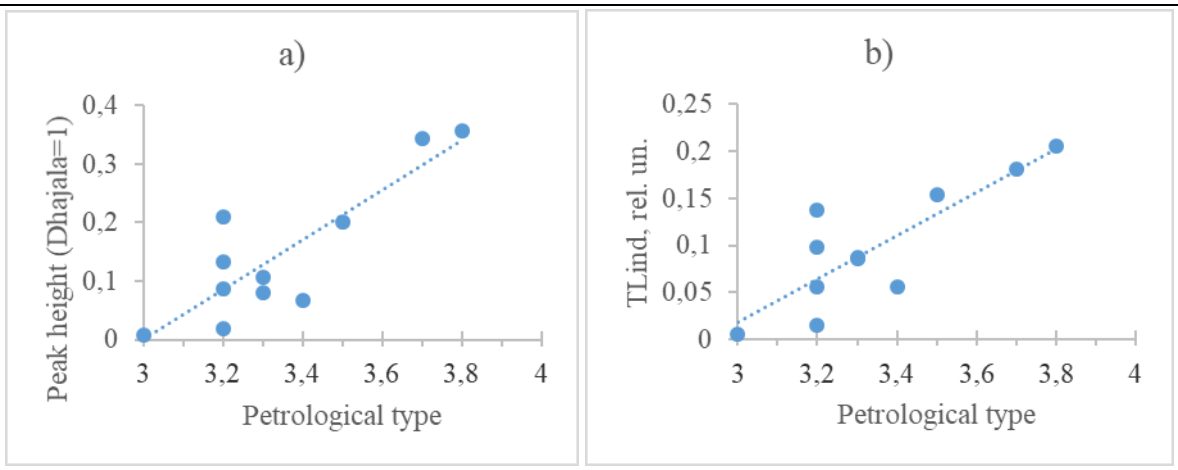

Fig. 3. Dependence of peak height (a) and TLind (b) on the petrological type of carbonaceous CV and CO group chondrites relative to the Dhajala H3.8 chondrite

Conclusions. Measurements of X-ray radiation induced thermoluminescence in laboratory conditions can be used to assess the nature and metamorphism degree of the parent bodies of carbonaceous CO and CV group chondrites.

This work was partially supported by Program No. 12 of the Presidium of the Russian Academy of Sciences

References

Ivliev A.I., Badyukov D.D., Kashkarov L.L. (1995) Investigations of thermoluminescence in samples subjected to experimental shock loading. I: Oligoclase. // Geochemistry. No. 9. S. 1368-1377.

Ivliev A.I., Badyukov D.D., Kashkarov L.L. (1996) Thermoluminescence studies in samples subjected to experimental shock loading. II: Quartz. // Geochemistry. No. 10. S. 1011-1018.

Ivliev A.I., Badyukov D.D., Kuyunko N.S., Kozlov E.A. (2002) Thermoluminescence studies in samples subjected to experimental shock loading. III: Calcite. // Geochemistry. No. 8. S. 820-833.

Kuyunko N.S., Ivliev A.I., Alekseev V.A. (2015) Determining the degree of metamorphism of ordinary nonequilibrium chondrites by the thermoluminescent method. // Proceedings of the All-Russian Annual Seminar on Experimental Mineralogy, Petrology and Geochemistry. Moscow, April 21-22, 2015. Moscow.: GEOCHI RAS, 2015.1, 293-296.

Guimon R.K., Symes S.I., Derek W.G. et al. (1995) Chemical and physical studies of type 3 chondrites XII: The metamorphic history of CV chondrites and their components. // Meteoritics. V.30. N6. P.704-714.

Sears D.W.G., Grossman J.N., Melcher C. L., et al. (1980) Measuring metamorphic history of unequilibrated ordinary chondrites. // Nature, 287 (5785), 791-795.

Sears D.W.G., Batchelor J.D., Lu J., Keck B.D. (1991) Metamorphism of CO and CO-like chondrites and comparison with type 3 ordinary chondrites. // Proc. NIPR Symp. Antarct. Meteorites, 4, 319-343.

Lavrentjeva Z.A., Lyul A.Yu. To question about formation of the pallasite parent bodies: on the peculiarities of trace element composition of mineral components from the omolon pallasite.

V.I. Vernadsky Institute RAS, Moscow (lavza@mail.ru).

Abstract. In the present paper the results of trace element abundances in the accessory minerals and fragments from the Omolon pallasite are reported. Based on the study of the features of lithophile and siderophile trace element distributions, it is assumed that Omolon pallasite body was formed as impact-brecciated mixture of material in the result of the large impacts between asteroids.

Keywords: mineral fractions; trace element distributions; pallasites.

Pallasites are highly differentiated meteorites with two major phases, olivine and Fe-Ni metal [Buseck, 1977]. Based on the chemical composition of metal and silicates pallasites are subdivided into main, main anomalous, Eagle Station, and pyroxene bearing groups [Wasson and Choi, 2003]. The main group of pallasites, which was supposedly produced from a single parent body, could be formed: (1) in the near surface areas of the body [Mittlefehldt , 1980; Davis. and Olsen,1991]; (2) near the core of the body [Davis and Olsen,1991; Wahl, 1965]; (3) in the metal–olivine contact zones of isolated metallic lenses [Urey, 1956], or (4) at the core–mantle boundary [Wasson and Choi, 2003; Scott, 1977]. The origin of pallasites is also controversial. A standard view is that pallasites originated from the core – mantle boundary in differentiated bodies [Scott, 1977; Wasson and Choi, 2003]. At the same time, pallasites could be formed not at the core–mantle boundary (most abundant opinion), but as impact–brecciated mixture of the core–mantle material. A

mixing of small amounts of metal from the core with mantle olivine could be caused by catastrophic collisions between asteroids [Asphaug et al., 2006]. Such collisions could transform colliding objects into a series of differentiated bodies with diverse metal–silicate ratios.

This work reports new data on the composition of mineral fractions of the Omolon pallasite, which are considered from the viewpoint of cosmochemical history of pallasites. The preliminary study of olivine crystals shows that the meteorite Omolon belongs to main group of pallasites with low concentration of fajalite about 12.3 % [Bondar et al., 2002]. The Omolon pallasite experienced two impact deformations, which follows from data on the chemical composition of opaque minerals and petrography of this meteorite [Sharygin et al., 2006]. The main aim of our study is to estimate better the petrogenesis of pallasites from studying the trace element distribution in individual mineral.

Samples and methods. We studied the following fractions of minerals: tridymite (SiO_2), troilite (FeS), daubreelite ($FeCr_2S_4$), metal (Fe,Ni phase), magnetite ($FeFe_2O_4$) and four fragments from the Omolon pallasite, which were hand - picked using needles under MBS- 2 binocular microscope and stereoscopic MPS-2 microscope. Iron–nickel phase was separated by hand magnet and magnetic needle. The elemental composition of fractions was analyzed at the Central Laboratory of GEOKHI RAS using optimized version of neutron–activation analysis developed for analyzing extraterrestrial material [Kolesov, 2001].

Results and discussion. Under consideration are peculiarities of elemental composition of accessory minerals and fragments extracted from Omolon pallasite. The analysis of the chemical composition of the obtained data showed that:

Tridymite in Omolon pallasite (fraction M, Fig. 1) is enriched in REE with the prominent predominance of heavy REE $(Lu/La_M)/(Lu/La)_{C1}$ = 1.97 and positive Eu anomaly $(Eu/Sm)_M/(Eu/Sm)_{C1}$ = 2.37. The element distribution in the tridymite indicates that this mineral accumulates HREE. Tridymite in comparison with the clean olivine (fraction A, Fig. 1.) is strongly enriched in REE, Na, Ca, Sc and in siderophilic elements.

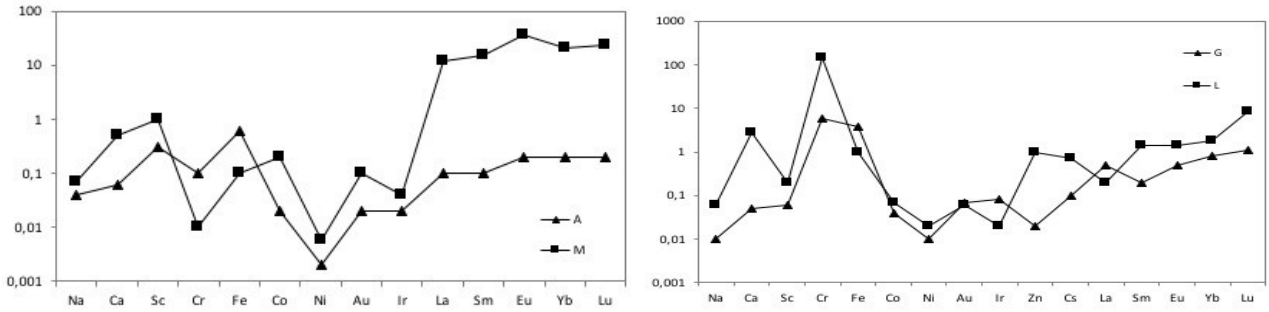

Fig.1. CI chondrite–normalized of trace element abundance patterns in accessory minerals from Omolon pallasite: 1 – fraction A (pure olivine); 2 – fraction M (trydimite).

Fig.2. CI chondrite–normalized of trace element abundance patterns in accessory minerals from Omolon pallasite: 1 – fraction G (troilite); 2 – fraction L (daubreelite).

The presence of tridymite in the olivine grains is uncommon, the phase of silica and forsterite the incompatible minerals, which are not formed in the presence of each other. In pallasite of main group Fukang [Della Giustina et al., 2011], also as in Omolone, is discovered the tridymite, which, as he is presented by the authors of work, was formed after olivine. Tridymite is a SiO_2, polymorph that crystallizes within a narrow range of low-pressure, high temperature conditions. It can stably form at vacuum pressures and temperatures between 867 and 1470°C [Della-Giustina et al., 2011]. It cannot with stand pressures > 0.4 GPa at any temperature, even for short durations. It is therefore as a pressure indicator in terrestrial and planetary materials [Della-Giustina et al., 2019].

Troilite (fraction G, Fig. 2) demonstrates enrichment in Cr, Fe, Ir, and Co relative to Ni (Cr,Fe,Ir, Co/Ni)G/(Cr,Fe,Ir,Co/Ni)CI = 590.0; 301.7; 8.0, and 4.0, respectively. Such a distribution of siderophile elements in the troilite suggests that Cr, Fe, Ir and Co is more chalcophile elements than Ni. Enrichment of troilite in Cr can be related to the presence of daubreelite.

In daubreelite (fraction L, Fig. 2), the abundance of iron and zinc (Fe,Zn)L/(Fe,Zn)C1 = 1.0 and ratio of (Ir/Ni)L/(Ir/Ni)C1= 1.0 correspond to CI chondrites. The abundances of volatile Zn and Na with close condensation temperatures strongly differ $(Zn/Na)_L/(Zn/Na)_{C1}$ = 16.7 due to different geochemical properties. Daubreelite is enriched in Co and Au relative to Ni and Ir. The distribution of siderophile elements in the troilite and daubreelite suggests that these minerals were formed under different conditions (probably, troilite was formed at higher temperature than daubreelite).

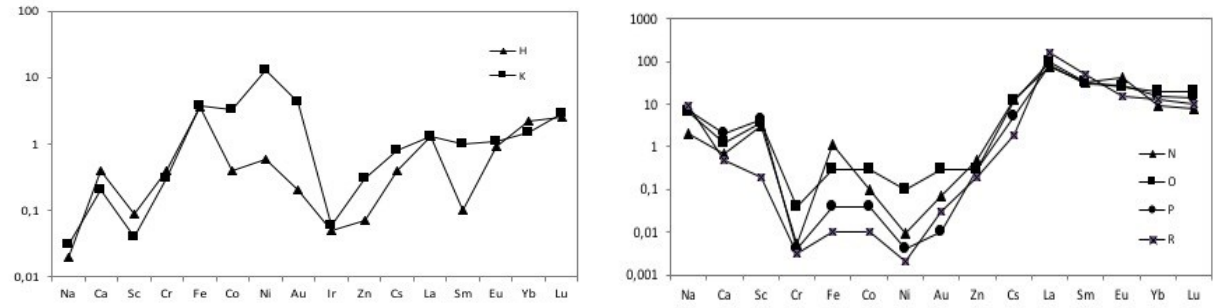

Fig.3. CI chondrite–normalized of trace element abundance patterns in accessory minerals from Omolon pallasite: 1 – fraction H (magnetite); 2 – fraction K (metal).

Fig.4. CI chondrite–normalized of trace element abundance patterns in fragments N, O, P, R from Omolon pallasite.

According to the obtained data, the Co content (0.16 wt %) in the nickelous iron (fraction K, Fig. 3) in the Omolon pallasite is significantly lower than in iron meteorites (0.4 – 0.7 wt %) and enstatite and ordinary chondrites (0.3 – 1.3 wt %) [Scott, 1972]. Nickelous iron from the Omolon pallasite has lower Au content (0.6 μg/g) than E-and H-chondrites, but exceeds the lower limit for iron meteorites. The abundance of Ir, Co, and Au in Fe,Ni - phase in the pallasite relative to Ni and CI chondrite is less than 1 and, hence, lower than cosmic contents.

In magnetite (fraction H, Fig. 4), the abundances of Fe, Co, and Ir relative to Ni are higher than in metal: (Fe,Co,Ir/Ni)H/(Fe,Co,Ir/Ni)C1 = 6.0, 0.7, and 0.08, respectively, while (Au/Ni)H/(Au/Ni)C1 = 0.33 is identical to that in the pallasite metal.

Fragments enriched in refractory lithophile elements. The Omolon pallasite contains four fragments with high contents of refractory lithophile elements (Fig.4). All fragments enriched in LREE, Na, Ca, Sc, Cs.

The fragments N, O, P, and R show significant fractionation between LREE and HREE (La/Lu)N/(La/Lu)C1 = 9.7; (La/Lu)O/(La/Lu)C1 = 5.2; (La/Lu)P/(La/Lu)C1 = 6.6; (La/Lu)R/(La/Lu)C1 = 16.2 with positive anomalies of Eu in the N fragment and negative, in O and R fragments. In the fragments of the Omolon pallasite, the HREE/LREE fractionation increases with increase of Na content in them. Obviously, the LREE, Na, and Th were incorporated in the same mineral. In the pallasites, the carriers of such elements as Na, K, U, and Th are phosphates [Buseck and Holdsworth, 1977]. The Omolon pallasite contains two phosphates [Sharygin et al., 2006]: stanfieldite $Ca_4\ Mg_3\ Fe_2\ (PO_4)_6$ and whitlockite $(Ca\ Mg\ Fe^{2+})_3\ (PO_4)_2$. Whitlockite in this case is of geochemical interest as accumulator of small amounts of alkalis available in pallasites [Buseck and Holdsworth, 1977]. Hence, LREE and Na in the fragments are accumulated in whitlockite.

Conclusion. Based on the study of the features of lithophile and siderophile trace element distributions in the accessory minerals and fragments from Omolon pallasite the assumption has been made that these peculiarities probably result from mixing effects of material of core and mantle olivine from different differentiated parent bodies. Such a mixture could result from a strong impact between asteroids [Asphaug, 2006].

References

Asphaug E., Agnor C.B., Williams Q. Hut – and - run planetary collisions. // Nature. 2006. V.438. P. 155 - 160.

Buseck P.R. Pallasite meteorites- mineralogy, petrology and geochemistry. //Geochim. Cosmochim. Acta. 1977. V.41. № 6. P. 711 - 740.

Buseck P. R. and Holdsworth E. Phosphate minerals in pallasite meteorites. //Mineral. Mag. 1977.V. 41.№ 317. P. 91 - 102.

Bondar Yu. V., Kashkarov L. L., Perelygin V.P. Tracks and dislocations in silicate minerals of the Omolon pallasite.// Lunar Planet. Sci. Conf. 33 th. 2002. Houston: LPI, 2002, CD #1067.

Davis A. M. and Olsen E. J. Phosphates in the pallasite meteorites as probes of mantle processes in small planetary bodies. //Nature 1991.V. 353. P. 637 - 640.

Della-Giustina D. N., Lauretta D. S., Hill D. H., Killgore M., Yang H. and Downs R. T. (2011) Implications of the presence of tridymite in Fukang pallasite. // Lunar Planet. Sci. Conf. 42th. 2011. Houston: LPI 2011. CD # 1915.

Della-Giustina D. N., Habib N., Domanik K.J., Lauretta D. S., Hill D. H., Lauretta D. S., Goreva Y. S., Killgore M., Hexiong Y. and Downs R. T. The Fukang pallasite: characterization and implications for the history of the main-group parent body. // Meteoritics & Planetary Science 2019.V.54. Nr 8. 1781 - 1807.

Kolesov G. M., Shubina N.V., Lyul A.Yu. Optimizing instrumental neutron activation analysis of extraterrestrial materials: fragments of lunar rocks, meteorites, chondrules and ultrarefractory inclusions. // J. Anal. Chem. - 2001. - V.56. - P. 1169 – 1172.

Mittlefehldt D.W. The composition of mesosiderite olivine clasts and implications for the origin of pallasites. //Earth Planet. Sci. Lett. 1980 V.51. № 1. P. 29 - 40.

Scott E.R.D. Chemical fractionation in iron meteorites and its interpretation. //Geochim. Cosmochim.Acta. 1972.V.36. №11. P. 1205 - 1236.

Scott E. R. D Geochemical relationships between some pallasites and iron meteorites. //Mineral. Mag. 1977. V. 41. № 318. P. 265 - 272.

Sharygin V.V., Kovyasin S.V., Podgornykh N.M. Mineralogy of olivine hosted inclusions from the Omolon pallasite. // Lunar Planet. Sci. Conf. 37th 2006. Houston: LPI, 2006, CD #1235.

Urey H. C. Diamonds, meteorites, and the origin the solar system. //Astrophys. J. 1956. V. 124. P. 623 - 637

Wahl W. The pallasite problem. (1965). //Geochim. Cosmochim.Acta. Vol. 29. № *3*. P.177 – 181

Wasson J. T. and Choi B. G. Main–group pallasites: chemical composition, relationship to III AB irons, and origin. //Geochim. Cosmochim. Acta. 2003.V. 67. № 16. P. 3079 - 3096.

Lyul A.Yu., Lavrentjeva Z.A. On an influence of the metamorphic processes on siderophile element distributions between the major componemts of the h-group of ordinary chondrites.

V.I. Vernadsky Institute RAS, Moscow (*ajull@mail.ru*)

Abstract. Analysis of the siderophile element contents in the metal and silicate fine-grained fraction of the H-group ordinary chondrites shows that the secondary processes in the parent body did not lead to a noticeable redistribution of elements between major chondritic components.

Keywords: ordinary chondrites, H-group, major components, siderophile elements, parent body, secondary processes.

The elemental composition of the individual components of chondrites reflects both the cosmochemical fractionation of elements during the formation of the substance of chondrites in the protoplanetary cloud, and the subsequent geological processes that took place in their parent bodies. Despite the fact that the abundances of rock-forming elements in chondrites are similar to those of the solar photosphere, the observed significant differences in the composition of individual components of the chondrites of the groups are due to subsequent post-accretion changes in their primary composition in the parent bodies under the influence of secondary thermal and water processes. Studying the properties of ordinary chondrites, the most numerous group of meteorites, allows you to obtain information about both the primary processes in the early solar system and the secondary processes that took place in the parent bodies of this group of meteorites. The currently observed trends in the fractionation of elements in the substance of chondrites are indicators of condensation and metamorphic processes occurring at different stages of the evolution of the substance of chondrites. Ordinary chondrites are represented by three groups that differ both in the content of iron and siderophile elements in them, and in the distribution of these elements between the main components of meteorites: chondrules with metallic iron and a fine-grained substance filling the space between these fractions of chondrites. To assess the effect of secondary processes in parent bodies on the primary composition of the main components of chondrites, data on the content of siderophilic elements in individual components of ordinary chondrites of the H-group, characterized by a high content of metallic iron, are considered. The data obtained by the INAA method on the content of siderophilic elements in the metal (8 vol. %), fine-grained fractions (10-15 vol.%) and chondrules (60-80 vol.%) [Scott, 2007] are shown in the tables.

Results and its discussion The metallic fraction of chondrite**s** is represented by isolated grains of kamacite + tenite + plessite composition and its chemical composition is determined by the ratio of these components.

Table 1a. The content of siderophile elements in the Fe, Ni-fractions of nonequilibrium chondrites of the H-group (Lavrukhina et al. 1982; Kong et al., 1997; Rambaldi, 1977).

Chondrite	Type	Fe,%	Ni,%	Co,%	Ir, mcg/g	Au, mcg/g
Tieshitz	H3	88	11,1	0,57	3,7	1,3
Dimmitt	H3,4	93	6,0	0,34	2,8	0,92
MAC88174	H3,5	83	13	0,40	3,9	1,71
ALHA77299	H3,7	90	11,6	0,44	3,6	1,54
WIS91627	H3,7	86	8,8	0,41	3,3	1,24
Dhajala	H3,8	89	9,8	0,42	4,0	1,32
EET87778	H3,9	85	9,1	0,43	3,4	1,2
Mean	**H3,4**	**87**	**10,4**	**0,42**	**3,7**	**1,4**
σ		***3***	***1,9***	***0,06***	***0,4***	***0.23***

Table 1b. The content of siderophile elements in the Fe, Ni-fraction of equilibrium chondrites of the H-group (Lavrukhina et al. 1982; Kong et al /. 1997; Rambaldi, 1977).

Chondrite	Type	Fe,%	Ni,%	Co,%	Ir, mcg/g	Au, mcg/g
Ochansk	H4	92	7,9	0,51	3,1	1,1
Y91434	H4	89	9,3	0,46	3,0	1,3
Pultusk	H5	92	7,5	0,47	2,2	1,04
Richardon	H5	89	8,8	0,42	3,1	1,2
Y791328	H5	89	8,0	0,50	3,1	1,2
Pshibram	H5	91	7,1	0,48	1,9	1,18
Y74014	H6	87	10	0,49	3,2	1,31
Doroninsk	H6	90	8,7	0,44	3,0	1,12
Mean	**H4-6**	**89**	**9,1**	**0,49**	**3,2**	**1,25**
σ		***1,5***	***0,9***	***0,02***	***0,2***	***0,08***

As follows from the data table 1a, the content of siderophile elements in nonequilibrium ordinary chondrites does not depend on the degree of individual meteorite metamorphism. Of the

compositional features of nonequilibrium chondrites, significant variations in the nickel content can be noted, possibly due to the ratio of taenite and kamacite in the selected chondrite fraction. Data on the metal composition of equilibrium ordinary chondrites are presented in table 1b.

Similarly to nonequilibrium chondrites, in equilibrium chondrites there is also no clear dependence of the content of siderophile elements in the metal on the degree of metamorphism of chondrites. It is possible that variations in the composition of the metal in ordinary chondrites are due to the ratio of kamasite and tenit in it.

The fine-grained fraction of ordinary chondrites. Composed of silicate minerals, the non-magnetic fine-grained fraction (10 - 15 vol. %), filling the space between chondrules and metal particles, is also the main component of ordinary chondrites of the H-group [Scott, 2007]. In the process of thermal metamorphism, a change in its chemical composition is possible as a result of redistribution of siderophilic elements between other components of chondrites. To assess the influence of metamorphic secondary processes on the chemical composition of the fine-grained fraction of the component chondrites, data on the content of siderophile elements with different distribution coefficients between the metal and the silicate fraction of meteorites are considered.

Table 2a. The content of siderophile elements in the fine-grained fractions of nonequilibrium chondrites of the H-group. (Kong et al., 1997; Rambaldi, 1977).

Chondrite	Type	Fe,%	Ni,%	Co,%	Ir, mcg/g	Au, mcg/g
Grady	H3	17,6	0,296	155	0,13	0,054
MAC88174	H3,5	13,7	0,251	138	0,14	0,04
ALHA77299	H3,7	14,3	0,225	106	0,16	0,028
WIS91627	H3,7	15,1	0,362	185	0,25	0,044
Dhajala	H3,8	17	0,111	110	0,12	0,015
EEt87778	H3,9	13,2	0,324	100	0,33	0,034
Mean	**H3**	**15,1**	**0,261**	**132**	**0,18**	**0,035**
σ		**1,6**	**0,08**	**30**	**0,07**	**0,012**
σ,%		**11**	**31**	**23**	**38**	**34**

Table 2b. The content of siderophile elements in the fine-grained fractions of equilibrium H-group chondrites (Kong et al., 1997; Rambaldi, 1977).

Chondrite	Type	Fe,%	Ni,%	Co, mcg/g	Ir, mcg/g	Au, mcg/g
Ochansk	H4	18,3	0,496	230	0,33	0,055
Y791434	H4	16,2	0,526	185	0,39	0,043
Richardon	H5	15,4	0,821	110	0,71	0,074
Y791323	H5	18,7	0,917	390	0,37	0,064
Y74014	H6	16,1	0,350	160	0,23	0,036
mean		**16,9**	**0,621**	**215**	**0,41**	**0,054**
σ		**1,3**	**0,21**	**95**	**0,18**	**0,014**
σ ,%		**7,6**	**33**	**44**	**25**	**52**

As follows from the data in Table 2 variations in the content of siderophile elements in the fine-grained fraction of nonequilibrium H-chondrites significantly exceed those for the metal of chondrites of this group. These differences are partly due to the different metal content in the selected fractions, but mainly due to the ratio in kamasite and taenite.

A feature of the composition of this fraction of equilibrium chondrites is a significant scatter the content of siderophile elements in it. Moreover, with almost the same iron content in nonequilibrium and equilibrium chondrites in this group, significant differences are observed in the contents of other siderophiles, especially Ni, Ir and Au - elements concentrated mainly in taenite.

From the above table 3 data shows that the value of the distribution coefficients of iron and cobalt between the metal and the silicate fine-grained fraction does not depend on the petrological type of chondrites. We can also note a significant difference in the distribution coefficients between individual fractions of elements with strong siderophilic properties (Au and Ir). In the transition from nonequilibrium chondrites to equilibrium, the magnitude of these coefficients decreases markedly. The relatively high content of siderophile elements in the nonmagnetic fraction of H-chondrites and the observed differences in the distribution coefficients between the metal and the fine-grained fraction of chondrites are possibly due to the presence of submicron grains of metal formed in other redox conditions, the composition of which is different from the composition of basic Fe, Ni phases of chondrites [Horan et al.].

Table 3. Coefficients (K) of distribution of siderophilic elements (K) between metal and fine-grained fractions of ordinary H-group chondrites of different petrological types. (Data of Tables 1 and 2).

Fractions	Type	K	б	б, %
Fe (metal) /Fe (fine-grained fraction).	H3	5,9	0,44	7,5
	H4-6	5,4	063	6,1
Ni (metal) /Ni (fine-grained fraction).	H3	41	23	56
	H4-6	52	17	33
Co (metal) /Co (fine-grained fraction)	H3	33	7,8	23
	H4-6	35	9,4	27
Ir (metal) / Ir (fine-grained fraction)	H3	18	8,5	45
	H4-6	8,4	3,6	43
Au (metal) / Au (fine-grained fraction.)	H3	44	23	53
	H4-6	24	15	63

Conclusion. An analysis of data on the content of siderophile elements in the metal and the fine-grained fractions of H-group chondrites of different petrological types showed that metamorphic processes did not significantly affect the content of siderophile elements in these fractions of chondrites. The observed differences in the content of this group are primary, due to the processes occurring in the parent body of chondritis.

References

Chou C.L., Baedecker P.A., Wasson J.T. (1973). Distribution of Ni, Ga, Ge and Ir between metal and silicate portions of H-group chondrites. // Geochim. Cosmochim. Acta. V.37. P. 2150-2171.

Horan M.F., C.M.O'D Alexander, Walker R.J. (2009). Highly siderophile element evidence for early solar system processes in components from ordinary chondrites. // Geochim. Cosmochim. Acta. V.73. P. 6954-6957.

Kong P., Ebihara M. (1997). The origin and nebular history of the metal phase of ordinary chondrites. // Geochim. Cosmochim. Acta. V.61. P. 2317-2329.

Lavrukhina A.K., Lyul A.Yu., Baryshnikova G.V. (1982). On the distribution of siderophilic elements in the Fe, Ni-phase of ordinary and enstatite chondrites. // Geochemistry. No. 5. S. 645-663.

Lyul A.Yu., Lavrentieva Z.A. (2018). On the fractionation of siderophile elements in the fine-grained fraction of ordinary chondrites of different chemical groups (2018). // Materials of the 18th international conference "Physico-chemical and petrographic studies in earth sciences. Moscow. S. 168-171.

Rambaldi E.R., Cendales M., Thacker R. (1978). Trace element distribution between magnetic and non-magnetic portions of ordinary chondrites. // Earth Planet. Sci. Lett. V.40. P. 175-168.

Scott E.R.D. (2007). Chondrites and Protoplanetary disk. // Ann. Rev. Earth Planet. Sci. V.35. P. 577-620.

Nikitin S.M,[1], Gorbatsevich F.F.[2] , Skripnik A.Ya.[3], Beltyukov N.A.[4], Morozov I.A.[4] Brittle fracture features of terrestrial analogues of ordinary chondrites components under volumetric compression

[1] LP LLC "LS-KAM", Moskow, [2]GI KSC RAS, Apatiti, [3]GEOKHI RAS, Moscow, [4]GI UB RAS, Perm. (petromechanika69@mail.ru),

Abstract. The article discusses terrestrial rocks, which are analogues of the mineralogical and geochemical structural elements that determine the conditions of deformation and destruction of stone meteorites. The selection of rocks was carried out on the basis of the manifestations of signs of mechanical shock in the structure and composition of the substance of ordinary chondrites. In comparison with the data on the physical and mechanical properties of the Tsarev meteorite, new results are considered for determining the strength and deformability under volumetric compression of gabbro, diabase, obsidian, and quartz glass samples (Karman scheme in the modes with 5, 15, 25, 35, and 45 MPa lateral load). The brittleness and strength of the materials is controlled by anomalies in the load-deformation characteristics which correspond to the processes of impact fracture at different stages of deformation of the samples. The change in the state of the substance is controlled simultaneously by the methods of optical fracture-graphy and electron microscopy.

Keywords: ordinary chondrites, cracks, shock metamorphism, durability, fragility

The solution of many cosmological problems which are associated with the destruction of cosmic bodies in their history of origin, evolution and decay requires the development of a theory of strength based on experiments with heterogeneous and multicomponent rocks. It is necessary to adequately describe the variety of forms and mechanical state of the substance of the universe at all stages of its development.

Mineralogical and geochemical analysis of meteorites indicates the advisability of considering the processes of destruction of matter, taking into account the hierarchy of structural and material relations between the main components of extraterrestrial bodies, the organization of which is reflected in different levels of their structure.

These components have a number of individual physical and mechanical properties and are differing in size, shape, concentration and structural position. Their properties largely determine the nature of the reaction of cosmic bodies arriving at Earth in the form of meteoroids. Structural analysis shows that in a number of cases, structural-material associations play an independent role in the structure of matter and can be considered as individual separate formations or bodies. At the same time, the actual theoretical and experimental data, related to such objects that change their behavior both at high thermodynamic parameters and under conditions of dynamic and static influences, are clearly

insufficient. This work is a continuation of our definitions of the parameters of the Tsarev meteorite physical and mechanical properties that were done for the first time under generalized unequal-component compression in the range of side loads of 5 – 35 MPa (Nikitin et al. 2015) on samples of regular shape. The analysis of the obtained results made it possible to draw attention to a number of anomalous effects of the dynamic fracture localization of samples during their transition to the stage of extreme deformation, similar to those previously described by Bridgman and known as "rheological explosion". Comparison of the load-deformation characteristics shape with the nature of Chelyabinsk chondrite destruction, which is reflected in the luminosity curve of the Chelyabinsk bolide, made it possible to make an assumption about the analogy of the dynamic processes of destruction of an asteroid in the atmosphere and samples of the Tsarev meteorite on the press. Analysis of the fracture energy balance, which was carried out on the basis of comparison of the data on the strength of the Tsarev meteorite under uniaxial compression on samples of semi-regular shape with the results of calculations by S.S. Grigoryan, indicates that the process as a whole is determined by the dissipation of internal energy accumulated in the substance at the contacts and phase boundaries of inhomogeneities of different structural levels. The appeal to the physical and mechanical properties of terrestrial analogs of components that are widespread in the composition of ordinary chondrites of the L type is aimed at identifying the sources and forms of destruction depending on the degree of deformation constraint and load intensity.

The object of the study is fragment No. 15383.5 of the Tsarev meteorite L5 S2 W1. According to the structural-petrographic classification data obtained earlier during the study of fragments No. 15380, No. 15384 and No. 15390, the Tsarev meteorite is a shock-metamorphosed brecciated chondrite (Migdisova et al. 1982). Traces of impact events are reflected in the composition and structure of chondrules, the variability of their size and deformation of the contours. Fragments of the martensitic structure observed in inclusions of nickel iron are also of great diagnostic value. Considering all types of chondrules present in the meteorite, one can note their usual variety, starting with the predominant microporphyrite, including radiant, eccentrically radiant and full crystalline, and ending with the least widespread barred chondrules. The matrix binding the chondrules is composed of a fine-crystalline aggregate of silicate grains, opaque minerals, and chondrue fragments. The presence of the latter can be attributed to the result of a shock dynamic event that the meteorite underwent in its cosmic history, just as the bending and deformation of the beams inside the chondrules can be considered as a consequence of the static relaxation of the consequences of this event. The meso construction of the Tsarev sample is shown in figure 1 and 2.

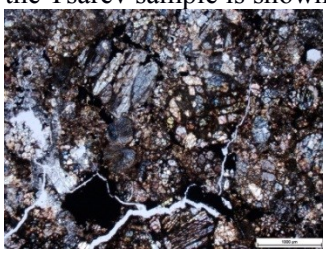

Fig.1. The grain-boundary fracture and crack branching

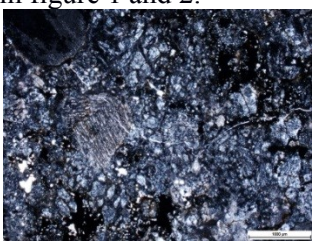

Fig.2. The transform structure of a crack – the main rupture

The choice of terrestrial rocks, considered as analogs of the structural elements of ordinary chondrites, was made taking into account the mineral composition of the meteorite (olivine, pyroxenes, plagioclase, mascelinite, phosphates, nickel iron, troilite, chromite, ilmenite, rutile) and its structural features (crystallized glass), which determine the behavior during deformation and destruction. Samples of *gabbro*, *diabase*, *obsidian* and *quartz glass* served as the objects of studies of terrestrial matter.

The petrographic analysis of the initial structure of the objects made it possible to note some common features inherent in both the meteorite and terrestrial rocks. One of the most striking examples of this generality was the behavior of plagioclase crystals. In gabbro samples, the plagioclase grains, which underwent syngenetic mechanical effects, took a curved shape reminiscent of the curved beams noted in the structure of the chondrules of the Tsarev meteorite. At the same time, the crystals did not lose their continuity, what indicates their deformation in the elastic-plastic state. In diabase, 90% composed of large-tabular grains of plagioclase, polysynthetic forms prevail, the shift along twin seams in which facilitates deformation processes in plasticity. Glasses were chosen as samples of brittle materials of natural (obsidian) and artificial origin.

All types of rocks were tested according to the method previously used in testing a meteorite. Samples of *regular shape* 25x25x50 mm in size were subjected to volumetric compression on an MTS-815 press (Mechanic Test System), equipped with a servo drive and allowing testing according to the Karman scheme, while maintaining the lateral load constant. The tests were carried out under axial compression with lateral thrust ($\sigma_2 = \sigma_3$) = 5, 15, 25 and 35 MPa. The processing of the obtained load-deformation characteristics was carried out by the methods of linear approximation within the limits of elasticity at the prelimiting and transcendental stages, and the values of ultimate loads and deformations were recorded to assess the value of ultimate strength, elasticity in the mode of residual strength. Special

attention was paid to the nature of lateral compression, the registration feature of which was the increased sensitivity of the lateral load stabilization system by the press servo drive to the localization of the fracture processes of the samples during crack growth.

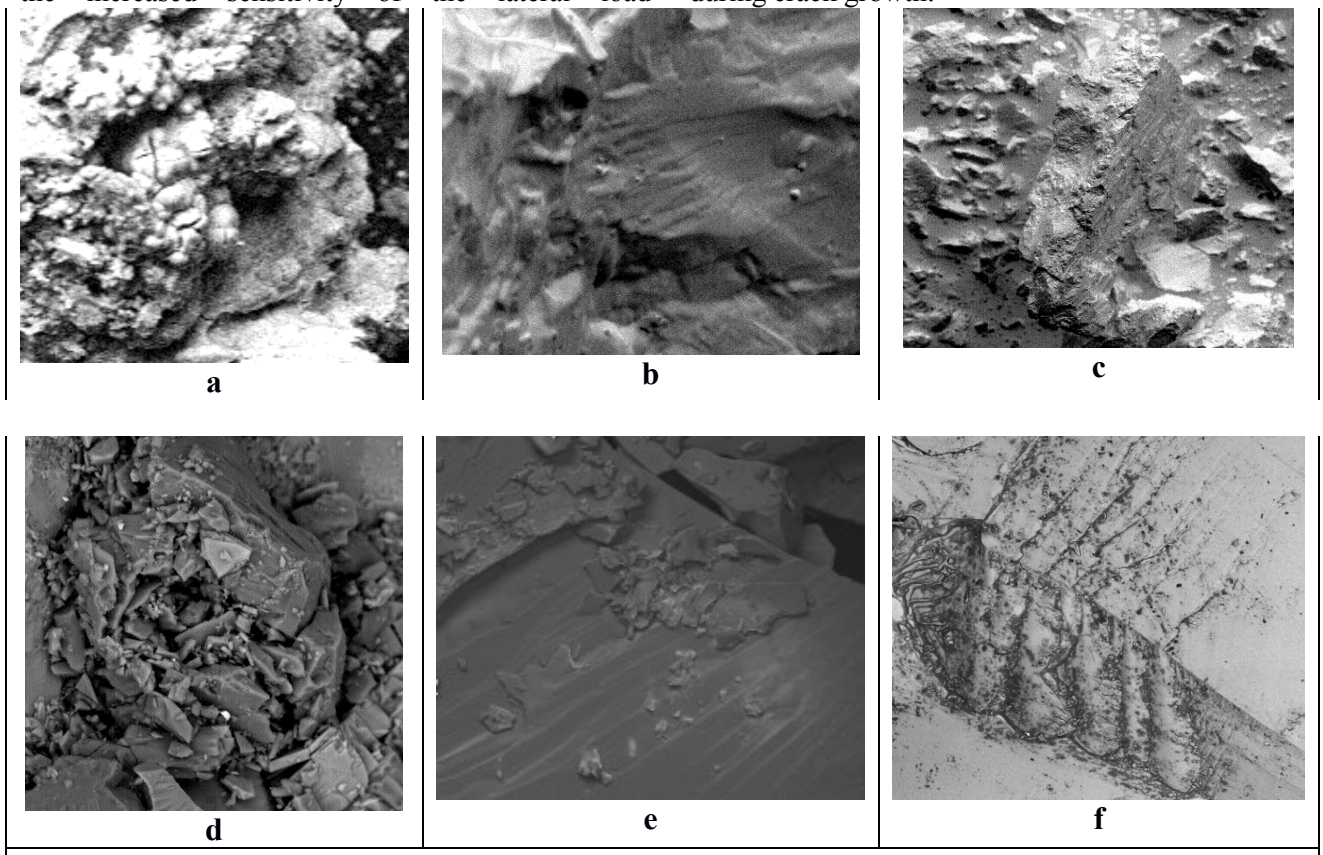

Fig.3. Forms and mechanisms of the destruction of ordinary chondrites and terrestrial rocks. Meteorites: a – SAUH-001, b – Tsarev, c – Ghubara. Rocks: d – Gabbro, e – Diabaz, f – Obsidian.

Analysis of the samples after volumetric compression and granuloscopy of the fractured material was performed using optical (Olimpus) and electron microscopes (VEGA 3 LMH with Oxford Instruments INCA Energy 250 / X-max 20 and Phenom XL). Analysis of the surface images of the samples, figure 3, makes it possible to identify the mechanisms of destruction in the structure of the objects of research. Thus, the destruction of the Sayh al Uhaymir (SAUH-001) meteorite mainly along the boundaries of chondrules is accompanied by the destruction of their complexes with the opening of the internal structure capable of concentrating the energy of brittle destruction, figure 3a. During the destruction of the Tsarev meteorite, photo 3b, a cleavage surface with traces of fatigue growth of a microcrack was found. The destruction of the Ghubara meteorite, photo 3c, is accompanied by intensive crushing of the material with the accumulation of the dust fraction in the mouths and inside the cracks. The microspheroidal organization of the fracture surface of gabbro, resembling microspheres of chondrites, is possibly associated with the microscopic fracture under conditions of rotary deformation modes, figure 3d, and the same block fracture is a characteristic of both diabase and volcanic glass. However, the geometry of their blocks is different. Diabase breaks down into longitudinal blocks, since their shape is determined by the geometry of plagioclase grains, while obsidian blockiness is isometric, figures 3e and 3f.

According to previously obtained data (Slyuta, Nikitin et al. 2010), the investigated meteorites differ significantly in strength. Ghubara is the weakest, its compressive strength is σ_{comp} = 72 MPa, and in tension σ_{tens} = 24 MPa, while SAUH-001 has σ_{comp} = 105 MPa and σ_{tens} = 18 MPa. The Tsarev meteorite turned out to be the strongest σ_{comp} = 188 MPa and σ_{tens} = 30 MPa, but also the most brittle, its brittleness in relative terms σ_{comp} / σ_{tens} is almost 2 times higher than that of the Ghubara meteorite. It is the high brittleness of the Tsarev meteorite that was reflected in the tests in the volumetric stress state that we performed earlier (Nikitin, Pankov et al. 2013). The observed effects of dynamic fracture of the samples manifested themselves in the form of anomalies in the diagrams in the region of ultimate deformation. Dynamic shock processes appeared during the growth of main cracks in a clamped medium.

The defectiveness degree of the samples was evaluated by the velocities of elastic waves, the measurements of which were carried out on a UD2N-

P flaw detector with a frequency of 312.5 kHz, Table 1.

The data obtained when testing samples in a volumetric compression chamber allow us to note a number of features that distinguish the behavior of Tsarev chondrite as a whole from the behavior of its putative components. If the chondrite material in the vicinity of the ultimate loads shows signs of explosive destruction, with a clearly visible negative drop in the load, then even in gabbro the decay modulus is practically similar to the decreasing load of obsidian and quartz glass. A feature of the latter is the ability to exhibit plasticity in the area of large lateral loads, at 45 MPa. In this case, obsidian breaks down brittle and retains its elastic properties up to destruction at the ultimate strength. Separate dynamic events associated with manifestations of brittle fracture are recorded by an alternating anomaly of the lateral load on the sample, figure 1 in table 2. At the same time, ductile fracture corresponds to negative anomalies, and brittle to positive ones. The plasticity of plagioclase diabase is recorded in the entire range of lateral compression, figure 3 in table 2.

Table 1. Physical properties of rock samples – analogs of the substance of ordinary chondrites

No.	Rock	Density, δ, g/cm^3	Elastic wave velocities	
			Vp, m/s	Vs, m/s
1	Gabbro (Golovinskoe deposit)	3,04	6421	3845
2	Plagioclase diabase	2,75	4491	2934
3	Obsidian (Armenia)	2,33	5893	3452
4	Quartz glass	2,84	5839	3456
5	Tsarev meteorite, chondrite L5 S2 W1	3,43	6802	3917

A distinctive feature of the behavior of rocks in the region of 5-10 MPa, i.e. under conditions close to uniaxial compression, is the localization of the maximum strength of the samples in the region corresponding to the residual strength, recorded on the diagrams at medium, 15 -25 MPa, and large lateral loads, 35-45 MPa.

Table 2. The main forms of deformation and fracture of samples in volumetric stress state: figure 1 – the obsidian sample lateral load anomaly, $\sigma_2 = \sigma_3 = 25$ MPa, figure 2 – the obsidian deformation summary diagram, figure 3 – the characteristic of diabase $\sigma_2 = \sigma_3 = 25$ MPa

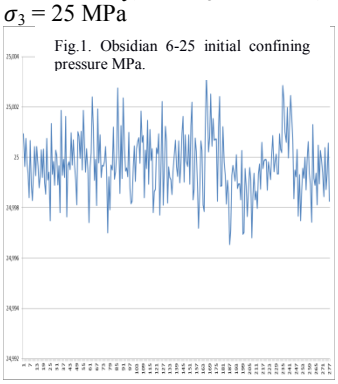

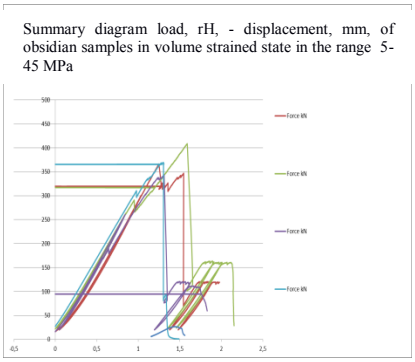

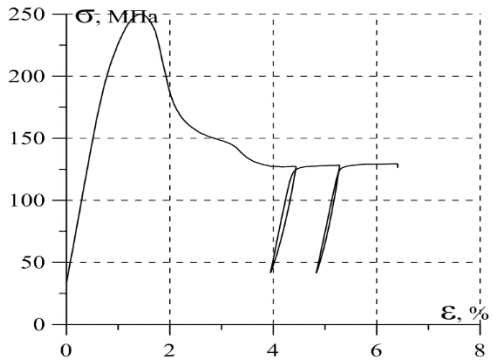

The obtained results of experimental studies confirm the qualitative conclusions regarding the heterogeneity of the mechanisms of deformation and destruction of the substance of ordinary chondrites in terms of the brittleness of chondrules and the viscosity of the matrix and serve as the basis for the development of a numerically provided physical and mathematical model of the destruction process of extraterrestrial matter both in its space history and in the processes of interaction with the planet atmospheres.

The authors express their deep gratitude to the operators who rendered great assistance in carrying out petrographic and electron microscopic studies of the samples: O.Y. Korotchenkova (State Institute of the Ural Branch of the Russian Academy of Sciences), V.I. Khanin and P.V. Vakhaev (Melitek LLC), M.S. Nikolsky (IGEM RAS).

References

Migdisova L.F. et al. Features of the composition and structure of the Tsarev meteorite. Meteoritics, issue 41, 1982. S.13-30.

Nikitin S.M. et al. Deformation and Fracture of Tsarev Meteorite Samples under Volume Compression. Proceedings of VESMPG-2015, M. 2015.S. 311-315.

Slyuta E. N. et al.Strong physical and mechanical anisotropy of ordinary chondrites. 40th Lunar and Planetary Science Conference, Abstr.1051 (2010).

Shornikov S. I.[1], Yakovlev O. I.[1] The chemical fractionation of perovskite at evaporation

[1]V. I. Vernadsky Institute of Geochemistry & Analytical Chemistry RAS, Moscow, (sergey.shornikov@gmail.com)

Abstract. The effect of redox conditions on the direction of melt composition changes at evaporation is shown for the perovskite melt. The proposed approach allows us to take into account the experimental conditions and calculate the thermodynamic parameters characterizing the melt evaporation.

Keywords: thermodynamic properties of oxide melts, evaporation, perovskite $CaTiO_3$

As it was shown earlier (Yakovlev & Shornikov, 2019), the chemical fractionation of a melt during evaporation under vacuum conditions can be calculated using the Hertz-Knudsen equation for the evaporation rate (J) of a component from a multicomponent melt, taking into account the Raoul-Henry law:

$$J = \frac{x\gamma p^{\circ}}{\sqrt{2\pi RTM}}, \quad (1)$$

where x, γ, p°, M are the concentration (mole fraction), activity coefficient, vapor pressure, and molecular weight of the melt component, respectively. The equation (1) does not specify the component evaporation coefficient, which can be ignored in the case of melt evaporation (Shornikov, 2015).

The vapor pressure of the melt components (CaO and TiO_2) can be easily calculated from thermochemical data (Glushko et al., 1978–1982; Balducci et al., 1985): 1.514×10^{-5} and 2.702×10^{-5} atm at 2278 K, respectively. Based on the data on activity coefficients of oxides in the CaO–TiO_2 melts, determined by the Knudsen mass spectrometric effusion method (Shornikov, 2019), it is possible to calculate the change of the perovskite melt composition at evaporation. As can be seen from Fig. 1**a** (line **1**), the melt loses TiO_2 to a concentration of 41.25 mol % TiO_2 and congruently evaporates under the condition:

$$\frac{x_{CaO}\gamma_{CaO}p^{\circ}_{CaO}}{\sqrt{M_{CaO}}} = \frac{x_{TiO_2}\gamma_{TiO_2}p^{\circ}_{TiO_2}}{\sqrt{M_{TiO_2}}} = 2.263\times10^{-7}\ \text{atm}\times(\text{g/mol})^{-1/2}. \quad (2)$$

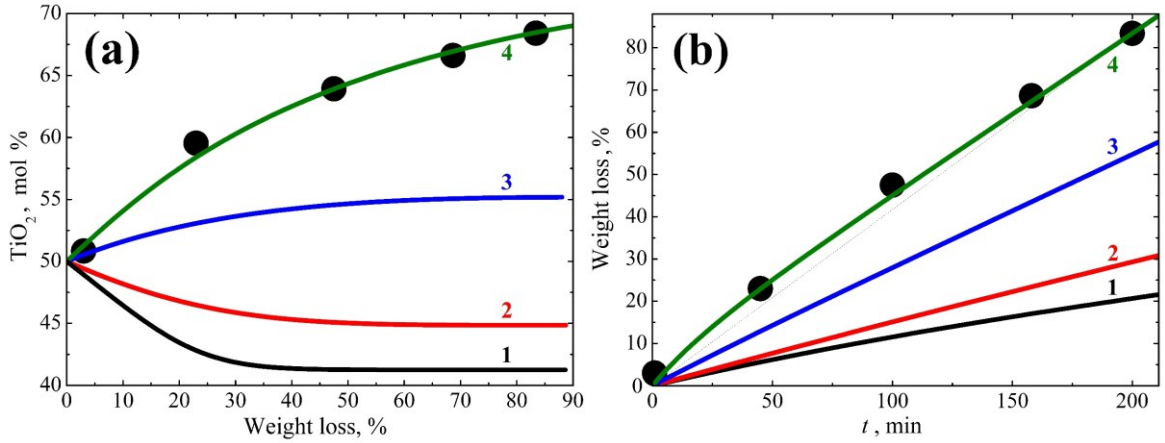

Fig. 1. Dependences of changes in the composition (a) and weight (b) of perovskite melt during evaporation at 2278 K, determined experimentally (symbols) by Zhang et al. (2014) and calculated in the present study (lines): 1 – without taking into account redox conditions; 2 – for the case of neutral redox conditions; 3 – for the case of the melt evaporation from a molybdenum effusion cell (according to Knudsen); 4 – for the case of the melt evaporation in a vacuum furnace with a tungsten heater (according to Langmuir).

Table 1. Equilibrium constants of perovskite evaporation reactions at 2278 K (Glushko et al., 1978–1982; Balducci et al., 1985; Shornikov, 2019)

Reaction		Equilibrium constants of reaction	$K_{r_i,2278}$
$\{CaTiO_3\} = (CaTiO_3)$	(3)	$K_3 = p_{CaTiO_3} / a_{CaTiO_3}$	7.267×10^{-9}
$(CaTiO_3) = (CaO) + (TiO_2)$	(4)	$K_4 = p_{CaO}p_{TiO_2} / p_{CaTiO_3}$	2.372×10^{-6}
$(CaO) = (Ca) + (O)$	(5)	$K_5 = p_{Ca}p_O / p_{CaO}$	3.573×10^{-4}
$(TiO_2) = (TiO) + (O)$	(6)	$K_6 = p_{TiO}p_O / p_{TiO_2}$	1.917×10^{-7}
$(TiO) = (Ti) + (O)$	(7)	$K_7 = p_{Ti}p_O / p_{TiO}$	5.351×10^{-10}
$2(TiO_2) = (Ti_2O_4)$	(8)	$K_8 = p_{Ti_2O_4} / p^2_{TiO_2}$	3.197×10^{-3}
$(Ti_2O_4) = (Ti_2O_3) = (O)$	(9)	$K_9 = p_{Ti_2O_3}p_O / p_{Ti_2O_4}$	2.092×10^{-8}
$(O_2) = 2(O)$	(10)	$K_{10} = p^2_O / p_{O_2}$	1.872×10^{-5}
$\{CaTiO_3\} = [CaO] + \{TiO_2\}$	(11)	$K_{11} = a_{CaO}a_{TiO_2} / a_{CaTiO_3}$	8.551×10^{5}
$[CaO] = (CaO)$	(12)	$K_{12} = p_{CaO} / a_{CaO}$	1.225×10^{-7}

Reaction		Equilibrium constants of reaction	$K_{r_i,2278}$
$\{TiO_2\} = (TiO_2)$	(13)	$K_{13} = p_{TiO_2} / a_{TiO_2}$	2.264×10^{-5}
$[W] + 3(O) = [WO_3]$	(14)	$K_{14} = a_{WO_3} / a_W p_O^3$	3.054×10^{14}

Note: the gas phase is indicated in parentheses, the crystal phase in square brackets, and the liquid phase in curly brackets.

From experimental data (Shornikov, 2019), it follows that the perovskite melt $\{CaTiO_3\}$ evaporates forming a gaseous perovskite ($CaTiO_3$) according to the reaction (3). ($CaTiO_3$) dissociated according to the reaction (4) to gaseous oxides (CaO) and (TiO_2). They form the gas phase composition over the melt according to the reactions (5) – (10), presented in Table. 1. We neglect insignificant amounts of molecules (Ca_2), (O_3) and (O_4) in the gas phase (less than 10^{-7} mol %).

Based on the equilibrium constant values (K_r) given in Table 1 and experimental concentration dependences of CaO, TiO_2 and $CaTiO_3$ activities (a_i) in the CaO–TiO_2 melts at 2278 K (Shornikov, 2020), the total vapor pressure (p_{tot}) and partial pressures of vapor species (p_i) for any melt composition evaporating under various redox conditions determined by the oxygen partial pressure (p_O) were calculated. In this case the vapor pressure of the melt component in the equation (1) was calculated from the partial pressure of the prevailing vapor species over [CaO] and $\{TiO_2\}$ – (Ca) and (TiO_2), respectively, according to the equation:

$$p^\circ - \mu_i \prime x_i, \quad (15)$$

where x_i is the concentration of (Ca) and (TiO_2) in the vapor over the oxides, equal to 0.548 and 0.839 at 2278 K, respectively. The calculation results are shown as lines in Fig. 1 and 2**a**–**c**.

The p_O value is such that the p_{tot} over the perovskite melt is minimal (Fig. 2**a**, symbols **I**) in the absence of redox effects. In this case the perovskite melt loses TiO_2 at evaporation to a concentration equal to 44.83 mol % TiO_2 which evaporating congruently (Fig. 1**a**, line **2**). The difference from the calculation results according to equation (1) (Fig. 1**a**, line **1**) can be caused by the presence of a gaseous ($CaTiO_3$) in the gas phase, which prevents the $\{TiO_2\}$ loss in the condensed phase, which was neglected in these calculations.

From a comparison of the concentration dependences of partial pressures of vapor species over the CaO–TiO_2 melts at 2278 K, calculated in the absence of redox effects (Fig. 2**c**) and experimentally determined by evaporation from a molybdenum effusion cell (Fig. 2**d**), we can easily see the increase of the total vapor pressure (Fig. 2**d**, line **11**) caused by the increase of p_{Ca} (Fig. 2**d**, line **1**) and p_{TiO} (Fig. 2**d**, line **4**) due to the p_O decreasing (Fig. 2**d**, line **9**) according to equilibria (5) and (6), respectively. The observed regularities in the dependence of p_i *vs*. p_O in the case of evaporation of perovskite from a molybdenum effusion cell (Fig. 1**a**, line **3**) lead to the enrichment of the melt by $\{TiO_2\}$ to a concentration of 55.18 mol % TiO_2, which then evaporates congruently (without the composition changing).

Experimental results obtained by Zhang et al. (2014) on evaporation of the perovskite melt at 2278 K using a tungsten furnace in a vacuum (not exceeding 1.32×10^{-9} atm) are shown in Fig. 1 and Fig.2 (**a**, **b)**.

Significant chemical fractionation of the perovskite melt can be observed: with the wight loss equal to 83.40 wt %, the concentration of $\{TiO_2\}$ in the melt was 68.30 mol % TiO_2 (Fig. 1**a**). There is also an increase in the evaporation rate (Fig. 1**b**, symbols and line **4**) in comparison with those for cases of melt evaporation in chemically neutral conditions (Fig. 1**b**, lines **1** and **2**) and from a molybdenum effusion cell (Fig. 1**b**, line **3**), determined by the angle of inclination of the weight loss dependences on the evaporation time. Calculated from data obtained by Zhang et al. (2014), the p_O over the melt was 8.53×10^{-8} atm (Fig. 2**a**, symbols **III**, line **9**), which is approximately 3 times less than the equilibrium value in the conditions of a molybdenum effusion cell, equal to 2.72×10^{-7} atm (Fig. 2**a**, symbols **II**, line **9**).

The character of perovskite melt evaporation is probably due to the reactions of oxygen species of the gas phase over the melt with the material of tungsten heater, which could be formed gaseous tungsten oxides (WO_2) and (WO_3). This processes lead to reduce the amount of (O) and (O_2) in vapor, and along with that according to the equilibrium constants of reactions (5) – (10) it increase the partial pressure of oxygen deficient molecular vapor species – (Ca), (Ti), (TiO), (Ti_2O_3) and the total vapor pressure over the melt, which ultimately determines the evaporation trend of the melt. Note that the presence of reducing conditions does not affect the values of partial pressures of (CaO), (TiO_2), (Ti_2O_4) and ($CaTiO_3$) (Fig. 2**a**, lines **2**, **5**, **7**, **8**).

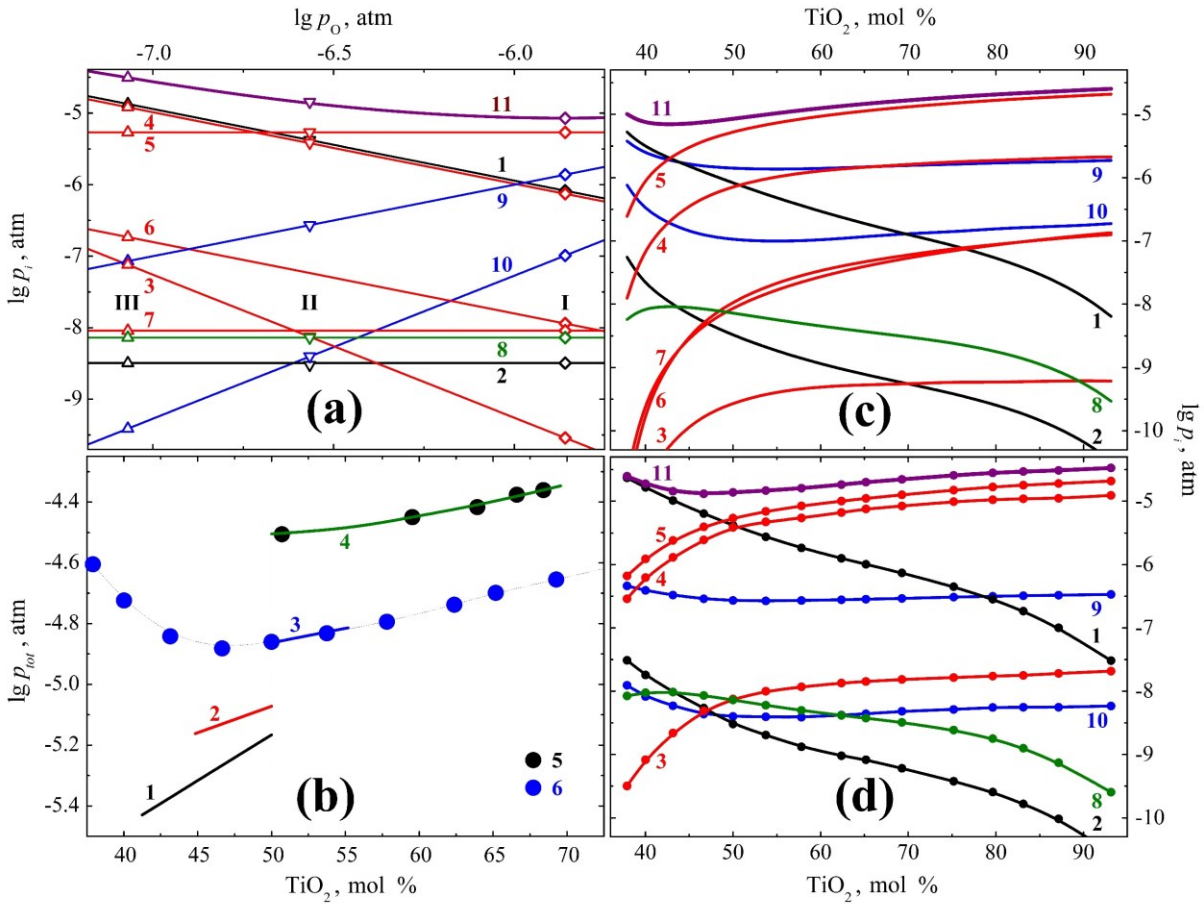

Fig. 2. The total and partial pressures of vapor species over perovskite melt *vs*. p_O (a), during its evaporation at different redox conditions (b), over the CaO–TiO_2 melts in the absence of redox effects (c) and at evaporation from molybdenum effusion cell (according to Knudsen) (d) at 2278 K.

Table of symbols:

(a) the symbols correspond to those determined experimentally during {$CaTiO_3$} evaporation from a molybdenum effusion cell (Shornikov, 2019) (II), as well as those calculated in the absence of redox effects (I) and for the case of reducing conditions in a vacuum furnace with a tungsten heater according to Langmuir (III): 1 – (Ca); 2 – (CaO); 3 – (Ti); 4 – (TiO); 5 – (TiO_2); 6 – (Ti_2O_3); 7 – (Ti_2O_4); 8 – ($CaTiO_3$); 9 – (O); 10 – (O_2); 11 – the total vapor pressure.

(b) the symbols (1–4) correspond to those in Fig. 1; 5 and 6 are the results obtained in (Zhang et al., 2014) and (Shornikov, 2019), respectively.(c, d) the symbols (1–11) correspond to those in Fig. 2a.

The [WO_3] presence in amount from 0.06 to 0.6 wt % in the CaO–MgO–FeO–Al_2O_3–TiO_2–SiO_2 residual melts found in similar experiments performed by Wang et al. (2001) on the same equipment used in (Zhang et al., 2014) indicates the course of the reaction (14), which characterizes similar interactions with the heater material. However, the calculation of the p_O value over the perovskite melt according to the reaction (14) is complicated by the lack of data on the [WO_3] activity (or other possible tungsten oxides) in the residual melts.

Thus, in the present study the effect of redox conditions determined by the oxygen partial pressure on the direction of changes in the melt composition during evaporation is shown by the example of perovskite melt evaporation. The proposed approach allows us to take into account the conditions of the experiment and calculate the thermodynamic parameters characterized the melt evaporation process and the evaporation trend.

The present study was supported by the Russian Foundation for Basic Research (grant #19-05-00801A).

References

Balducci G., Gigli G., Guido M. (1985) Identification and stability determinations for the gaseous titanium oxide molecules Ti_2O_3 and Ti_2O_4. *J. Chem. Phys*., vol. 83, no. 4, pp. 1913–1916.

Glushko V. P., Gurvich L. V., Bergman G. A., Veitz I. V., Medvedev V. A., Khachkuruzov G. A., Yungman V. S. (1978–1982) Thermodynamic properties of individual substances. Moscow: Nauka, vol. 1–4.

Shornikov S. I. (2015) Vaporization coefficients of oxides contained in the melts of Ca–Al–inclusions in chondrites. *Geochem. Int*., vol. 53, no. 12, pp. 1080–1089.

Shornikov S. I. (2019) Mass spectrometric investigation of evaporation processes of perovskite. *Russ. J. Phys. Chem. A*, vol. 93, no. 6, pp. 1024–1031.
Shornikov S. I. (2020) Study of $CaO–TiO_2$ melts by Knudstn effusion mass spectrometry. *Russ. J. Phys. Chem. A*, vol. 94, no. 7, pp. 1289–1299.
Wang J., Davis A. M., Clayton R. N., Mayeda T. K., Hashimoto A. (2001) Chemical and isotopic fractionation during the evaporation of the $FeO–MgO–SiO_2–CaO–Al_2O_3–TiO_2$ rare earth element melt system. *Geochim. Cosmochim. Acta*, vol. 65, no. 3, pp. 479–494.
Yakovlev O. I., Shornikov S. I. (2019) Chemical and isotopic fractionation of magnesium and silicon at evaporation of Ca–Al–inclusions of chondrites. *Geochem. Int*., vol. 57, no. 8, pp. 851–864.
Zhang J., Huang S., Davis A. M., Dauphas N., Hashimoto A., Jacobsen S. B. (2014) Calcium and titanium isotopic fractionations during evaporation. *Geochim. Cosmochim. Acta*, vol. 140, pp. 365–380.

Tselmovich V.A.[1], Maxe L.P.[2] Microstructure and composition of particles of native iron of cosmic origin UDC 523.681

[1]GO Borok IPE RAS, [2]LLC «MAERPRO», Mogilev, Republic of Belarus, (tselm@mail.ru, larissa_maxe@rambler.ru)

Abstract. In this work, the authors identified and studied iron particles extracted from samples of native trepel and magnetic concentrate of trepel as carriers of information about their origin using TMA and EMA method, pointed out their informative content, and explored the morphology and composition of particles in the content of astromineralogy of native metals and hydride theory. Scaly particles of native iron are found in a variety of environments of different ages and origin: peat, trepel, sedimentary rocks. They can be considered as highly informative indicators of cosmic dust.

Keyword: native iron, electron microprobe analysis, cosmic dust, trepel

Introduction. Native pure Iron (PI), which is found in meteorites, sediments, and various terrestrial rocks (from xenoliths and mantle hyperbasites to ocean basalts and Siberian traps), is an important source of information about a wide range of geophysical processes, as well as processes in near-earth and interstellar space. Electron microprobe analysis (EMA) and thermomagnetic analysis (TMA) of PI samples allow us to form a database on the origin and transformation of chemical elements in the course of the evolution of matter in the Universe.

The features of PI particles found in earth rocks include not only their magnetic properties, but also their distinctive morphological characteristics. Many scientific papers have been devoted to the study of PI in objects and rocks [Pechersky et al., 2012-2019], they discuss the results of EMA and TMA and form conclusions based on them. In relation to the PI from the Chelyabinsk meteorite [Markov et al., 2015], it was shown that the main magnetic minerals of the meteorite are represented by two groups of PI, more precisely, two iron-nickel alloys (differing in different concentrations of Nickel: low and relatively high) and iron sulfides. The results of EMA and TMA allowed us to conclude that the alloys have the same crystal lattice (volume-centered) of kamacite. In the Chelyabinsk meteorite, magnetite balls were also found, which are typical for other meteorites and sediments, but they are products of melting of the meteorite in the earth's atmosphere (iron compounds are oxidized to magnetite) [Markov et al., 2015].

At the same time, the generalization of the results of TMA and EMA of many samples of meteorites of different types, allowed us to come to the conclusion about three groups of native metals in meteorites and two main "methods" for the formation of pure Iron. Native Iron can crystallize from the melt, but it can also be formed when a solid iron-nickel solution is broken down. Thus, in the composition of meteorites and meteoritic matter, native Iron and two of its alloys with Nickel (an alloy with a low concentration of Nickel and a high one) are observed [Pechersky et al., 2015]. It should be noted that both the first and second variants of the formation of native Iron also indicate variants of the formation of pure Nickel, which will be taken into account by the authors in this work.

Further research has revealed that the particles of native Iron found in the earth's rocks are similar in composition, shape and size to the particles of extraterrestrial Iron extracted from sediments and meteorites, and, unlike meteorites, Nickel-free ones prevail among them. It was assumed that the predominance of PI in sediments is due to the fact that interplanetary dust gets mainly the material of the upper mantle of the planets – sources of dust, while the material of the lower mantle and the core of the planets get to the Earth mainly in the form of meteorites. Based on the results of a number of studies, D. M. Pechersky [Pechersky et al., 2012 – 2019] proposed a model of the structure of planets in the Solar system, the "core" of which is native Iron and iron-nickel alloys [Pechersky et al., 2017]. The problem of recognizing the origin of PI was solved by analyzing Quaternary period sediments using EMA and TMA, compared with previously studied objects in Eurasia and the Atlantic, and concluded that the predominantly cosmic origin of native Iron in the objects of study [Pechersky. et al., 2013]. In sedimentary rocks, there are also particles of pure Nickel of extraterrestrial (cosmogenic) origin, since particles of cosmic dust constantly falling to Earth contain Nickel. In sedimentary rocks, there are also particles of pure Nickel of extraterrestrial (cosmogenic) origin, since particles of cosmic dust constantly falling to Earth contain Nickel [Tselmovich et al., 2019].

The informativeness of CS, theory and practical problem. Earlier, using EMA and TMA, the authors studied the cosmogenic substance (CS) extracted from the trepel of the Stalnoye field (Republic of Belarus) – a sedimentary rock formed in the period 60 – 30 million years ago and concluded that the composition of the total background flow of iron particles (PI, alloys, magnetite) in different geological periods is approximately the same [Tselmovich et al., 2019].

The information content of CS differs significantly and is due to the long cosmic history of the condensed phase of matter from stellar synthesis to "arrival" on Earth. Not the identity of the informational content of meteors and meteorites was expressed and justified theoretically [Larin, 1975]. Meteorites reach the Earth's surface and leave an information trail concentrated in local sediments. Meteors and most of the bolides are completely destroyed in the atmosphere, undergoing physical and chemical changes (during the explosion, combustion in the atmosphere) and fall out as fragments and particles of varying degrees of change of the original body. Accordingly, bolides, meteorites and meteors leave a different information trail in the earth's precipitation. It was suggested that in the oxygen atmosphere of the Earth, meteor matter is differentiated and transformed depending on the heating temperature and interaction with oxygen. The oxygen atmosphere is the reason for the separation of meteor matter into a combustible and non-combustible part: non-combustible fragments reach the Earth's surface [Larin, 1975]. Differences in the composition of meteorites can be observed visually by the melted crust and their internal parts, represented in different collections (oxidized part, fused and fragments that were not affected by interaction with the atmosphere).

The nature of meteor combustion in the atmosphere, spectral characteristics indicate the reaction of hydrides and, accordingly, their presence in the composition of meteors. Scientific research and the hypothesis about the role of hydrides in the formation of the condensed phase of matter allowed us to create a hydride theory that postulates the initially hydrogen (hydride) composition of the Earth and the consequence of which is the predominance of metals in the composition of the planet [Larin, 1975]. Information differences in space dust, meteor and meteorite matter serve as a basis for hypotheses and theories of the origin of native metals on Earth, the formation of planets and their evolution.

The Earth's hydride theory can be used to analyze the composition and morphology of cosmogenic matter extracted from earth's sediments [Persikov et al., 2019; Manankov, 2014; Larin, 1975]. In the works of scientists, native metals (NM) are considered either from the positions of their origin and transformations on Earth, within the framework of Geophysics and Geochemistry, or from the positions of astrophysics and astrochemistry – stellar synthesis and evolution of chemical elements.

When studying the samples of trepel from the "Stalnoye" field, the authors assumed that the rock is a kind of collector of CS, can contain NM, can accumulate and store matter, both of geological events and events of astronomical scale. The extraction of particles that can be attributed to CS or the substance of geochemical transformations was carried out using neodymium magnets and the schlich method.

In this work, the authors identified and studied by TMA and EMA method iron particles extracted from private samples of native trepel and magnetic concentrate from trepel as carriers of information about their origin, noted their informative content, and considered the morphology and composition of particles in the light of astromineralogy of native metals and hydride theory [Manankov, 2014; Larin, 1975]. Standard research tasks focused on the search for possible "prints" of space processes, NM transformation in vacuum, and transformation processes in the atmosphere and water environment.

EMA of particles of CS. From the accumulated database of TMA and EMA particles extracted from native trepel and magnetic trepel concentrate, as well as particles extracted from peat (deposits of the Republic of Belarus), 15 were selected for comparative evaluation. Data from the EMA (TESCAN VEGA 2, GO "Borok", IPE RAS) are shown in figures 1 and 2.

The Fig. 1a and 1b are images of the inner regions of the magnetite spheres, which reflect the compression of a molten metal jet in a magnetic field and its twisting. Images indicate a high temperature difference between the outer and inner layers of the sphere's substance. In both cases, there is a correlation between the thickness of the jet and the thickness of the sphere itself.

The image in Fig. 1c represents an elongated (from the melt) particle with a "screw" step of about 20 microns. The twisting of jets of liquid metals and alloys is caused by the magnetohydrodynamic properties of a melt moving in a magnetic field [Frick et al., 2009, Jaworski et al., 2010]. The elongation of the particles and the pitch of the "screw" most likely depend on its mass and chemical composition, the speed of movement in the dense layers of the atmosphere.

The morphology of the particles shown in Fig. 1a, 1b, and 1c is due to the transformation, probably multiple, of their original composition and original shape.

Fig. 1d it is an image of an Mt-sphere filled with products of high-temperature exposure – a kind of "slag".

On the ablation sphere in Fig. 1e, the "center" is visible, and on the surface there are several particles of iron sulfide, presumably biogenic (macroscopic inclusions of biogenic pyrite on the remains of ancient organisms are observed on the freshly excavated trepel).

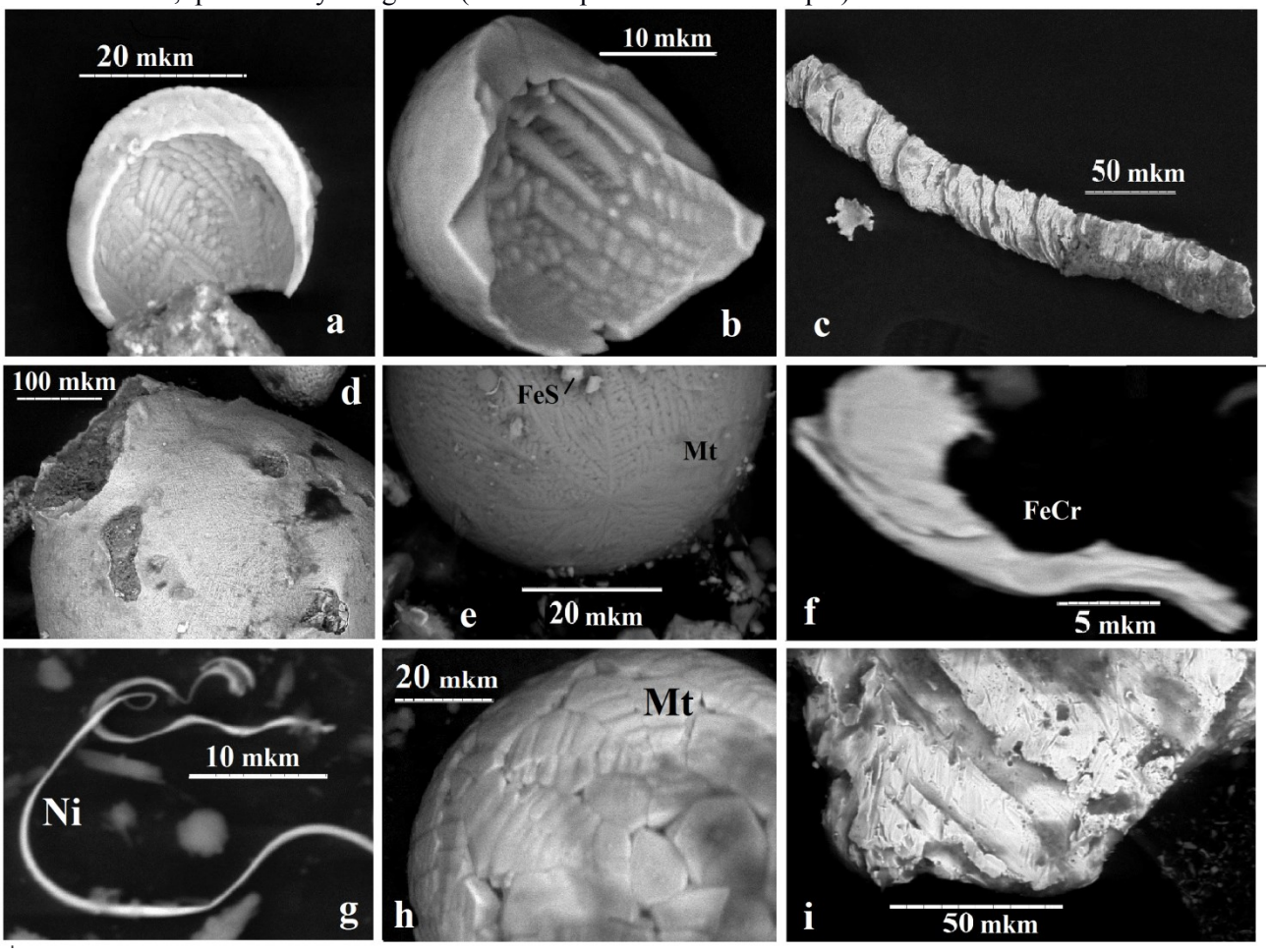

Fig. 1. CS particles with traces of impact by the earth's magnetic field and atmosphere.

The particle of the intermetallic compound in Fig. 1f presumably has a trace of temperature and magnetic influence hat caused the stratification of the jet.

Images of particles in Fig. 1g and 1h indicate the probability of the origin of the Nickel "tape", as a native metal, by its displacement from the magnetite sphere, similar to the one shown in Fig. 1h, the melting temperatures of the Iron, magnetite and Nickel alloy are different, Nickel remains longer in the molten form and can be displaced between the crystallites by an explosive process. The combustion of Iron, in the presence of water or in water, is accompanied by the release of hydrogen and oxygen, which form a mixture, explode and create excess pressure.

The smooth surface of the particle in Fig. 1i and indicates its iron-nickel composition, a pattern characteristic of petrographic polished thin sections of FeNi-alloy is noticeable.

Fig. 2 presents particles of native Iron. The iron particles of scaly form in Fig. 2a, 2b and 2c have characteristic features: they are permeated with micropores whose holes expand outward.

The image in Fig. 2a allows us to consider these peculiar "exhausts", which can be considered as traces of the initial presence of the gas-forming component in the cosmogenic particles of NM.

In the particles shown in Fig. 2a, 1b and 2c, micropores and cavities are not filled with oxidation products and do not bear traces of subsequent bio-damage. At the same time, on the surface of these scales, there are equally smooth round holes that can be traces of the impact of particles with very high, probably cosmic energy.

The series of particles, shown in Fig. 2d, 2e, and 2f represent the modified NM.

Fig. 2d shows a NM particle on the surface of which hematite was formed.

Fig. 2f represents a surface that has been subjected to bio-damage, it shows "vents" (5 – 10 microns) - gas outlet holes and traces of chemical transformation of the substance (cracking).

The fragment of the Mt-sphere is a hemisphere, in Fig. 2e, and contains loose non-metallic products and NM particles as a container.

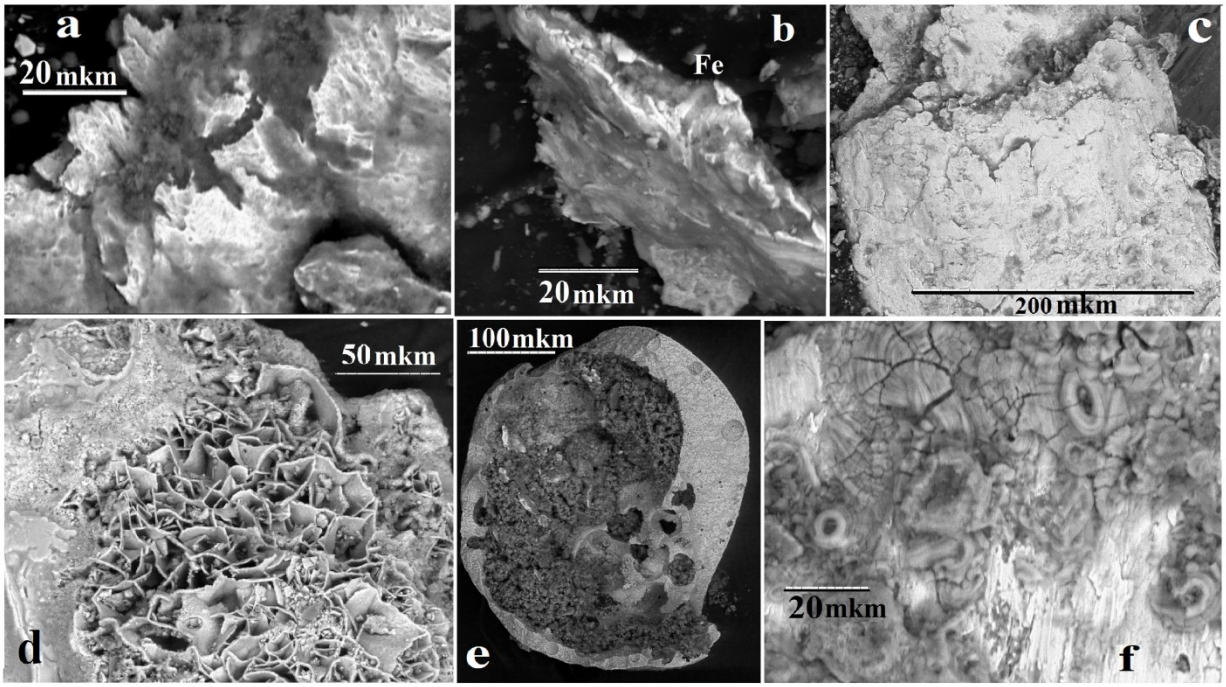

Fig. 2. Particles of cosmogenic substances – NM and particles that were transformed by terrestrial environment.

Conclusions. Scaly particles of native metals and a special case – PI are found in a variety of environments of different ages and origin: peat, trepel, sedimentary rocks. They can be classified as highly informative indicators of CS, they are more saturated with primary information about the composition and morphology than twisted in a spiral and particles-microspheres. Biodegradation of scaly particles NM lower their cosmogenic information, but may indicate geochemical processes in paleoperiods. Converted CS particles have less cosmogenic information, but more geochemical.

The work was done according to the state task № AAAA-A17-117040610183-6

References

Larin V. N. Hypothesis of initially hydrid Earth (new global concept). Moscow, "Nedra", 1975. 100 p.

Manankov A.V. Geochemistry of native metals and intermetallic compounds on the Earth, in meteorites and on the Moon // Structure and properties of metals under various energy effects and technological treatments: Materials of the scientific seminar with international participation/ Vol. to 80th anniversary of Prof. Kozlov E. V. Tomsk: TSUAE. 2014, P. 79 – 86.

Markov G. P., Pechersky D. M., Tselmovich V. A. Magnetic minerals of the Chelyabinsk meteorite. // Astronomical Bulletin. Exploration of the solar system. 2015, T 49, № 5. P. 340 – 352.

Persikov E. S., Bukhtiyarov P. G., Aranovich L. Ya., Nekrasov A. N., Shaposhnikova O. Yu. Experimental modeling of the formation of native metals (Fe, Ni, Co) in the earth's crust during the interaction of hydrogen with basalt melts. // Geochemistry, 2019, Vol. 64, № 10. P. 1015 – 1025.

Pechersky, D. M., Markov, G. P., Tselimovich V. A., Sharonova Z. V. Extraterrestrial magnetic minerals. // Physics of the Earth, 2012, № 7 – 8. P. 103 – 120.

Pechersky D. M., Markov G. P., Tselimovich V. A. The pure Iron and other magnetic minerals in meteorites. // Astronomical Bulletin. Research. solar system. 2015, T 49. № 1. P. 65 – 75.

Pechersky D. M., Kuzina D. M., Markov G. P., Tselmovich V. A. Native Iron on the Earth and in space. // Physics of the Earth, 2017, № 5. P. 44 – 62.

Frick P. G., Khripchenko S. Yu. Magnetic hydrodynamics - from problems of metallurgy to galaxies // Bulletin of the Perm scientific center, 2009, № 1. P. 5 – 9.

Tselmovich V. A. Pure Nickel as an indicator of cosmogenic substance // Proceedings of the 19th international conference "Physico-chemical and petrophysical research in Earth Sciences", Moscow, 2018. P. 330.

Tselmovich V. A., Kurazhkovsky A. Yu., Kazansky A. Yu., Shchetnikov A. A., Blyakharchuk E. A., Fillipov D. A. // Research of dynamics of space dust arrival on the earth's surface by peat deposits. / Physics of the Earth, 2019, № 3. P. 150 – 160.

Tselmovich V.A., Maxe L. P. Cosmogenic substance from the trepel of the "Stalnoye" field // Proceedings of the all-Russian annual seminar on experimental Mineralogy and Geochemistry. 2019. P. 325 – 328.

Jaworski M. A. et al. Thermoelectric Magnetohydrodynamic Stirring of Liquid Metals. Phys. Rev. Lett. 104, 094503 (2010).

Yurkovets V.P. General morphological features of some fragments of the Ladoga space body UDC 551.4:552.6

The Academy of DNA Genealogy, Boston, USA
(valery.yurkovets@gmail.com)

Abstract. The study of the catastrophe layers of the near zone of the Ladoga impact led to the discovery of several fragments of the Ladoga space body that had a common for this group morphology. The article offers a probable explanation for the discovered phenomenon.

Keywords: Ladoga impact-volcanic structure; catastrophe layers; meteorites

The experience of studying Ladoga impact-volcanic structure has shown, among other things, that some features of external appearance can be common (uniform) for stone meteorites if they are fragments of a single maternal body formed in the course of its destruction when approaching to the Earth, and, in addition, if they are represented by magmatics of extraterrestrial origin which have primary jointing. Thus, more than a dozen stone meteorites tentatively attributed to eucrites were found in catastrophe layers of the near zone of the Ladoga impact during several years of its study (Yurkovets, 2015).

Fig. 1.

Along with their uniform structural and textural features, magnetism, common petrologic composition, the same density, the same cellular structure of the surface, the presence of extraterrestrial minerals in the composition, most of the samples obtained in the catastrophe layers of the near zone of the Ladoga impact which assume to have fragments of Ladoga space body in the composition, have a common, regardless of the size, macro form - spherical, somewhat elongated along one of the edges tetrahedron.

By catastrophic layers in impactology is meant sedimentary bedrocks, usually clays, with a mixture of products of shock metamorphism - the smallest fragments of diaplectic and high-pressure minerals, microspheres of impact glass (with sizes of a maximum of tens of microns), small fragments of meteorites very seldom. The thickness of such layers is small (rarely more than 1-2 cm) and meets the estimated amount of ultra-thin (dust) emissions for a crater with a diameter of more than 100-150 km, provided that this material is more or less evenly distributed across the Earth surface (Feldman, 1999). That is, “classic” catastrophe layers - the result of atmosphere emission of the finest products of the impact, which after a long journey in suspension covered the surface of our planet with an even layer.

As for the catastrophe layers of the near zone, they are named so for an analogy because they were formed simultaneously with the material of “classic” catastrophe layers and as a result of the same processes. The fundamental difference is that in the near zone the impact products are scattered at cosmic speeds, as a result of which they largely become agents of impact metamorphism in rocks exposed to them (Yurkovets, 2016). In addition, in the near zone no glass is formed - here there is evaporation of impacter and target rocks and fragments of the space body have an independent meteorite origin and “macroscopic” (up to a few tens of centimeters across) size - fig. 1. Their presence in catastrophe layers of the near zone can be explained by the particles fall continuing after the fall of the main, that were formed as a result of main body destruction in the gravitational field of the Earth after passing Roche limit - the boundary where its own gravity becomes less than the gravity of the approaching Earth (Pukhlyakov, 1970).

Fig. 2

Apparently, they are small fragments of larger bodies that accompanied their fall along with the main group. As it is seen in fig. 1 there is a clear trend - the more large-grained is the structure of the particle, the larger is the fragment itself. Fig. 2 shows a close-up view of comparison of the two most expressive patterns: with medium-grain and fine-grain structure (bottom and upper respectively). The fragment with a medium-grain structure is many times larger than the fragment with a fine-grain structure. It follows that the size of meteorite jointing is a function of the size of grain in it.

Perhaps the only reason that can be offered as an explanation for the formation of Ladoga fragments of this natural shape and size related to the grain size is the primary jointing in eucrites which are magmatics, that perhaps once formed Vesta asteroid which eucrites are close in composition to Ladoga asteroid (Yurkovets, 2015). Primary jointing is formed when cooling down magmatics forming a system of intersecting cracks, where, apparently, there is destruction of the cosmic body when it crosses the Roche limit.

As for the relation of the size of particles and grain, the only thing that can be said with certainty so far is that such a relation is obvious. Perhaps its causes will be found in some structural features of Ladoga eucrite.

References

Pukhlyakov L. A.. Review of tectonic hypotheses. Tomsk. TSU publishing house. 1970. 266 p.

Feldman V. I. Petrology of impactites. M.: MSU publishing house. 1990. 300 p.

Yurkovets V. P. 2015. Extraterrestrial minerals in rocks of Ladoga region. Works of VESEMPG. Publication editor A. A. Kadrik /M.: GEOKHI RAS, 2015; 343 p. ISBN 978-5-905049-11-8

Yurkovets V. P. Moissanite in the rocks of Ladoga region as an indicator of Ladoga impact. Works of VESEMPG. Publication editor A. A. Kadrik /M.: GEOKHI RAS, 2016; 122 p. ISBN 978-5-905049-11-8

Zharkova E.V., Lukanin O.A., Tsekhonia T.I., Senin V.G. Intrinsic oxygen fugacity measurements of impact glasses from impact craters El'gygytgyn (Chukotka, Russia) and Zhamanshin (Kazakhstan) UDC 550.843 (543.559)

V.I.Vernadsky Institute of Geochemistry and Analytical Chemistry RAS, Moscow (zharkova@geokhi.ru; lukanin@geokhu.ru; tsekhonya@geokhi.ru)

Abstract. The results of electrochemical measurements of the intrinsic oxygen fugacity (fO_2) of impact glasses from two impact craters E'lgygytgyn (Chukotka) and Zhamanshin (Kazakhstan), which may contribute to a deeper understanding of the redox conditions for the formation of impact transformation products of the Earth's crust, are presented. For the study, we took four samples of impact glasses from bombs of various sizes in the E'lgygytgyn crater, as well as two samples of irgizite and one sample of zhamanshinite from the Zhamanshin crater. The fO_2 measurements were carried out on a high-temperature furnace based on two solid electrolytes in the temperature range 800 – 1100°C and normal pressure. The fO_2 values of impactites from the El'gygytgen crater are located in the region between the wüstite-magnetite (WM) - iron-wüstite (IW) buffer equilibria and are significantly more reduced compared to typical magmatic melts of crustal and mantle origin. The oxygen fugacity of impact glasses from the Zhamanshin crater varies over a wide range. Irgizite glasses are the most oxidized. The fO_2 values of irghizites ≥ fO_2 (WM), and with an increase in temperature (≥1000-1050°C), they approach and even exceed fO_2 (QFM). The fO_2 of zhamanshinite glass in the entire studied temperature range is below fO_2 (WM) and corresponds to the values for impact glasses from the El'gygytgyn crater. It is shown that the intrinsic oxygen fugacity of the impact glasses of El'gygytgyn and Zhamanshin craters, as well as tektites in general, correlate well with the degree of iron oxidation - the less $Fe^{3+}/\Sigma Fe$ in the glasses, the lower the fO_2.

Keywords: *intrinsic oxygen fugacity, impaktites, tektites, El'gygytgyn and Zhamanshin impact crater.*

Introduction. High-speed impact events play an important role in the chemical transformation of planetary matter, especially in the early stages of the formation of the Earth and other planetary bodies. Impactite and tektite glasses formed as a result of the impact interaction of terrestrial rocks (target) and meteorites (impactor) under ultrahigh pressures and temperatures are products of quenching of high-temperature melts or liquid condensates of the vapor phase (Bazilevsky et al. 1983; Melosh, 1989; Heinen, 1998, etc.). One of the features of glasses of impact origin is their more reduced state in comparison with the target rocks. This is most evident in tektites - natural glasses ranging in size from a few mm to several cm, which are usually far removed from the parental impact crater, so that their genetic relationship is not always certain. Tektites have low $Fe^{3+}/\Sigma Fe$ ratios (0.02-0.12) much lower than the sources assumed for them - target rocks of various compositions (> 0.2-0.25) (Fudali, 1987; Lukanin and Kadik, 2007 and references therein). The low values of the intrinsic oxygen fugacity (fO_2) of tektite glasses, measured by the electrochemical method, also indicate their strong reduced state (Walter and Doan, 1969; Brett and Sato, 1984; Kadik et al., 2003). Impact glasses, in contrast to tektites, are located near or directly in the meteorite craters themselves. They form impact bombs ranging in size from a few centimeters to several meters, consisting almost entirely of glass. Tektite-like irgizites of the

Zhamanshin impact crater can also be referred to this type. Impact glasses have noticeably higher $Fe^{3+}/\Sigma Fe$ values (0.25 - 0.50) than tektites (Lukanin and Kadik, 2007; Volovetskiy, 2010, etc.). Comparison of them with the original rocks in some cases gives reason to believe that the formation of impactite melts, as well as tektites, is accompanied by reduction reactions of iron oxide (Bazilevsky et al. 1983; Feldman, 1990; Dressler and Reimold, 2001; and others). The reasons for the reduction of Fe^{3+} in the impact process remain the subject of discussion. The influence of the reduced impactor material (metallic iron, carbonaceous matter) on the redox state of tektites and impactites formed from a mixture of the target and impactor material is considered as one of the possible reasons. At the same time, it seems that the main reason for the reducing nature of impact glasses is redox reactions involving iron ions and other elements caused by changes in the T-P-fO2 regime during melting and evaporation of the target substance that has experienced a powerful impact (Yakovlev et al., 1992; Lukanin and Kadik, 2007).

This report presents the results of the electrochemical measurements of the redox state of impact glasses of two large impact craters El'gygytgyn and Zhamanshin. The data obtained contribute to a deeper understanding of the redox conditions during the formation of products of impact melting and evaporation.

Object and method of research. Impact crater El'gygytgyn (Chukotka) is the largest of the young craters on Earth (diameter ~ 18 km, age ~ 3.5 Ma). The target rocks are mainly represented by felsic volcanites: rhyolites and, to a lesser extent, andesites and dacites (Feldman, 1990; Koeberl et al., 2013). For the study, glasses were taken from three impact bombs of different sizes found near the crater: ~ 2 cm (sample E-1a), 30 cm (E-37b), 3x0.6 m (E-55b), as well as a fragment of (~ 6 cm) bombs of unknown size (sample E113-1). The Zhamanshin crater (Kazakhstan) has a diameter of ~ 7 km and an age of ~ 1 million years. It is formed in thickness of metamorphosed volcanic rocks, mainly basic and intermediate composition, which also includes shales and siliceous rocks. Near and in the crater itself, there are different types of impact glasses - tektite-like irgizites and zhamanshinites (Izokh, 1991; Jonašova et al., 2016, etc.). fO_2 measurements were carried out for two samples of irgizite glasses, which are fragments of tubular bodies 0.8–1.5 cm in diameter and up to 3 cm long (samples Irg-N and Irg-M). The third sample zhamanshinite (Zh-77b) is a fragment of an impact bomb from a crater ~ 20 cm in size.

Small pieces of glass (1-3 mm) carefully selected under binoculars to avoid the presence of external weathering crusts, bubbles, and visible crystalline and other inclusions in the glass were used for experimental determination of the intrinsic oxygen fugacity. The chemical composition of the measured samples is shown in Table 1.

Oxides	Zh -77 b	Irg-M	Irg-N	E-1a	E–37b	E–55b	E-113-1
SiO_2	77.88	54.37	78.43	66.8	69.71	72.22	71.37
TiO_2	0.53	0.80	0.71	0.48	0.36	0.28	0.32
Al_2O_3	11.47	20.67	9.20	17.16	16.14	15.53	15.48
FeO	4.26	7.54	4.24	3.86	2.75	2.18	2.41
MnO	0.1	0.15	0.04	0.01	0.05	0.01	0.08
MgO	0.69	2.84	2.07	1.32	0.97	0.27	0.86
CaO	0.53	8.22	1.83	3.61	2.78	1.71	2.25
Na_2O	1.14	3.75	0.70	2.97	2.67	2.58	2.89
K_2O	2.55	1.39	2.19	4.34	4.15	4.63	4.28
Cr_2O_3	0.03	0.00	0.02	0.09	0.03	0.00	0.00
NiO	0.00	0.00	0.02	0.01	0.03	0.00	0.00
CuO	0.03	0.00	0.05	0.00	0.12	0.00	0.08
Total	99.21	99.73	99.50	100.65	99.77	99.42	100.03

Table 1. Chemical composition of impact glasses from zhamanshin and El'gygytgyn craters

Table 2. Values of the coefficients "A" and "B" in the empirical dependence log $fO_2 = A - B/T^{\circ}K$ for the measured samples of impact glasses

Sample (size)	A	B	*n	**r
E-1a, impact bomb (~1-1.5 см)	14.153	35285	9	0.994
E-37b, impact bomb (≥30 см)	18.060	39720	8	0.984
E-55b, impact bomb ≅ 3 м	11.382	32510	8	0.985
E-113-1, impact bomb (unknown)	16.519	37653	7	0.980
Irg-M, irgizite	20.690	41630	8	0.991
Irg-N, irgizite	27.577	49718	8	0.994
Zh-77b, zhamanshinite	15,649	37391	7	0,992

n - number of experimental points;
** r-correlation coefficient.

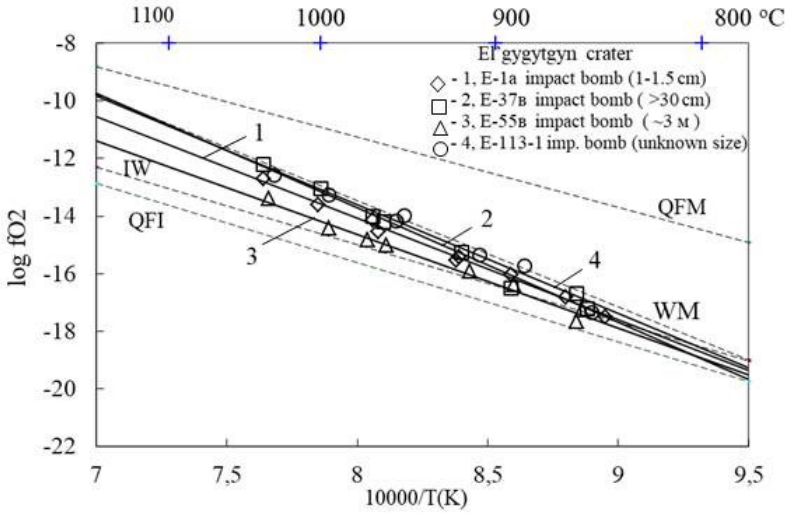

Fig. 1. Temperature dependence of the intrinsic oxygen fugacity of impact bomb glasses from the El'gygytgyn crater. Dashed lines are buffer equilibria: IW-iron-wustite, WM-wustite – magnetite, QFM-quartz-fayalite - magnetite, QFI-quartz-fayalite-iron.

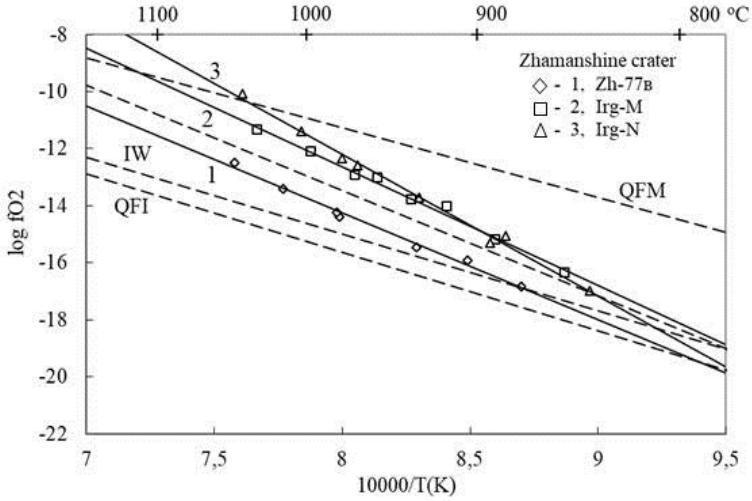

Fig. 2. Temperature dependence of the intrinsic oxygen fugacity of impact bomb glasses from the Zhamanshin crater. Dashed lines are buffer equilibria: IW-iron-wustite, WM-wustite – magnetite, QFM-quartz-fayalite - magnetite, QFI-quartz-fayalite-iron.

Measurements of the intrinsic oxygen fugacity of the samples were carried out on a high-temperature furnace based on two solid zirconium electrolytes at normal pressure in the temperature range from 800°C to 1050°C with a step of 30-50°C during heating and cooling of each sample. For more details on the technique, see (Kadik et al., 1989).

Results. For each sample, the results of measurements of intrinsic oxygen fugacity depending on temperature are described by a linear equation of the form (Fig. 1 and 2):

$\log fO_2 = A - B/T^{\circ}K$.

The measurement accuracy with a cyclic increase and decrease in temperature during the experiments is ±0.1-0.2 log. units. The values of the coefficients of equation A and B for all the studied samples are presented in table 2.

Electrochemical determinations of fO_2 of impact glasses from the Elgygytgyn crater are located in the region between the buffer equilibria wüstite-magnetite (WM) - iron-wüstite (IW). The temperature dependence lines for three samples (E-37b, E-1a, and E-113-1) are very close to the line of buffer equilibrium WM (Fig. 1). The line for the E-55b sample is slightly different. It has a lower slope, thus exhibiting lower fO_2 values at higher temperatures (> 950°C) to others. Correlation of line positions depending on the composition and size of impact bombs is not observed. It should be noted that at temperatures corresponding to the glass transition of acidic silicate melts (900-850°C), the fO_2 values for all samples approach each other. At temperatures above the melting point (≥ 950-1000°C), the fO_2 values of impact glasses are 2-3 orders of magnitude lower than the fO_2 values of the quartz-fayalite-magnetite (QFM) buffer, which are characteristic of acid magmatic melts. Comparison with the available determinations of the intrinsic fO_2 of different types of tektites shows that the impact glasses of El'gygytgyn correspond to some varieties of

indochinites, but are more oxidized relative to moldavites, for which the fO2 values are close to the IW buffer (Kadik et al., 2003). According to the Mössbauer spectroscopy data, the studied impact glasses of El'gygytgyn have higher $Fe^{3+}/\Sigma Fe$ ratios (0.16-0.20) than moldavites (0.06-0.08) (Rusakov et al. 2007, Volovetskiy, 2010).

Oxygen fugacity for two samples of irghizites with different silica content (Irg-M, Irg-N) in the studied temperature range is located in the region between the buffer equilibria WM and QFM (Fig. 2). This is in good agreement with the available electrochemical determinations of fO_2 for acidic irghizite glass (Kadik et al., 2003). The lines of the temperature dependence of fO_2 for irghizites (especially for Irg-N) have a noticeably steeper slope than the corresponding lines for Zh-77b and impactite glasses from the El'gygytgyn crater (Fig. 2). At elevated temperatures (≥1000 ° C) fO_2 of irghizites reaches the values of the QFM buffer. The zhamanshinite glass (Zh-77b) has a significantly more reduced character, all experimental points for this sample fall into the region between the WM and IW buffers, as well as for the impact glasses of El'gygytgyn (Fig. 1). These data are confirmed by Mössbauer determinations of the $Fe^{3+}/\Sigma Fe$ ratio in glasses of irghizites and zhamanshinites (Rusakov et al. 2007, Volovetsky, 2010): an anomalously low value of $Fe^{3+}/\Sigma Fe = 0.10$ was found in glass Zh-77b compared to glasses of irghizites (0.28- 0.35), as well as other zhamanshinite samples (0.24-0.41).

Conclusions.

1. The oxygen fugacity of the glasses of impact bombs from the El'gygytgyn crater, measured by the electrochemical method at 850-1050°C, is 2-3 orders of magnitude lower than the fO_2 (QFM) values. Thus, the impact melts formed as a result of the impact event are significantly more reduced than typical magmatic melts of crustal and mantle origin. The degree of reducing of the impact glasses of El'gygytgyn is comparable to some types of indochinites, but somewhat less than that of moldavites, genetically related to the formation of the Rhys crater (Germany), which has a larger diameter of ~ 25 km.

2. The oxygen fugacity of the impact glasses of the Zhamanshin crater, as shown by measurements, varies within wide limits. Irgizite glasses of acidic and intermediate composition are the most oxidized. The fO_2 values of irghizites ≥ fO_2 (WM), and with an increase in temperature (≥1000-1050°C), they approach and even exceed fO_2 (QFM). At the same time, for the zhamanshinite glass in the entire temperature range studied, fO_2 is almost an order of magnitude lower than fO_2 (WM) and is close to the values for impact glasses from the El'gygytgyn crater.

3. The measured oxygen fugacities of impact glasses from El'gygytgyn and Zhamanshin craters, as well as tektites as a whole, correlate well with the oxidation state of iron - the lower the $Fe^{3+}/\Sigma Fe$ glasses, the lower the fO_2.

4. The redox state of impact melts (glasses) formed as a result of impact events is determined by many factors. It is assumed that the main reducing factor is the temperature of the impacted substance. The maximum attainable temperature depends on the power of the impact event, which manifests itself in the size of the crater. In addition, the initial composition and redox state of the target rocks and impactors (meteorites) are obviously important. From this point of view, the diversity of the target rocks of the Zhamanshin crater, the presence among them of variously oxidized metamorphosed igneous and sedimentary rocks explains the formation of impact glasses with such a different degree of reduction. The target rocks of the El'gygytgyn crater are similar in composition and redox state. As a result, the impactites genetically associated with this crater are more homogeneous and, in general, are more reduced.

The work was carried out according to the state task of GEOKHI RAS (0137-2019-0017) and partial supported by RFBR (grant No 17-05-00713).

References

Bazilevsky A. T., Ivanov B. A., Florensky K. P. et al. Impact craters on the Moon and planets. Moscow: Nauka, 1983. 226 p. (in Russian)

Volovetskiy M. V. Valence and structural state of iron atoms in glasses of impact and volcanic origin. PhD thesis (Chemical Sci.), – Moscow. GEOKHI. 2010. – 128 P. (in Russian)

Kadik A. A., Lukanin O. A., Zharkova E. V., Feldman V. I. Oxygen and hydrogen (water) regime during tektite formation // Geochem. Int. – 2003. Vol. 41, № 9. – P. 865-880

Lukanin O. A., Kadik A. A. Decompression mechanism of ferric iron reduction in tektite melts during their formation in the impact process // Geochem. Inter. – 2007. Vol. 45. №. 9. – P. 857-881.

Izoh E. P. Zhamanshin impact crater and the problem of tektites // Geology and Geophysics – 1991. №. 4. – P. 3-15. (in Russian)

Rusakov V. S., Volovetskiy M. V., Lukanin O. A. Mössbauer studies of glass of impact and volcanic origin // Moscow University Physics Bulletin. – 2007. Vol.62. № 3. – P. 187-192.

Feldman V. I. Petrology of impactites. – MSU Publishing House. – Moscow, 1990, – 299 P. (in Russian)

Yakovlev O. I., Dikov Yu. P., Gerasimov M. V. Problems of oxidation and reduction in the shock process //Geochimiya, – 1992. – № 12. – P. 1359-1370. (in Russian)

Brett R., Sato M. Intrinsic oxygen fugacity measurements on seven chondrites, a pallasite, and a tektite and redox state of meteorite parent bodies // Geochim. Cosmochim. Acta, – 1984. Vol. 48. – P. 111-120.

Dressler B.D., Reimold W.U. Terrestrial impact rocks and glasses // Earth–Science Reviews. – 2001. Vol. 56. № 1-4. – P. 205-284.

Fudali R.F., Dyar M.D., Griscom D.L., Schreiber H.D. The oxidation state of iron in tektite glass // Geochim. Cosmochim. Acta. – 1987. Vol. 51. – P. 2749-2756.

Heinen G. Tektites witnesses of cosmic catostrophes. – Imprmerie, Luxembourg. – 1998. – 189 P.

Jonašova S., Ackerman L., Žak K, Skala R., Durisova J., Deutsch A., Magna T. Geochemistry of impact glasses and target rocks from the Zhamanshin impact structure, Kazakhstan: Implications for mixing of target and impactor matter // Geochim. Cosmochim. Acta, – 2016. Vol. 190. – P. 239-264.

Kadik A.A., Zharkova Ye.V., Kovalenko V.I., Ionov D.A., Uppermantle redox conditions: oxygen fugacity measurement on peridotite xenoliths from the Shavaryn Tsaram volcano, Mongolia // Geochem. Int. – 1989. Vol. 26. № 1. – P. 12-19.

Koeberl C., Pittarello L., Reimold W. U., Raschke U., Brigham-Grette J., Melles M., Minyuk P. El'gygytgyn impact crater, Chukotka, Arctic Russia: Impact cratering aspects of the 2009 ICDP drilling project //Meteoritics & Planetary Science. – 2013. Vol. 48. № 7, – P. 1108-1129.

Melosh H.J. Impact cratering – A geologic process. Oxford Monographs on Geology and Geophysics. 1989.№ 11. Oxford University Press. N.Y., Claredon Press. Oxford. – 245 P.

Walter L.S., Doan A.S. Determination of the P_{O2}–T equilibrium of indishinite tektite (abst.) NASA Astrophysics Data System (ADS) // Meteoritical Society. – 1969. Vol.4. P. 295-296.